UNIVERSITY OF SOUTHAMPTON

QUANTIFYING THE EFFECTS OF AIRFLOW DISTORTION ON ANEMOMETER WIND SPEED MEASUREMENTS FROM MERCHANT SHIPS

Bengamin I. Moat

Thesis submitted for the degree of Doctor of Philosophy

SCHOOL OF ENGINEERING SCIENCES
FACULTY OF ENGINEERING AND APPLIED SCIENCE

April 2003

UNIVERSITY OF SOUTHAMPTON

ABSTRACT

FACULTY OF ENGINEERING AND APPLIED SCIENCE
SCHOOL OF ENGINEERING SCIENCES

Doctor of Philosophy

QUANTIFYING THE EFFECTS OF AIRFLOW DISTORTION ON ANEMOMETER WIND SPEED MEASUREMENTS FROM MERCHANT SHIPS

by Bengamin Ivan Moat

Anemometers on Voluntary Observing Ships (VOS) are usually located above the bridge in a region where the effects of air flow distortion, created by the presence of the ship, may be large. Until now it was not known whether measurements from such anemometers would be biased high or low, and the possible magnitude of any such bias was not known.

Investigations into the airflow above merchant ships have been carried out experimentally using a low-speed wind tunnel and numerically using a commercial Computational Fluid Dynamics (CFD) code VECTIS. The investigations examined the airflow over simple block models of VOS shapes. The results of the investigations were compared to wind speed measurements made from the *RRS Charles Darwin*.

Experimental and CFD techniques have been used to devise scaling rules that predict the effects of the flow distortion. Both techniques have shown that the pattern of the flow distortion above the bridge scales with the 'step height', H, of the model. In the case of a tanker, H is the 'bridge to deck' height, i.e. the height of the accommodation block above the deck, for bow-on flows. Close to the top of the bridge the flow is severely decelerated and may even reverse in direction. Using the upwind edge of the bridge as the origin of the scaled co-ordinate system, there is a definite line above the decelerated region along which the speed of the flow is equal to the undistorted wind speed. Above this 'line of equality' the wind speed increases to a maximum and then decreases with increased height to a free stream wind speed. Simple equations have been devised to predict the positions of the 'line of equality', the maximum wind speed and the minimum wind speed within the decelerated region.

Comparisons of the results with wind speed data obtained from field measurements made using a number of anemometers located on the *RRS Charles Darwin* agreed well and have predicted a maximum wind speed increase of approximately 15 ±5 %. Comparisons with the field data have confirmed that CFD models can be used to predict the effects of airflow distortion above merchant ships.

The investigation has demonstrated the ability of the wind tunnel and CFD approaches employed to provide a better understanding of the airflow over merchant ships. Both methods have contributed to improve the understanding of how the wind speed at anemometer sites on merchant ships is affected by the ships hull and superstructure.

TABLE OF CONTENTS

LIST OF FIGURES

LIST OF TABLES

ACKNOWLEDGEMENTS

I would like to acknowledge the support and assistance of following people:

Mr. Robin Pascal (Ocean Engineering Division, SOC), for without him no *in situ* wind speed measurements would have been made from the *RRS Charles Darwin*.

Dr. Sheldon Bacon, Dr. Simon Josey, Dr. Elizabeth Kent, Dr. Robert Marsh, Dr. Lisa Redbourn, and Dr. Babalu Sinha for their helpful discussion.

Mr. Val Swail (Meteorological Service of Canada), for partial funding throughout this project.

Dr. P. K. Taylor (Head of Meteorology team, SOC) for his patience and advice.

Prof. Tony Molland (Department of Ship Science), who supervised this project, for his helpful comments and encouragement.

Most of all I would like to thank Dr. Margaret Yelland (Meteorology team, SOC), who jointly supervised this project, for her time, support, friendship and enthusiasm.

This work is dedicated to my late sister, Jan Perry Moat.

NOMENCLATURE

B_{aft}	distance from the stern to the aft edge of the bridge [m]
BH	bridge to waterline height [m]
C_{bow}	distance from the ship's bow to the containers [m]
C_{D10N}	drag coefficient at 10m and neutral stability
C_E	the stability and height dependent transfer coefficients for the latent heat flux Q_E
C_H	the stability and height dependent transfer coefficients for the sensible heat flux Q_H
C_v	specific heat capacity of a gas at a constant volume
C_μ	Dimensionless constant (see table A.1)
$C_{1\varepsilon}$	Dimensionless constant (see table A.1)
$C_{2\varepsilon}$	Dimensionless constant (see table A.1)
F	freeboard [m]
H	bridge to deck height [m]
H_{fore}	bridge to deck height for fore loading container ship [m]
$H_{fore+aft}$	bridge to deck height for fore and fore-and-aft loading container ship [m]
i	specific internal energy [Jkg^{-1}]
k	turbulent kinetic energy [m^2s^{-2}]
k_v	von Kármán constant [$k_v = 0.4$]
l	length scale (taken as the ship's length) [m]
L	bridge length [m]
LOA	ship's length overall [m]
MFR	Mass flow rate [kgs^{-1}]
p	pressure [Pa]
P	the rate of turbulent production of k
$\underline{q}$	velocity vector $\{u, v, w\}$
Q_H	sensible heat flux over the ocean [Wm^{-2}]
Q_E	latent heat flux over the ocean [Wm^{-2}]

r^2	correlation coefficient
R	universal gas constant
R_e	Reynolds number of the flow [$R_e = lU/\nu$]
$\overline{S_{ij}}$	mean rate of strain tensor
T	temperature [K]
u_*	friction velocity [m]
U	wind speed [ms^{-1}]
U_t	nominal speed in the wind tunnel [ms^{-1}]
U_{10N}	wind speed at 10m and neutral stability [ms^{-1}]
v_x	horizontal wind speed component [ms^{-1}]
x	distance aft from the front edge of the bridge [m]
x/H	normalised distance aft from the front edge of the bridge
y^+	dimensionless wall distance
z	height above the bridge [m]
z_0	roughness length [m]
z/H	normalised height above the bridge
δ_{ij}	Kronecker delta function
ε	rate of the dissipation of turbulent kinetic energy [m^2s^{-3}]
μ	coefficient of viscosity [$kgm^{-1}s^{-1}$]
μ_t	eddy viscosity [$kgm^{-1}s^{-1}$]
$\nu = \mu/\rho$	kinematic viscosity [m^2s^{-1}]
$\nu_t = \mu_t/\rho$	kinematic eddy viscosity [m^2s^{-1}]
θ	the angle of flow to the vertical [degrees]
ϕ	relative wind direction from the ships bow (bow =0°)
ρ	density [kgm^{-3}]
σ_k	dimensionless constant (see table A.1)
σ_ε	dimensionless constant (see table A.1)
τ	wind stress [Nm^{-2}]
τ_w	wall shear stress [Nm^{-2}]
Δy_p	distance of the near wall cell to the surface [m]
$\frac{1}{2}\rho U^2$	dynamic pressure

ACRONYMS

AT	acid tanker
BULK	bulk carrier
ChT	Chemical Tanker
COT	Crude Oil Tanker
COADS	Comprehensive Ocean Atmosphere Data Set
CO/PT	Crude Oil/products Tanker
IMO	International Maritime Organisation
LDA	Laser Doppler Anemometer
LOA	ship's length overall [m]
MFR	Mass flow rate [kgs^{-1}]
MT	Multi role Tanker
PIV	Particle Image Velocimetry
POT	Palm Oil Tanker
PT	Products Tanker
RRS	Royal Research Ship
R/V	Research Vessel
RNG	Renormalised Group theory
VLCC	Very Large Crude Carrier
VOS	Voluntary Observing Ship
VOSClim	Voluntary Observing Ship Climate Project
VSOP-NA	The Voluntary Observing Ships' Special Observing Project – North Atlantic
WMO	World Meteorological Organisation
YAG	Yttrium-Aluminum-Garnet crystals

1. INTRODUCTION

1.1 Background

Research ships are traditionally used to gather oceanographic data throughout the world. At the same time, merchant ships continuously travel across the world's oceans transporting cargo between continents. They cover more of the oceans than a single research ship can in its lifetime. As a consequence, a large proportion of the merchant fleet is recruited by the World Meteorological Organisation (WMO) Voluntary Observing Ship (VOS) programme to routinely report meteorological parameters at the ocean surface. Over many years these meteorological observations have been collected together to form a large database known as the Comprehensive Ocean Atmosphere Data Set (COADS; [1, 2]). COADS is used for weather forecasting, ocean/atmosphere model forcing, coupled ocean atmosphere model validation, satellite validation and to create climatologies to observe and predict possible changes in climate.

VOS meteorological observations include many parameters, e.g. cloud type and cover, precipitation, air temperature, sea surface temperature (SST), wind speed and direction and sea state. The observations are performed either visually (e.g. sea state, precipitation, wind speed and direction etc.), or by ship mounted instrumentation (e.g. air temperature from thermometers, wind speed and direction from anemometers and pressure from barometers). It is known that some of these parameters can be affected by the presence of the ship and a lot of effort has gone into correcting biases in VOS observations [3, 4, 5, 6]. For example, air temperatures measured by badly exposed instruments can be affected by heat from the ship so the data are biased high; SST data depend upon the measuring method used; air pressure has to be corrected to the sea surface height.

Similarly, it has long been suspected that wind speed measurements from anemometers may also be affected by the presence of the ship distorting the flow

of air [7], resulting in measured wind speeds which are accelerated or decelerated compared to the free stream, or undisturbed, flow. As an example, the numerical simulation of the air flow around a merchant ship shape are shown in Figure 1.1. The contours indicate the ratio of the wind speed to the free stream or undisturbed speed, i.e. a value of 1.0 indicates no change in the wind speed. Figure 1.1 shows possible accelerations of up to 10 % in the wind speed and decelerations well in excess of 10 %, depending upon the location of the anemometer. Anemometer wind speed measurements are made using either hand held anemometers on the bridge wing, or fixed anemometers which are located on a mast in the bows of the ship or more generally on a mast on top of the bridge. Until now, the sign and magnitude of possible biases in these measurements have not been quantified.

The impact that any bias in the wind speed estimate could have is illustrated here. The wind stress, τ, is the transfer of horizontal momentum between the atmosphere and the ocean surface. This is calculated from VOS observations of the mean wind speed submitted to COADS by the following 'bulk formula' method. Firstly, the wind stress is defined as:

$$\tau = \rho C_{D10N} U_{10N}^2 \qquad (1.1)$$

where ρ is the air density, C_{D10N} is the drag coefficient and U_{10N} is the wind speed. It is usual to correct wind speed measurements to a height of 10m and equivalent neutral atmospheric stability (standardised conditions). The subscripts 10 and N refer to a height above the sea surface of 10 m, and equivalent neutral stability values. C_{DN} is related to U_{10N}, and hence the wind stress, by an empirical bulk formula, e.g. [8]:

$$1000 C_{D10N} = 0.61 + 0.063 U_{10N} \qquad (1.2)$$

Any error in the wind speed measurements will lead to an inaccurate estimate of the drag and a large bias in the wind stress. For instance, a 10 % increase in wind speed applied to a U_{10N} of 10 ms^{-1} leads to a 27 % overestimate of the wind stress when calculated via equations 1.1 and 1.2.

The exchanges of heat between the atmosphere and the ocean are also dependent on the wind speed, but are not as affected by airflow distortion as the wind stress. The sensible heat flux, Q_H, corresponds to a loss or gain of energy by the ocean depending on the sign of the temperature difference between the ocean surface and the air. The latent heat-flux, Q_E, is the heat exchanged between the sea and the atmosphere by evaporation. Both parameters can be calculated from the VOS measurements using bulk formulae. In both cases the heat flux is directly proportional to the wind speed (assuming C_E and C_H constant) and any change due to airflow distortion will be transferred to the bulk calculation of the flux, i.e. a 10 % wind speed error will produce a 10 % error in the heat-flux. Errors of up to 10 % in wind speed have been estimated for well exposed anemometers on masts in the bows of research ships [9] and it is likely that errors of this magnitude, or greater, may be present in anemometer measurements on merchant ships since these often lack a well exposed mast in the bow. In addition, the relatively large size of a merchant ship means that anemometers will probably be positioned relatively closer to the superstructure than is usual on research ships.

1.2 Literature review

1.2.1 Wind speed measurements from ships

Previous work to determine the error due to the airflow distortion caused by air flow around ship's structures has mainly been concerned with oceanographic research ships. One qualitative approach compared wind speed measurements from anemometers located on a number of ships masts, and booms projected from the ships bow [10, 11, 12]. When ships are beam on to the wind, Ching [10] found that the mast wind speed measurements were biased high when compared to wind speed measurements made from anemometers on the bow booms. The least difference between measurements occurred when the wind was directly over the bow. Kidwell and Seguin [11] showed similar results and stated that the differences in wind speed between mast and boom sensors depended upon: the

relative wind direction, the wind speed, the sensor height above sea level and the exposure of the sensor to the wind.

A number of wind tunnel studies have been performed on ships to determine the wind speed error at anemometer sites. Mollo-Christensen [12] used a wind tunnel study of the R/V *Flip* to demonstrate that bow mounted anemometers have to be located at a distance greater than the windward cross section of the vessel to achieve a wind speed measurement accurate to within ±5 %. Romanov [13] for the Russian R/V *Akademik Mstislav Keldysh,* Surry [14] and Thiebaux [15] for Canadian research ships and Blanc [16, 17] for two naval ships carried out wind tunnel tests. Underestimates of the wind speed of 5 % at the end of a bow boom and 3 % for the foremast anemometer site were observed for the R/V *Akademik Mstislav Keldysh* for airflow over the bows, whilst the Canadian research ships exhibited overestimates of the wind speed of 5 % to 10 % for the main mast anemometer sites for most relative wind directions. Wind tunnel studies have also been used to examine the forces [18], wind resistance [19] of the above water hulls and below water hulls [20], but are of little use in this study as no wind speed measurements were made.

Previous numerical studies of the flow over ships have mainly concentrated on research ships (Kahma and Leppäranta [21]; Dupuis [22]; Moat and Yelland [23 to 28]; Yelland *et al.* [9, 29]; The numerical models varied in complexity. Kahma and Leppäranta [21] solved the flow field around a 2-dimensional ship profile of the *RV Aranda* using simple potential flow theory. Potential flow models simulate the flow of an ideal fluid and are of limited use as they do not reproduce many features of a real flow, e.g. flow separation. Nevertheless, their study gave the first insight into the magnitude of the flow distortion at anemometer sites on ships. Dupius [22] used a 2-dimensional CFD model to predict a wind speed increase of about 20 % at the main mast anemometer site on R/V *Le Suroit*. Moat and Yelland [23 to 28], and Yelland *et al.* [9, 29] used 3-dimensional Computational Fluid Dynamics (CFD) models to predict the airflow distortion at anemometer sites on a number of research ships. In all cases the ship

geometries were very detailed, and the anemometers were very well exposed and had low flow distortion (within 10 %).

Tai and Carico [30] compared a wind tunnel study and a CFD simulation to reproduce the flow conditions around the deck of a frigate for landing helicopters. Tai [31] presents similar applications for the flight deck of an aircraft carrier. Wind tunnel measurements of the surface pressures on the deck of a simple frigate shape were performed by Cheney and Zan [32]. The aim was to understand better the modelling of the effect of airflow distortion in helicopter-ship operations and produce a set of measurements by which to validate numerical results. Moctar and Bertram [33] used CFD to simulate the flow of air over a surface effect ship at a number of relative wind directions and studied the smoke plume from a passenger liner's funnel. A combination of CFD simulations and wind tunnel testing of the wind loads on a ferry was undertaken by Aage [34] to determine the ship manoeuvrability in a harbour.

Jin *et al.* [35] used a CFD model of the flow over a merchant ship to observe the influences of the funnel and accommodation arrangement on the smoke behaviour. Using a number of different funnel and deckhouse configurations they concluded that for safe smoke exhaust emission the ratio of the funnel height to the deck house height is 1.3 or larger.

1.2.2 The distortion of the airflow by masts and marine platforms

Many authors [36 to 45] have studied the effects of tower and mast structures on wind speed measurements. Their work either compares *in situ* anemometer wind speed measurements to a reference free stream wind speed, or makes use of wind tunnel studies. In summary, the air flow was found to be decelerated by up to 40 % in the wake region downwind of the structure, accelerated by up to 20 % either side and decelerated by up to 6 % in front. To achieve wind speed measurements accurate to within ±5 % Gill [37] recommends that anemometers should not be placed within the down wind wake regions and be located not less than 2 mast diameters from an open lattice mast and not less than

3 mast diameters for a solid cylindrical mast. In a comparison with measured data Wucknitz [44], and Kondo and Natio [45] show that the flow around cylindrical masts can be represented well by a simple numerical models of the flow of an ideal fluid around a cylinder. This early work shows the importance of placing anemometers in well exposed locations.

Thornthwaite *et al.* [46] measured the wind speed at different locations above and below a box-like platform standing on 4 legs, 20 m above the sea surface. The wind speed measurements above the platform were normalised by a wind speed measured from a reference anemometer. Using an indirect approach the study estimated the boundary layer profile during the period of study and corrected the changes in the wind field caused by the platform. For an airflow normal to the side of the platform two jets of accelerated air, one above and one below the platform, extended from the upwind leading edge of the box. The maximum accelerated wind speed within both jets was 18 %. In front of the platform and close to the roof and underside of the platform the wind speed was decelerated by up to 30 %.

For flows over box-like offshore platforms, Davies and Miller [47] performed flow visualisation studies that showed that the flow separated at the upwind leading edge of the platform, and that within the region of separation there existed an unsteady recirculating motion. The study showed that the extent and shape of the flow separation regions are related to the dimensions of the block (i.e. the block thickness) and the flow direction.

A wind tunnel study by Chen *et al.* [48] measured the wind speed above the helideck (28.6 m above the sea surface) of a box-like offshore platform. The wind speed measurements were standardised by a reference wind speed measured at height of 12 m above the helideck. Airflows normal and for relative wind directons of 14° and 30° to the helideck were measured. In all three cases the flow separated at the upwind leading edge of the helideck and wind speed accelerations of up to 40 % in wind speed where observed.

In summary, previous work to quantify the air flow distortion around ships have shown wind speed increases in the order of 10 % to 20 % are possible. Anemometers located close to masts and spars (< 2 mast diameters) may experience possible increases of 20 %, or large decelerations of approximately 40 % may be experienced if the instrument is located in the downstream wake of the mast. Marine offshore platforms are complex structures and wind speed increases of approximately 40 % may occur.

1.3 Objectives of the study

The principal objectives of the work have been to:

1) Gain an improved understanding of the airflow distortion above the bridge of merchant ships;

2) Use experimental and theoretical techniques to quantify the airflow distortion for anemometers in terms of position relative to the bridge;

3) Propose methods to determine the suitable correction to wind speed measurements based on merchant ship type and anemometer position.

The work has been carried out using both experimental and CFD studies of the flow over two typical merchant ship types. The CFD approach was carried out using a commercial code (VECTIS) and the experimental work was conducted using a wind tunnel.

It is impossible to perform a wind tunnel, or numerical, study of the airflow over every individual VOS ship since their numbers are too great. Chapter 2 details a generic approach to create typical merchant ships from their overall length. These generic ship models are very simple block-like, or bluff body, shapes that were derived from ship dimensions listed in the publication *Significant Ships* [49].

A summary of the stages of the work programme is as follows.

i) Wind tunnel testing of two generic bluff body merchant ship shapes.

ii) Validation of the CFD code by comparison with published data (two simple bluff body cubes).

iii) CFD investigations of the airflow above the bridge of a full sized tanker of length 170 m and at the size used in the wind tunnel study (length 3.7m).

iv) Comparisons of the CFD studies with the wind tunnel data. The hypothesis that the flow field above the bridge scales with the bridge to deck height, or the 'step height', is tested.

v) Comparisons of wind tunnel and CFD studies with *in situ* wind speed measurements made above a ship.

vi) Discussion of results and proposals for practical applications of the outcomes of the work.

The flows above the bridge of two simple generic ships were studied in a wind tunnel for a flow directly over the bow of each ship (Chapter 3). A Particle Image Velocimetry (PIV) system was used to map the flow field above the bridge and the results were examined for a scaling law. The aim was to predict the flow above the bridge given only the ship type, step height (derived from the length overall) and anemometer position.

Wind tunnel experimentation is time consuming and although producing high quality data, the PIV system is limited in the amount of measurements that it can produce. For this reason, the use of Computational Fluid Dynamics (CFD) as an alternative method to simulate the air flow over ships was applied in Chapter 4. This chapter examines the performance of the CFD code VECTIS by comparing the results of various CFD models to the PIV measurements.

For this study the research ship *RRS Charles Darwin*[1] was instrumented with a number of anemometers above the bridge and wind speed measurements were made for a period of eight weeks in open ocean conditions. Only relative wind directions over either beam were considered as these reproduced the flow over a bluff body shape. Chapter 5 validates the scaling laws derived in Chapter 3 by comparison with the *in situ* wind speed measurements.

An overall discussion, bringing together the results of the experiments and CFD investigations is given in Chapter 6.

A summary of the outcomes and applications of the investigation and final conclusions are drawn in Chapter 7, together with recommendations for further work.

[1] Operated by: National Environment Research Council (NERC) Research Ship Unit, Southampton Oceanography Centre, Southampton, UK.

2. DETERMINING GENERIC MERCHANT SHIP SHAPES

2.1 Introduction

The VOS fleet contains about 7000 merchant ships of various types, sizes and shapes. Of these, about 10 % leave the VOS fleet and are replaced by other ships each year [50]. It is clearly not feasible to model the flow of air around each individual VOS ship. However, it is considered that the fleet may be split into different basic types of ship; such as a tanker, container ship, bulk carrier, general cargo ship and others (Figure 2.1), and that each type could be represented by a generic, or typical, ship shape. This chapter describes the generic shapes and the method by which they were determined.

The VOS metadata[2] (WMO47, [51]) does not contain information on the ship type, shape or size. Instead, ship dimensions were taken from the Royal Institution of Naval Architects yearly publication *Significant Ships* from 1990 to 1993 [49]. These were taken to be representative of ships currently in service. The *Significant Ships* publication includes both passenger and merchant ships above 100 m in length. A typical publication lists around 45 ships which are included because of their innovative cargo handling systems, above average safety features or automated navigation systems. It is therefore believed that these ships are not significantly different in dimension from the rest of the world merchant fleet or from the VOS fleet. *Significant Ships* does not list all the dimensions required, but provides A4 scale plans which were used to extract the dimensions necessary to create a simple ship geometry. From comparison of the ship plans, it was clear that bulk carriers were similar in shape to tankers and for this reason these two ship types were grouped together. A total of 71 ships were used to represent three of the five major ship types; 1) tankers and bulk carriers and 2) container ships. General cargo ships can show wide variations in their overall shape so this type of ship was not considered for a generic type. The fifth ship class ‘other’ contains passenger liners, research vessels and car transporters

[2] A set of data that describes and gives information about other data.

etc., but because of their varied shapes a generic model of this class of ship can not be developed.

A potential subset of 200 VOS are currently being recruited and meteorological data from these ships will be used in the Voluntary Observing Ship Climate (VOSClim) project (Kent and Taylor, [52]). Unlike the VOS, the VOSClim data will include the ships overall length (LOA), ship type and anemometer position. The aim of this chapter is to generate a generic ship shape using just the LOA and the ship type.

Figure 2.1 shows the distribution by ship type of the VOSClim fleet [52], the world fleet (ISL, [53]) and the ships registered by Lloyds of London in 1999 [50]. The distributions differ since the VOSClim ships are all open ocean vessels, whereas the world fleet and Lloyds includes many small coastal vessels. Together the tanker/bulk carrier shapes (hereafter referred to as tanker shapes) and the container ships represent 53 % of the VOSClim fleet, 39 % of the world fleet and 40 % of the 1999 registered Lloyds fleet.

The generic ship shapes developed in Section 2.2 are very simple block models (Figure 2.2) and clearly differ in many ways from a real ship structure. For example: the bow is a broad flat shape rather than a curved surface; the deckhouse spans the whole breadth of the ship; and masts, satellite communication domes and other small-scale obstructions are not included in the model. For these reasons the simulations (performed in subsequent chapters) of the flow distortion above the deckhouse will represent that caused by the large-scale obstruction of the ships hull and superstructure only. For instruments located above the deckhouse it is the absence of any small-scale obstruction which is thought to be the most significant difference between the generic and the real ship shape. In particular, an instrument mounted on a mast above the deckhouse would, in reality, be affected by the flow distortion caused by the mast. The extent of this distortion will depend on the mast shape, and distance between the mast and the instrument [37]. However, such information is not presently available, even in the VOSClim metadata. In summary, it should be noted that, at present, neither the sign nor the magnitude of the effects of flow distortion are

known for instruments mounted on VOS, and the simple generic ship shape approach allows at least a first-order estimate of these effects to be obtained. These estimates may be refined in future, as and when suitable detailed information about instrument locations is available in the metadata.

2.2 Generic ship models

2.2.1 Tanker model

The principal dimensions of 36 tankers and 8 bulk carriers (Table 2.1) were taken from *Significant Ships* and used to create the generic tanker geometry. The bridge to waterline height (BH), bridge length (L), breadth (B) and the freeboard (F) were used to describe the generic ship geometry (Figure 2.2). The bridge to deck height, H, was calculated from the difference between the bridge to waterline height and the freeboard, i.e. BH-F. Since the ships LOA is a known dimension in the VOSClim dataset, linear regressions were fitted to each ship dimension against LOA in Figures 2.3 to 2.7. The coefficients for each regression are listed in Table 2.2. The equation for the bridge to deck height is stated as it is used in later chapters:

$$H = 9.11 + 0.026 \times LOA \qquad (2.1)$$

These relations are able to realistically predict each ship dimension from the LOA and hence a simple representation of a tanker can be determined using only its length.

The assumption that a bulk carrier is similar to a tanker is tested by overlaying the respective dimension of both ship types against the ships length overall (LOA) in Figures 2.3 to 2.7. The limited number of bulk carriers makes direct comparisons with tankers difficult, but it can be seen that their dimensions lie within the spread of the corresponding tanker dimensions. From Figure 2.4 it could be speculated that bulk carriers have a smaller freeboard than tankers, but this is regarded as insignificant since freeboard varies with the loading of the ship and could change with every passage the ship makes. The ships loading will be

reported to the VOClim project [52] and the variation in free board will be examined. It is apparent that the bridge to deck height is not constant (Figure 2.7), but varies between 11 m to 19 m with the ships length overall.

Figures 2.3 to 2.7 show that the merchant ships can be grouped by LOA into three distinct classes; ships below 200 m, ships between 200 m to 300 m and those over 300 m. Ships over 300 m correspond to Very Large Crude Carriers (VLCC) and large bulk carriers, whilst ships between 200 m to 300 m are generally crude oil tankers that have a restricted breadth to allow them passage through the Suez and Panama canals. Ships below 200 m are specialised chemical tankers, which transport specific goods. Three tankers of lengths 170 m, 250 m and 330 m which represent the three LOA classes have been created from the linear regressions fitted through the data in Figures 2.3 to 2.7. The dimensions of each ship are detailed in Table 2.3 and overlaid in Figures 2.3 to 2.7. If more data were used it may be more representative to fit three separate regressions for each of the LOA groupings.

2.2.3 Container ship model

The principal dimensions of 27 container ships (Table 2.4) were used to create the generic model derived in this study. Two types of container ship are present in *Significant ships*: firstly, ships with containers only loaded in front of the deck house, and secondly larger ships with containers loaded in front of and behind the deckhouse. There was an approximate 50/50 split between 1) forward-loading and 2) fore-and-aft loading designs in the ships studied. As there is no dominant ship type it was decided to create generic models of both ships. The block representations of the two generic ships, and the dimensions used are illustrated in Figure 2.8a and 2.8b. For simplicity, the freeboard is assumed to be equal to the height of the bow above the sea. This is not strictly true, as the bow is higher than deck level.

Each ship dimension is plotted against LOA in Figures 2.9 to 2.15. Overlaid are the generic container ship dimensions for forward loading container

ships of lengths 125 m and 180 m, and fore and aft loading container ships of lengths 180 m and 270 m. generic ship dimensions for these four types are dervied below and detailed in Table 2.6. Instead of fitting one linear regression through the data, it was apparent that the dimensions of the two types of ship differ slightly and two regressions were needed to represent the fore loading and the fore-and-aft loading ship types. The only exception is the bridge to container top height, H, (Figure 2.15) which could be represented by a single regression. This is shown by the two almost identical regressions fitted for each ship type. Table 2.5 contains the coefficients of the linear regressions derived from Figures 2.9 to 2.15 for both fore-loading, and fore-and-aft loading generic models. The equations for the bridge to container top height, H, are:

$$H_{fore} = -0.03 + 0.03 \times LOA \qquad (2.2)$$

$$H_{fore+aft} = 1.2 + 0.023 \times LOA \qquad (2.3)$$

The bridge to deck height, H, varies with LOA and is approximately 3 m for ships of 100 m in length, increasing to 8 m for ships over 250 m in length.

Figures 2.9 to 2.15 show that ships with LOA less than 160 m have only forward loaded containers whilst the largest container ships of LOA over 215 m have containers loaded in front and behind the bridge superstructure. An overlap of the two designs exists between a LOA of 160 m to 215 m.

2.3 Summary

The data from *Significant Ships* [49] has been used to developed a generic tanker/bulk carrier and a generic container ship by relating each dimension to the ships overall length. These generic models of the ships are used in subsequent chapters where the flow distortion above the bridge is examined and related to the bridge to deck height, H. Providing the anemometer location is known, this will create a method to correct for the effects of airflow distortion based only on knowledge of H (calculated from the ships LOA) and ship type. In future years, this correction will be applied to the VOClim data.

3. WIND TUNNEL STUDIES OF THE FLOW OVER THE GENERIC SHAPES

3.1 Introduction

The low speed section of the University of Southampton 2.13 m by 1.52 m (7' by 5') wind tunnel [54] was used to examine the flow over scaled models of the generic merchant ships. The scaled generic merchant ships placed in the wind tunnel were created using the relations developed in Chapter 2. In total, three wind tunnel studies were performed. The first used a thermal probe anemometer to determine the wind speed at different locations in the wind tunnel and above the bridge of the generic merchant ships. Two subsequent experiments used a state-of-the-art Particle Image Velocimetry (PIV) system to measure the velocity field above the bridge of the generic merchant ship models.

The experimental techniques used to measure the wind speed in the tunnel and the three experiments used to evaluate the flow over the generic ship models are described in Section 3.2. The accuracy of the wind speed data is examined by comparing wind speed profiles from all three wind tunnel experiments (Section 3.2). The PIV measured wind speeds are used to quantify the flow distortion above the bridge of a number of generic ship models (Section 3.3). Simple equations are derived to define the pattern of the flow and the magnitude of the wind speed above the bridge of the ship geometries. Wind tunnel time and resources allowed only measurements on the centreline of the bridge and flows directly over the bow. The wind tunnel was not wide enough to allow the flow above the scaled ship geometries to be measured at other relative wind directions. Therefore, wind speed measurements were made at relative wind directions of 15° and 30° above the bridge of the deck house block (Section 3.4) only. However, air flows directly over the bow are believed to be a realistic representation as 41 % of merchant ships' observations/data are obtained for relative wind directions within ±25° of the bow (Figure 3.1). This is due to the apparent wind angle moving towards the bow when the ship moves at speeds which are a significant fraction of, or greater than, the true wind speed.

3.2 The wind tunnel experiments

3.2.1 Introduction

The low speed section of the Southampton University wind tunnel is 5 m long with a 4.6 m by 3.7 m working cross section. The generic tanker geometry (Figure 3.2) was scaled by 1:46 in order to create the largest model possible (for high spatial resolution of the measurements) without causing undue blockage of the flow. Dimensions are shown for a full-scale ship and for the geometry used in the wind tunnel study (shown in brackets). For a flow directly over the bows of the model the blockage ratio (frontal area of ship : area of the wind tunnel section) was 1.5 %. This ratio is less than the typical values stated by Barlow *et al*. [55] and corresponds to that used by Castro and Robbins [56]. Therefore, no blockage correction was applied as a blockage ratio of 1.5 % should only cause a 1.5 % increase of the flow velocity on average. A generic containership geometry was made by adding an extra block (block 4, Figure 3.3) to the tanker geometry in order to represent the containers loaded forwards of the deck house. The container model therefore had a slightly smaller beam than it should have been (Chapter 2.2.3). Wind tunnel tests were also performed over just the deck house block (block 1, Figure 3.2) in order to increase the range of bridge to deck or, in this case bridge to sea, heights modelled.

Wind tunnel tests attempt to simulate the full-scale flow. If the Reynolds number (eq. 3.1) of the wind tunnel experiment is in the same Reynolds number regime as the full-scale flow, then the model and the full-scale flow will be dynamically similar [55], i.e. the ratio of the velocities at two points in the wind tunnel will be the same for a full-scale flow. In practice it is difficult to match the Reynolds number typical in full-scale flows. The Reynolds number is the ratio of the inertial forces to viscous forces in a given flow:

$$R_e = \frac{lU}{\nu} \qquad (3.1)$$

where; l represents the ship length, U is the wind speed, and $\nu = 1.44 \times 10^{-5}$ m^2/s

is the kinematic viscosity of air at 15 °C. The full-scale and wind tunnel scale Reynolds numbers are detailed in Table 3.1. The wind tunnel R_e value was higher than the critical value of 5×10^5 suggested by Romanov *et. al.* [57], which suggests that self similarity holds. Molland and Barbeau [58] measured the dependence of the aerodynamic drag of scaled bluff body catamarans on R_e in the Southampton University wind tunnels. For wind tunnel R_e between 1.07×10^6 to 2.68×10^6 there was negligible change in the drag coefficient of the body, confirming that the results were independent of R_e and that self similarity holds. Again, this suggests that self similarity holds between the wind tunnel experiments and the full-scale flow using these wind tunnels and Reynolds numbers.

The wind tunnel was run at a nominal constant dynamic pressure:

$$\frac{1}{2}\rho U_t^2 = \text{constant} \qquad (3.2)$$

where ρ is the density of air and U_t is the nominal wind speed. This is common wind tunnel practice to provide a constant non-dimensionalising factor. The fan speed was adjusted until the Betz manometer reading corresponded to a wind speed of 7 ms^{-1}. To maintain a constant dynamic pressure the fan speed had to be routinely varied to keep the wind tunnel pressure constant, i.e as wind tunnel temperature increased the density reduced and therefore the nominal wind speed had to be increased. To minimise these resultant changes in wind tunnel speed, the third wind tunnel experiment did not use a constant dynamic pressure, but instead used a set fan speed of 437 rpm. This corresponded to a nominal wind speed of 7 ms^{-1}. In all experiments, the model was oriented so that the flow was directly over the bow and all measurements were made along the centreline of the ship.

Wind tunnels that run at a constant dynamic pressure will have variations in the nominal wind tunnel speed with temperature. It is standard practice to normalise wind speed profiles by a reference wind speed simultaneously measured at one fixed location. Since the aim of this study is to quantify the absolute wind

speed errors it was thought necessary to obtain accurate free stream velocities at all locations of interest. Therefore, during the three wind tunnel experiments the geometries were periodically removed and the vertical profiles of the free stream velocity were obtained. These free stream profiles were used to normalise the wind speed measurements made with the model present in the same location in the wind tunnel and the absolute wind speed changes were determined.

3.2.2 The thermal probe anemometer study

The first wind tunnel experiment (Figure 3.4) took place between the 2nd and 4th May 2000 during which a thermal probe[3] anemometer (measurement accuracy of within ±2 %) was used to measure the wind speed above the bow and the bridge of both the tanker and container ship geometries. A number of vertical profiles of the free stream wind speed at various locations in the wind tunnel were measured and are shown in Figures 3.5 a) and 3.5 b).

Problems were highlighted by the analysis of the free stream wind speed profiles shown in Figure 3.5 a) and b). Firstly, the variation in time of the free stream profiles suggested that the mean wind speed at different positions in the tunnel were increased by up to 1 ms^{-1} from its nominal set value of 7 ms^{-1} and, due to temperature changes could drift by up to 0.5 ms^{-1} over a period of a few hours or less. These variations in wind speed caused problems when trying to normalise the vertical profiles obtained around the ship geometry. Secondly, the general shape of the wind speed profile showed that a wall jet was present close to the tunnel floor. The wind speed increased to a maximum at a height of approximately 0.1 m and then decreased with height. Thirdly, the thermal probe anemometer had a specified accuracy of 2 %, but only measured the horizontal component of the wind speed. This meant that the instrument could have significantly underestimated the wind speed in the regions of interest, i.e. above the bridge where the flow can be at a large angle from the horizontal. For these reasons, the results from this first experiment should be are treated with caution.

---

[3] Developed and calibrated by: Airflow developments Ltd., High Wycombe, U.K.

However, from the point of view of normalising the measured speeds, the experiment proved useful in that it highlighted the necessity of obtaining free stream wind speed data in the region of interest as soon as possible after the with-ship geometry measurements.

3.2.3 The PIV system

The first PIV measurements (PIV 2000) took place between the 22nd August and 23rd August 2000. In the time available, it was only possible to measure the velocity field above the tanker in any great detail. Therefore, a second PIV experiment was performed between the 17th September to 19th September 2001 (PIV 2001). The same PIV system was used for both experiments and the geometries were located the same distance from the wind tunnel inlet as in the thermal probe study.

Details of the PIV system are available from Dantec [59], and are summarised here. In contrast to other methods which employ probes to measure the velocity, the PIV is an optical technique and therefore nonintrusive. It is time consuming to set-up the PIV system in the wind tunnel, but once achieved the PIV allows the measurement of 2-dimensional velocity vector maps. The PIV method is based on projecting two consecutive light sheets (separated in time by between 30 μs to 100 μs) from a high power laser into a dark wind tunnel, which was seeded with smoke. A digital camera normal to the light sheet records the position of the seeded particles and statistical methods are used to determine their displacement. The velocity is calculated by dividing the displacement of the particles by the time delay between the light sheets.

The experimental set up is shown in Figure 3.6 and illustrated schematically in Figure 3.7. A high power Neodymium-YAG (Nd:YAG) laser was mounted at a height of 1.97 m on a beam running the length of the tunnel. The beam was attached to the tunnel roof by a square frame at the upstream end and by an A-frame bolted to the tunnel floor downstream. Due to difficulties in positioning the beam, the generic ship geometry was moved 0.24 m off the centreline of the

tunnel. The vertical laser sheet was orientated parallel to the mean flow, and a DANTEC 80C60 Hi-Sense digital camera was mounted in a metal frame 1.28 m from the measurement area. The height of the camera could be adjusted to measure different areas of the flow. A smoke generator using regular Disk Jockey smoke fluid was used to seed the airflow in the tunnel.

The flow field above the bridge of the tanker was recorded using various amounts of seeding in the tunnel and various time delays between laser sheets. The above findings were used to define the following parameters used during both PIV experiments. The camera was able to sample a measurement area of 152 mm by 191 mm. The measurement area was divided into an array of 64×64 smaller areas, referred to as interrogation areas. A cross correlation technique [59, 60] based on this interrogation area size was used to determine the particle displacement based on a time delay of 50 μs between laser sheets and produced 31 (z, vertical) by 39 (x, streamwise) velocity measurements, i.e. a resolution of about 4.9 mm in the measurement area.

One hundred velocity maps were taken at each of four measurement areas (Figure 3.7) above the bridge of each ship and used to create a time average of the flow. A time delay of 0.5 seconds between velocity maps provided a sampling period of approximately 50 seconds. The four areas were combined and a flow field of size 0.36 m (x, stream wise) by 0.29 m (z, vertical) was created, which corresponded to 73 (x, streamwise) by 59 (z, vertical) velocity measurements. As a check on the consistency of the PIV system, the camera was positioned so the four measurement areas overlapped by 0.03 m and 0.014 m in the streamwise and vertical directions respectively (Section 3.2.4). To overcome the problem caused by the wind tunnel speed varying from its nominal value of 7 ms^{-1}, each measurement area was also sampled without the ship geometry present, with this data subsequently used to normalise the results.

Spuriously large velocities (above ± 15 ms^{-1}) were removed from the vector maps. Careful examination of the data during the experiment showed that this accounted for less than 3 % of the velocity measurements. A time average of the

flow was calculated after each measurement. During post-processing of the time averaged wind speed data, only mean velocities with sample sizes of 80 or more and standard deviations of less than 2 ms^{-1} were selected. The limit of the standard deviation was set high in order to capture the unsteady flow within the recirculation region. In general, the flow outside the recirculation region was steady and the standard deviation was less than 0.2 ms^{-1}. In order to smooth out any scatter in the time averaged vertical profiles of the wind speed, a 3-point running mean was applied spatially to the vertical profiles of the normalised wind speed data. In general, the difference between the smoothed and unsmoothed wind speed profiles was less than 1 %. All normalised wind speed profiles presented in this chapter have been smoothed in this fashion.

3.2.4 Accuracy of the PIV results

The normalised wind speed profiles calculated using the wind tunnel measurements could be affected by variations in the nominal wind tunnel speed. The thermal probe study of the air flow in the wind tunnel has shown that the wind speed in the tunnel can drift by 0.5 ms^{-1} within an hour or less (Section 3.2.2), i.e. the free stream wind speed used to normalise the wind speed profiles could change during the time taken to measure the flow over each ship geometry. Therefore, the free stream wind speed was measured as soon as possible after the with ship geometry measurements. At each measurement area the times between the PIV measurements made with and without the ship geometry present were minimised and are: 40 minutes for the tanker, 30 minutes for the container ship and 10 minutes for the deck house block. Stopping the wind tunnel and changing the ship geometries caused the delay between each measurement. To determine any bias caused by variations in the free stream wind tunnel speed this section compares: i) the normalised wind speeds in the overlapping regions of the PIV measurement areas, ii) the normalised wind speed profile measured during the thermal probe experiment to the two separate PIV experiments, and iii) the free stream wind speed when the wind tunnel was run using a constant dynamic pressure (thermal probe and PIV 2000 experiment) and when using a constant fan speed (PIV 2001).

Firstly, during the experiments the PIV measurement areas were overlapped to determine any bias in the measurements. The vertical overlaps were made within 100 minutes of each other, whilst the horizontal overlaps were made within a day of each other. Even with the long time delay between measurements a comparison of the overlapping regions suggested that changes in the wind speed measurements were generally 4 % or less. Due to noise in the PIV 2000 measurements it was only possible to compare normalised wind speeds between the lower two overlapping regions of the tanker measurements. This comparison also suggested that biases in the wind speed measurements made during the PIV 2000 experiment were about 4 % or less.

Secondly, the accuracy of the PIV system in the wind tunnel was examined by comparing the wind speed measurements made during the three separate wind tunnel experiments. Wind speed profiles at a distance of x=0.074 m from the upwind leading edge of the bridge have been selected from; the thermal probe, the PIV 2000 and the PIV 2001 experiments and the normalised wind speed profiles are shown in Figure 3.9. During the PIV 2001 experiment the wind speed above the front edge of the tanker was deliberately measured twice to determine if any change in the wind speed measurements occurred during the experiment. Both are shown separately here. All PIV measured profiles were normalised by the wind speed profiles obtained in the same location with no model present, measured during each respective experiment. During the thermal probe study no free stream wind speed profile was measured at the bridge measurement location in the centre of the tunnel, therefore the thermal probe wind speed was normalised by a wind speed profile measured 0.83 m abeam of the bridge with no model present (position 2, Figure 3.5a). The normalised wind speed profile from the thermal probe is thought to be reliable, as the probe is a robust method used to measure wind speed.

The thermal probe anemometer measured only the longitudinal component of the wind speed. In order to calculate the total wind speed, a cosine correction was applied to the anemometer wind speed measurements;

$$\text{total wind speed} = \frac{v_x}{\cos(\theta)} \qquad (3.3)$$

where v_x is the horizontal wind speed component and θ is the angle of the flow to the vertical at the measurement location. The angle of the flow, θ, was obtained from the PIV 2000 data.

Figure 3.9 shows the normalised wind speed profiles from all three experiments. The vertical scale is the height above the bridge in meters and the vertical dashed line indicates normalised wind speeds of 1.0 where the measured wind speed equals the free stream speed. The error bars indicate the standard error. The profiles agree well in their general shape. The normalised wind speed increased with height to a maximum at a height of about 0.08 m above the bridge, and then decreased. Although the results agree well on the height of the maximum wind speed they differ in the magnitude of the maximum wind speed. The normalised thermal probe measurements of the wind speed maximum are approximately 1.20, the PIV 2000 measurements by 1.30 and the PIV 2001 measurements are 1.34. The magnitudes of the measured PIV 2001 wind speed maxima agree to within 2 % of each other. All the normalised wind speed measurements are independent of the wind tunnel temperature, as the measured winds speeds were all made within 1 °C of the respective free stream measurements, and should agree. This suggests that there may be some variability in the wind tunnel measurements. Therefore, a time series of the change in free stream wind speed from both PIV experiments was examined to determine if running the wind tunnel at a constant fan speed reduced the variation in the wind speed in the tunnel and provided a more consistent result.

The change in the free stream wind tunnel speed was examined with variable tunnel fan speed with constant dynamic pressure (PIV 2000), and constant tunnel fan speed with variable dynamic pressure (PIV 2001). The thermal probe anemometer was located in the wind tunnel (Figure 3.6) throughout the 2 days of the PIV 2000 experiment. The thermal probe anemometer measured the wind speed at a fixed location which corresponded to a distance of 0.80 m downstream of the upwind leading edge of the bridge, and at a height of

0.93 m above the wind tunnel floor. The temperature inside the wind tunnel was measured using a fixed probe and was recorded at the beginning of each PIV measurement. With the wind tunnel running using a constant dynamic pressure a time series of the mean wind speed data (Figure 3.10) shows, in the absence of the ship geometries, increases of up to 0.2 ms^{-1} within a period of 30 minutes. In Figure 3.10 the error bars indicate the standard error. More importantly a consistent reduction of 0.4 ms^{-1} in the free stream wind speed occurred between the two days. This cannot be explained by the changes in the daily atmospheric pressure (< 1 mbar), or wind tunnel temperature between the two days (20 to 30 °C). Oil deposits from the smoke that was used to seed the tunnel could have contaminated the thermal probe sensor and caused the discrepancy in the wind speed between the two days. The PIV 2000 measured free stream wind speed at the four measurement locations is shown in Figure 3.11. Each separate measurement area is indicated. The upwind leading edge of each model was located at x=z=0, 0.422 m above the tunnel floor. The direction of the flow is from left to right. Analysis of the data showed a low signal to noise ratio representing scatter in the normalised wind speed measurements.

During the PIV 2001 experiment the dynamic pressure in the wind tunnel was varied. The free stream wind speed was measured over a period of 3 hours during the morning of the second day of the experiment (19th September 2001). The wind speed was measured 13 times by the PIV system at a location that corresponded to 'area 3' (Figure 3.8) with no ship geometry present, i.e. not the same location as the thermal probe in the PIV 2000 experiment. The mean wind speed across the measurement area was calculated at a height of 0.5 m above the wind tunnel floor. A time series of the mean wind speed data (Figure 3.12) showed increases of up to 0.2 ms^{-1} within a period of 40 minutes. In Figure 3.12 the error bars indicate the standard error. The mean wind speed from the same location was measured during the afternoon of the first day (18th September 2001) and was included in Figure 3.12. It verifies that there were small changes of up to 0.2 ms^{-1} in the free stream wind speed as measured during either day of the PIV 2001 experiment.

In summary, the maximum possible variations in the normalised wind speed measurements during the PIV 2001 experiments are: 4 % by comparing overlapping regions, 2 % between profiles measured during the PIV 2001 experiment and 3 % by using a variable dynamic pressure. Taking the maximum error of this analysis, it can be concluded that the PIV 2001 measurements are accurate to within 4 %.

3.3 A model to quantify the effect of flow distortion at anemometer sites

3.3.1 Basic visualisation of the general flow pattern

A series of smoke tests above the bridge of the tanker (Figure 3.13) and container ship (Figure 3.14) were performed to determine the structure of the flow above the bridge of the ships. The smoke tests were performed at 5 ms^{-1} using a smoke wand to examine the flow along the centreline of the ship.

The smoke wand was moved to different heights in front of the bridge of the ships. The study showed that the general flow pattern over the bridge of the tanker behaved in a similar manner to flow over a cube [61, 62]. Flow separation at the upwind leading edge was present, with a deep recirculation region close to the bridge top (Figure 3.13a). A stagnation point about half way up the front face of the bridge was observed, with a standing vortex beneath it (Figure 3.13b). No reattachment of the flow to the top of the bridge was apparent.

In contrast, the flow above the container ship was not as well defined (Figure 3.14). It was not clear if a recirculation region close to the top of the bridge was present, or if any reattachment of the flow occurred. The smoke tracer was more turbulent and the wind speed was decelerated upwind of the bridge. This may be caused by the airflow over the front of the model separating at the leading edge of the bow and the containers (block 4, Figure 3.3), which produces a decelerated region of air close to the container top and an accelerated region above it (sketched in Figure 3.15). If the air was accelerated sufficiently it

is possible that the disturbed air flow stretched downstream of the bow and affected the flow pattern at the bridge. This is discussed further in Section 3.3.5.

3.3.2 The effect of step height on the flow over a bluff body

Figure 3.16 shows the time average of the flow over the container ship, tanker and deck house block. Velocities are illustrated by length and direction of arrows at 73×59 PIV grid points in left hand column. The measurement region is shown as a dashed box above the ship section in right hand column. The upwind leading edge is located at z=x=0. It can be seen that the size of the region where the flow is decelerated scales at least qualitatively with the step height, H, of the geometries. The container ship model step height (H=0.10 m) is defined as the height of the bridge above the containers. Likewise, the step height (H=0.29 m) of the tanker is the height of the bridge above the deck and the step height (H=0.42 m) of the deck house block is the height of the bridge above the wind tunnel floor. Vertical profiles of the wind speed were extracted from the PIV data and presented firstly at absolute distances, x, aft of the upwind edge of the bridge and then at scaled heights of z/(step height) and distances of x/(step height) back from the upwind leading edge.

The wind speed profiles were normalised using the vertical profiles of the free stream wind speed obtained in the absence of the models. The free stream wind speed field above the bridge is shown in Figure 3.17 a). The upwind leading edge of each model was located at x=z=0, 0.422 m above the tunnel floor and the direction of the flow is from left to right. The lower areas 3 and 4 were measured the day before the two higher areas. There is some inconsistency in the PIV data as the wind speeds in measurement area 3 were all spuriously high, and as consequence have been reduced by 3 % in Figure 3.17 b) to agree with the adjacent contours. At heights between the bridge top and 0.29 m above the bridge the wind speed decreases by approximately 0.3 ms^{-1} with height. This decrease is not uniform across the measurement area. The wind speed also increased by 0.3 ms^{-1}, between the upwind and down wind limits of the measurement area.

Figure 3.18 shows the vertical profiles of the normalised wind speed extracted at absolute distances aft of the upwind edge of the bridge. The vertical scale is the height above the bridge in meters. Profiles are shown at absolute distances, x, aft of the upwind edge of the bridge of a) 0 m, b) 0.09 m, and c) 0.215 m. The dashed line indicates normalised speeds of 1.0 where the measured speed equals the free stream speed. For the purposes of clarity the standard error is only displayed for every third measurement. Above the upwind leading edge of the bridge (Figure 3.18a) the wind speeds are accelerated by 10 to 20 % and do not vary a great deal with height compared with those further downwind. Further aft (Figure 3.18b) the wind speed is decelerated close to the top of the bridge, and then increases with height to a point where it is equal to the free stream flow, i.e. a normalised wind speed of 1.0. Above the decelerated region the wind speed increases rapidly to a maximum and then decreases to between 10 % to 15 % above the free stream wind speed at a height of 0.3 m. It is presumed that the wind speed will decrease further towards a free stream or undisturbed flow (a normalised wind speed of 1.0) with increasing height, although this was not measured. At the aft most position (Figure 3.18c) there is region of air flowing counter to the wind direction within the decelerated region.

Figure 3.19 shows the normalised wind speed at scaled distances of x/(step height) back from the leading edge. The scaled vertical positions of the wind speed maxima for the three geometries agree to within the measurement error and increase in scaled height with distance aft of the upwind leading edge. The magnitude of the tanker and deck house block normalised wind speed above the upwind edge (Figure 3.19a) decrease with height from roughly 1.15 to 1.05, whist the containership normalised wind speed increases with height to 1.20 at z/H=1.5. The magnitude of the maximum wind speed for the tanker and deck house blocks vary with distance from the upwind leading edge and have a maximum of approximately 1.38 at x/H=0.5 (Figure 3.19c). The maximum wind speed for the containership at these distances was generally 10 % less than the other two geometries. The thickness of the decelerated region (normalised wind speeds less than 1.0) is the same for all three geometries (Figures 3.19b, c, d), and increases in depth with distance from the upwind leading edge. There is recirculation

present in the decelerated region close to the bridge top for both the tanker and deck house geometries, but not for the container ship.

Apart from at the front edge of the bridge, it is clear that scaling all distances by the step height of the geometry successfully collapses the data from all three bodies together, and confirms the step height as the correct scaling parameter. Comparison of the profiles from all three bodies show that the line of equality (normalised speed equal to 1.0) agree to within the measurement error over all three bodies, and the height of the maximum wind speeds agree to within the measurement error over all three bodies.

The normalised wind speeds fields above the containership, tanker and the deck house block are shown in Figures 3.20, 3.21 and 3.22 respectively. In each figure the height and distance back from the upwind leading edge has been normalised by the step height, H, and the free stream direction of the flow is from left to right. The upwind leading edge was located at z/H=0=x/H. Dashed lines mark each of the four PIV measurement areas. The hatched areas in Figures 3.21 and 3.22 show a region of air that has travelled up the rear face of the cube and entered the recirculation region. Note that, because H varies, the measurement areas represent different regions of the flow for the different geometries and the figures are to different scales. The wind speeds above all three geometries in 'area 1' were unrealistically high in the bottom right hand corner. No uniform wind speed correction could be applied, as in area 3 Figure 3.11, to reconcile this wind speed increase as the normalised wind speed contours could not be aligned to the surrounding contours. This suggests that there could be a problem with the measurement of the free stream wind speed. The time average free stream wind speed (Figure 3.17) towards the bottom right of 'area 1' was slightly lower (0.2 ms^{-1}) than the surrounding air, which can account for 3 % of the increase in normalised wind speed. Variations of 0.2 ms^{-1} in the free stream wind speed are possible (Section 3.2.4) and could account for this increase in the normalised wind speed.

3.3.3 A model describing the pattern of the flow

It has been shown that the main characteristics of the flow field above the bridge are governed by the step height, H. This suggests that if the position of an anemometer on a ship is known in relation to the upwind edge of the superstructure, and the step height of the ship is known, then the effect of the flow distortion on the measured wind speed at that site can be predicted. If the step height of the ship is not known, it can be estimated from the ship's overall length using the generic merchant ship relations described in Chapter 2. This section quantifies the flow pattern above the bridge in terms of the step height.

The normalised wind speed data above each geometry were examined to determine the position of the line of equality (normalised wind speed of 1.0), and the positions of the normalised wind speed maximum and minimum. An algorithm was devised to search each smoothed vertical profile for the position of the line of equality. Points above and below 1.0 were selected and the height at which the normalised wind speed was equal to 1.0 was interpolated between these two heights. Similarly, the heights of the maximum and minimum were selected by choosing the highest and lowest wind speed from each vertical wind speed profile. The positions of the line of equality, and the maximum and minimum wind speeds above each geometry are shown against distance from the upwind leading edge in Figure 3.23. The area is divided into regions of accelerated and decelerated flow with the upwind leading edge at x/H=0=z/H. Curves were fitted to the normalised wind speed data using curve fitting software (KaleidaGraph [63]). The type of curve fit was decided from the observation of the resulting correlation coefficients, r^2. These relationships can be used to determine whether an anemometer is located within the decelerated region, the accelerated region, or is high enough to be unaffected by flow distortion.

The positions of the line of equality, and of the maximum and minimum wind speeds above each geometry agree to within z/H=0.05. The position of the line of equality above the bridge were determined from the container ship, tanker and deck house block PIV results. A curve (eq. 3.4) was fitted through the

heights at which the scaled wind speed profiles from all three flow fields cross the line of equality. The resulting equation for the line of equality is:

$$\frac{z}{H} = 0.45\left(\frac{x}{H}\right)^{0.55} \qquad \left(0 < \frac{x}{H} < 3.0\right) \qquad (3.4)$$

where z is the height above the bridge, x is the distance back from the leading edge of the bridge and H is the step height, with r^2=0.98.

The position of the wind speed maximum was obtained from the flow over the container ship, generic tanker and deck house block models. This resulting equation for the wind speed maximum is:

$$\frac{z}{H} = 0.62\left(\frac{x}{H}\right)^{0.50} \qquad \left(0 \le \frac{x}{H} \le 1.2\right) \qquad (3.5)$$

with r^2=0.95.

The normalised wind speed minima were obtained from the tanker and deckhouse data. The containership data was not used for the minimum value because of the low resolution of the data within the decelerated region. The resulting equation for the wind speed minimum is:

$$\frac{z}{H} = 0.31\left(\frac{x}{H}\right)^{0.71} \qquad \left(0 \le \frac{x}{H} \le 1.1\right) \qquad (3.6)$$

with an r^2=0.90.

The wind speed measurements above all three geometries were not high enough to determine the position at which the wind speed was unaffected by the geometry, i.e. the height above the line of equality at which the wind speed returns to the free stream value. Instead, a separate area was measured above the front edge of the tanker at approximately 0.66 m above the tanker bridge. The algorithm that determined the position of the line of equality was used, namely a normalised wind speed 1.0. A straight line (eq. 3.7):

$$\frac{z}{H} = 2.5 \qquad \left(0 \le \frac{x}{H} \le 0.5\right) \qquad (3.7)$$

indicates the height at which the acceleration of the flow reduces to the free stream (Figure 3.24). In contrast, the normalised wind speed above the container ship at a height of z/H=2.5 varies between 1.15 to 1.20 (Figure 3.20). It is not clear why the wind speed should be accelerated to this value, but it is speculated that the front of the container ship geometry may be affecting the flow above the bridge. This is discussed further in section 3.3.5.

3.3.4 Investigating the maximum wind speed

In the previous sections, simple equations have been used to predict the positions of the line of equality, and minimum and maximum wind speeds in terms of the step height, H. However, the scaled wind speed profiles (Figure 3.18) have shown that the magnitude of the container ship wind speed maximum does not agree with the other two geometries.

The magnitude of the normalised wind speed maxima for the container ship, tanker and deck house block are shown against distance from the upwind leading edge, x/H, in Figure 3.25. The upwind leading edge is located at x/H=0=z/H. The wind speed maxima for the tanker and the deck house block are similar. They increase rapidly with distance back from the upwind leading edge and reach an upper limit of 1.35 at a distance of x/H=0.3. It then reduced slowly to 1.30 at a distance of x/H=1.1. The wind speed maximum for the container ship increased less rapidly with distance back and reached an upper limit at approximately 1.30. It then reduced to 1.15 at a distance of x/H=3.0 down stream. The container ship wind speed maximum was up to 10 % less than the tanker and deck house block. These differences will be discussed in the next section.

3.3.5 The flow of air over the container ship

The previous sections have highlighted a number of differences in the air flow over the bridge of the container ship compared to the other geometries (Section 3.3.1). These problems are as follows:

i) The basic flow visualisation showed that the flow pattern in front of and above the bridge of the container ship was not very well defined (Figure 3.14).

ii) The height above the tanker bridge where the wind speed returns to the free stream is approximately z/H=2.5 (eq. 3.7). The PIV study showed that at this height the wind speed above the container ship is accelerated by between 15 % to 20 % (Figure 3.20).

iii) Although the line of equality above the container ship bridge agreed well with the tanker and the deck house block, the magnitude of the maximum wind speed was underestimated by 10 % (Figure 3.19 and 3.24).

It is hypothesised that these differences in the flow pattern above the container ship bridge are caused by the flow of air from the upwind bow reaching the bridge (Figure 3.15). The flow over the bow step is complex. The flow over the bow is either: a) effected by the height of the container top to water line, or b) the bow to waterline. Assuming eq. 3.4 holds for x/H greater than its range of limits of $(0 < x/H < 3.0)$ the depth of the decelerated region can be calculated for the airflow reaching the bridge. For example, for two forward loading container ships of length 100 m and 150 m the two bow step heights and the distance of the bridge to the container front are calculated using the linear relationships generated in Chapter 2. The heights and distances are shown in Table 3.2 along with the bridge to deck heights and the decelerated region depth. It is clear that in each case the depth of the decelerated region is roughly four to six times the bridge to deck height and hence the bridge is well down in the region of decelerated flow. An approximate extrapolation of Figure 3.23 suggests a 10 % deficit in the wind speed may explain the discrepancy in the maximum normalised wind speed

between the tanker and container ship. This will be examined further using CFD in Section 4.

3.4 The change in the airflow distortion at different relative wind directions

The effect of the airflow distortion at three different relative wind directions is investigated by examining the PIV measured flow pattern and normalised wind speed magnitude above the deck house block. Figure 3.26a) shows the positions of the line of equality and the wind speed maximum for a flow normal to the deck house block (eq. 3.4), and at wind directions of 15° and 30°. Similarly the maximum wind speed magnitude is shown in Figure 3.26b). In general, there is good agreement in the pattern of the flow and the wind speed magnitude (< 2 %) for flows within ±15°. At a wind direction of 30° there is a variation of within 5 % in the magnitude of the wind speed maximum for x/H>0.25. It must be noted that as the relative wind direction from the bow, ϕ, increases the distance of the anemometer position from the upwind leading edge, x, will increase to $x/\cos(\phi)$ (schematic Figure 3.26). Assuming H is constant for the case of the simple block the depth of the decelerated region will increase with increases in x/H (Figure 3.26a). In general the wind speed magnitude varies by up to 5 % with increasing x/H (Figure 3.26b). It is unknown if the step height, H, of a real ship will vary with increasing relative wind direction, e.g. whether at ϕ=30° H will be the bridge to deck height or the bridge to waterline height. No wind tunnel studies of the tanker or container ship were performed at different wind directions.

3.5 Summary

The aim of this chapter was to derive a way to predict the flow of air above the bridge using information about the ship type and size. Wind tunnel studies of simple representations of bluff body generic VOS ship shapes were used to derive scaling rules that predict the extent of the accelerated and decelerated regions of air flow above the bridge of the ships. The scaling rules are only applicable for flows directly over the bow of VOS ships and for anemometers located on the

ships centreline. However this is likely to be the case for high proportion of observations. It was found that:

3a) The flow field scales with the step height, H, of the model. In the case of a tanker and container ship, H is the bridge to deck and the bridge to container top heights respectively.

3b) Equations describing the positions of the line of equality (eq. 3.4), wind speed maximum (eq. 3.5) and minimum (eq. 3.6) have been described. Based on the scatter of the data these equations are accurate to within z/H=±0.025 (±0.35 m for a tanker of length 170 m).

3c) Close to the bridge top, the airflow was severely decelerated and may even reverse in direction. The decelerated region is bounded by the line of equality, where the normalised wind speed (measured/undistorted) has a value of 1.0. Depending on position, the airflow above the line of equality is accelerated by up to 38 %.

3d) Close to the line of equality the normalised wind speed varies between 0.2 to 1.1 (Figures 3.19, 3.20, 3.21). Such a large gradient suggests positions along the line of equality are not the ideal position to locate an anemometer.

3e) The effects of airflow distortion reduce with increased height, and the acceleration of the flow decreases to the free stream at z/H=2.5 for the tanker geometry.

3f) The magnitude of the maximum wind speed for the container ship is 10 % less than the tanker geometry, and the height that the wind speed returns to the free stream does not agree with the tanker. Therefore a separate model may be necessary to predict velocity changes over the container ships.

In summary, the results and developed methodology makes it possible to estimate the sign and magnitude of the bias in wind speed measurements, obtained at the predominant relative wind direction, from an anemometer located on or near the centreline of a Voluntary Observing Ship. This will rely on a knowledge of the anemometer position and a basic ship dimension (e.g. the bridge to deck height, or the length overall allowing the bridge height to be determined). The following chapters apply CFD techniques to support and broaden the application of the experimental measurements.

4. CFD SIMULATIONS OF THE FLOW OVER THE GENERIC SHAPES

4.1 Introduction

The use of wind tunnels can be costly and time consuming, and the studies may be limited by the wind tunnel speed and the physical size of the model. It is also impractical to model a large number of ships in a wind tunnel. With the continual increases in computing power, Computational Fluid Dynamics (CFD) has become a viable alternative for modelling the air flow over ships. The aim of this chapter is to test the performance of a commercial CFD code, VECTIS, in modelling the flow over bluff body merchant ships. The CFD code VECTIS used in this study will be detailed in Section 4.2.

As already stated in the literature review, previous numerical studies of the flow over ships have mainly concentrated on research ships (Moat and Yelland [23 to 28]; Yelland et al. [9, 29]). In all cases the ship geometries were detailed, and the anemometers were well exposed and had low flow distortion. In contrast, the generic merchant ship geometries used in the present study are simple bluff body structures. The anemometers may not be well exposed and could have high flow distortion.

Many experimental studies of the flow over bluff bodies have been performed for the purpose of validating of CFD codes. However, these were either not unbounded flows (e.g. Martinuzzi and Tropea, [64]), or did not measure the velocity in sufficient detail in the areas of interest to enable a comparison to be made (e.g. Minson *et al.* [65]; Cheney and Zan, [32]). These are therefore not suitable for direct comparison with the wind tunnel results (Section 3). However Martinuzzi and Tropea, [64] and Minson *et al.* [65] are used in Section 4.3 for partial validation of the performance of the CFD code VECTIS in modelling the flows over bluff bodies.

The accuracy of CFD codes are significantly dependent upon the choice of turbulence closure scheme, the numerical schemes and the mesh design (Cowan, *et al.* [66]). Therefore Section 4.4 examines various VECTIS simulations of the

flow over the full-scale generic tanker (of length 170 m) in terms of their dependence on mesh density, turbulence closure schemes, inlet profile definition, and the scale of the geometry. The results of Section 4.4 are compared in Section 4.5 to the PIV measurements of the flow over the tanker.

It was shown in Chapter 3 that the magnitude of the wind speed maximum above the container ship was less than that of the tanker and deck house block. It was postulated that this was due to the air flow over the upwind bow step effecting the airflow reaching the bridge. CFD simulations of the flow over the wind tunnel scale models of the tanker, container ship and deck house block are performed in Section 4.5 to test this hypothesis. These simulations were performed at the same Reynolds number (1.8×10^6) as the PIV wind tunnel studies.

4.2 The CFD code VECTIS

4.2.1 Introduction

CFD is a method to calculate the flow of a fluid by means of computer based simulation. All CFD codes contain three main elements: i) a pre-processor stage where the geometry (Section 4.4.2), mesh, and boundary conditions are defined (Section 4.2.3); ii) a solver stage where the equations governing the fluid flow are solved (Section 4.2.4); and iii) a post processing stage where the flow field can be analysed for convergence and data can be extracted (Section 4.2.5). The commercially available finite volume CFD code VECTIS (Ricardo, [67]) was used to calculate the velocity field over the bluff body geometries presented in this chapter.

This code was originally chosen and used since 1993 to calculate the wind speed over a variety of very detailed research ship geometries (Moat and Yelland [23 to 28] and results have been compared to previous wind tunnel studies [9] and *in situ* wind speed data [29]. Its main advantage is a sophisticated automated

mesh generation feature that allows fast mesh generation (within hours) around a complicated geometry.

VECTIS calculates the 3-dimensional, compressible, steady state solutions of the Navier-Stokes continuity and energy equations (Versteeg and Malalasekera, [68]). The governing equations of fluid flow (APPENDIX A.1) cannot yet be solved efficiently for high Reynolds number flows. Therefore, the governing Navier-stokes equations are time, or Reynolds, averaged which introduces unknown turbulence correlation terms which render the equations insoluble. These Reynolds (or turbulent) stress terms have to be parameterised by a turbulence closure scheme. The VECTIS solver is second order accurate and uses finite-difference-type approximations for the terms representing flow processes such as convection and diffusion. The differencing schemes used are stated in Section 4.2.4b. Even though the CFD solutions are modelled at sufficiently low wind speeds (order 10 ms^{-1}) that density changes are minimal, a compressible solution is always specified since this produces a more stable solution [69]. All the flow simulations performed using VECTIS were isothermal, i.e the air, ship sides and decks, and the sea surface were set at a constant temperature of 20 °C.

4.2.2 Geometry creation

The simple 3-dimesional bluff body shapes of the generic merchant ships were created using the pre-processor FEMGEN [70]. The ship geometry was then enclosed in a computational domain or wind tunnel (Figure 4.1). The width of the volume was chosen to minimise the blockage of the flow in the domain by the ship [18]. No blockage correction was applied as the blockage ratio (frontal area of the ship : area of the of domain cross section) was approximately 0.5 % for all full-scale simulations.

4.2.3 Boundary conditions and mesh generation

The flows over the full-scale generic ship geometries (of length 170 m) were modelled using a thick planetary boundary layer wind speed profile at the inlet boundary. The inlet profile of the tanker model did not match that measured in the wind tunnel, since the latter varied both in shape and in magnitude (Chapter 3.1), but was representative of profiles found over the open ocean. The wind speed profile varied logarithmically with height, z, and was defined using:

$$U_{zN} = \frac{u_*}{k_v} \ln\left(\frac{z}{z_0}\right) \tag{4.1}$$

where u_* is the friction velocity, k_v, is the von Kármán constant (0.4) and z_0 is the roughness length. Assuming an open ocean wind speed of U_{zN}=10 ms^{-1} at a height of 10 m, the wind speed profile can be defined by eq. 4.1 by calculating values u_* and z_0. The friction velocity, u_*, was calculated using:

$$u_*^2 = C_{D10N} U_{10N}^2 \tag{4.2}$$

where C_{D10N} is the drag coefficient which varies with wind speed and is defined in eq. 1.1. The subscripts 10 and N refer to a height above the sea surface of 10 m, and equivalent neutral stability conditions. The roughness length, z_0, can be calculated by combining eq. 4.1 and 4.2:

$$z_0 = \frac{10}{\left(e^{\frac{k_v}{\sqrt{C_{D10n}}}}\right)} \tag{4.3}$$

using the using the value of C_{D10n} calculated from eq. 1.2, z= 10 m and U_{10N}=10 ms^{-1}.

At a solid boundary there is a thin boundary layer in which the velocity increases rapidly from zero at the surface and approaches the velocity of the main stream. Immediately adjacent to a solid wall, an extremely thin viscous sub-layer exists and has a turbulent region above. The number of mesh points

required to resolve all the details in a turbulent boundary layer would be prohibitively large and CFD employs a wall function [68] to represent the effect of the wall boundaries. In all the CFD models, the wind tunnel floor and ship sides were specified as a solid wall with a roughness length, z_0, similar to that of the open ocean (10^{-4} m) [71]. The sides and roof were defined as zero gradient walls, i.e. the walls were defined with a slip condition and therefore produced no boundary layers. The outlet wind speed profile was determined from the flow upstream of the boundary, whilst maintaining a mass flow rate identical to that at the inlet boundary.

VECTIS uses a non-uniform Cartesian mesh and can increase the number of cells in specific areas of interest whilst minimising the number of cells at large distances from the ship where the flow does not vary a great deal. The cell size was defined by specifying the number of gridlines in each of the co-ordinate directions. The cell size was reduced in specific locations of interest by subdivision of each existing cell into 4 sub-cells in each co-ordinate direction (64 cells for each cell volume). Finally, all cells which bisect a boundary were automatically truncated to conform exactly to the shape of the boundary. This enabled the exact shape of the geometry to be preserved.

The number and size of cells within the computational domain varied between CFD models (Table 4.1). The models were limited to 270,000 cells or less until a dual processor Silicon Graphics Origin 200 UNIX workstation was purchased in January 2000.

4.2.4 The VECTIS discretisation

4.2.4a Turbulence closure schemes

The most widely used turbulence closure schemes available in commercial CFD codes are Eddy Viscosity Models (EVM). The unknown turbulence correlation terms generated by the Reynolds averaging are calculated from the eddy viscosity using the Boussinesq relationship (APPENDIX A.2 and [68]).

VECTIS uses either the $k \sim \varepsilon$ parameterisation [68] with standard coefficients (Launder and Spalding, [72]), or a Re-Normalisation Group (RNG) based $k \sim \varepsilon$ parameterisation (Yakhot *et al.* [73]). No other turbulence closure schemes are available in the code and therefore will not be discussed. In the $k \sim \varepsilon$ parameterisation two transport equations are solved, one for the turbulent kinetic energy, k, and a further one for the rate of dissipation of turbulent kinetic energy, ε. Both are related to the eddy visocity via:

$$\mu_t = \rho C_\mu \frac{k^2}{\varepsilon} \tag{4.4}$$

where μ_t is the eddy viscosity, ρ is the air density and C_μ is a dimensionless constant the value of which changes between the two parameterisations [74]. The $k \sim \varepsilon$ parameterisation is known to overestimate k in regions of high rates of strain [75 to 78] and thus increase the value of the eddy viscosity calculated via eq. 4.4. The RNG $k \sim \varepsilon$ parameterisation is a variant of the $k \sim \varepsilon$ parameterisation and is known to reduce the over estimation of k in regions of high rates of strain, such as the upwind leading edge, by increasing the rate of dissipation [31].

Although EVMs have many flaws in predicting the turbulent statistics, Murakmi and Mochida [79] state that the $k \sim \varepsilon$ parameterisation reproduced the mean velocity and pressure fields well when a fine mesh resolution is used. Easom [80] compared the CFD solutions of the flow over a 6 m cube using the RNG $k \sim \varepsilon$ parameterisation and the standard $k \sim \varepsilon$ parameterisation. Easom reported that the RNG $k \sim \varepsilon$ parameterisation was more accurate in predicting the pressure field on the cube roof than the $k \sim \varepsilon$ parameterisation and was generally as accurate as higher order closure models, while having with less computational cost and greater stability. Both turbulence schemes will be used to determine the velocity field above bluff body merchant ships in Section 4.4.

4.2.4b Differencing schemes

The VECTIS code used a second order accurate differencing scheme (Zhu and Rodi [81]) to approximate the advection and diffusion of the fluid motion.

Zhu and Rodi [81] claim that the scheme is equivalent in accuracy and stability to the QUICK [82] scheme, in addition to being highly effective at suppressing the overshoots that can occur with QUICK. A first-order accurate upwind differencing scheme (Spalding [83]) was used for the pressure equation, the turbulent kinetic energy (k) and the rate of dissipation of turbulent kinetic energy (ε). No other higher order differencing schemes were available in the code and therefore will not be discussed.

The velocity field has to be linked (or coupled) to the pressure field to calculate a velocity field that satisfies continuity of mass. For steady state flows Ricardo [67] recommends that the PISO algorithm [68] be used for this. This is an iterative method that on the first step of the iterative process predicts the velocity field from the existing pressure field. This first prediction of the velocity field will not satisfy continuity, and a pressure correction field is obtained and used to correct the velocity and pressure fields. As opposed to other algorithms PISO then applies a second pressure correction field to improve the accuracy of the velocity field further still. The process is iterated until the pressure field applied to the momentum equations produces a velocity field that satisfies continuity.

4.2.5 Model convergence

The velocities at a number of locations within the computational domain were monitored until the variations in velocity were less than 1×10^{-4} ms^{-1}. In the full-scale CFD simulations the monitoring locations were close (50 m) to the tunnel sides except for one within the region of interest, such as above the bridge of a ship. Generally the models took 20,000 time steps (up to 3 to 4 weeks of processing time) on an Origin 200 UNIX workstation to converge. The speed of the free stream flow was determined using a vertical profile of the wind speed at a point well abeam (more than 100 m) of the site of interest.

4.3 Comparison of VECTIS with previous wind tunnel studies of the flow over cubes

4.3.1 Introduction

Two tests cases were used to validate the CFD code VECTIS for air flows over bluff bodies. Both are wind tunnel studies of the flow over surface mounted cubes and both were obtained from the European Research Community on Flow, Turbulence and Combustion (ERCOFTAC) data base[4]. The first case is a fully developed channel flow, and the second is a boundary layer flow. CFD was used to simulate both flows and the results were then compared to the wind tunnel measurements.

4.3.2 Channel flow over a cube

Martinuzzi and Tropea [64], placed a surface mounted cube with a height H, of 0.025 m, in a closed channel of 0.05 m (2H) in height and 0.6 m in width. A blower-type wind tunnel was used to simulate a fully developed channel flow over the cube, with a inlet velocity of 25 ms^{-1}. The Reynolds number, based on the channel height, was $R_e = 10^5$. Measurements of the velocity above the cube were made using a three-beam, two component Laser Doppler Anemometer (LDA). This experiment was re-created numerically using the CFD code VECTIS (Figure 4.2). The upstream profile measured by [64] was approximately parabolic with a maximum velocity at height H. This profile was used as the inlet boundary condition for the computational domain, and matched the closed channel wind tunnel exactly. The turbulent kinetic energy, k, and the rate of dissipation of turbulent kinetic energy, ε, at the inlet were defined as 2.4 m^2s^{-2} and 0.017 m^2s^{-3} respectively. Two CFD simulations were performed, one using the $k \sim \varepsilon$ turbulence parameterisation with standard coefficients and the other the RNG $k \sim \varepsilon$ turbulence parameterisation.

---

[4] Based at the Department of Mechanical Engineering, University of Surrey, UK.

Both simulations used the same mesh of 243,696 cells. The RNG $k \sim \varepsilon$ parameterisation was also run using a finer mesh of 519,886 cells to determine the sensitivity of the solution to the mesh density. The minimum cell size used above the cube in the coarse grid model was 0.024H and in the fine grid model was 0.016H. Figure 4.3 shows the vertical profiles of the total velocity measured above the centerline of the cube, both from the wind tunnel and from the three CFD simulations. The minimum cell sizes are displayed in the legend. All velocities were normalised by the average inlet velocity of 25 ms^{-1} and all heights were normalised by the cube height, H. Five profiles are shown; one at the upwind leading edge of the cube, one at the rear edge and the other three spaced equally between these two.

The wind tunnel measurements show flow separation behind the leading edge with strong re-circulation close to the cube top. Within the re-circulation region the minimum wind speed occurs at a height of about z/H=0.15, half way back from the leading edge (Figure 4.3c). The height where the total velocity equals the free stream velocity (at a normalised wind speed of 1.0) varies from just above the leading edge and increases with distance downstream, reaching a height of z/H=0.3 at a distance of x/H=1.0 (Figure 4.3e). Above this 'line of equality' the flow is accelerated, except close to the channel roof. The maximum normalised velocity of 1.4 occurs at a distance of x/H=0.5 downstream of the leading edge at a height of z/H=0.35. The height of the maximum also increases with distance downstream.

Examining the results from the CFD model using the 0.024H mesh and the standard $k \sim \varepsilon$ turbulence parameterisation, it can be seen that this model performs quite well in simulating the shape of the accelerated region and the position of the maximum velocity. However, the model underestimates the maximum normalised velocity by up to 0.1, i.e. a maximum normalised velocity of 1.3 rather than 1.4. In the region below the line of equality this model does not perform well and as opposed to the wind tunnel measurements a separation bubble is formed and the flow re-attaches to the cube top at x/H=0.75.

The results from the CFD model using the 0.024H mesh and RNG $k \sim \varepsilon$ turbulence parameterisation show better agreement with the experimental data than the standard $k \sim \varepsilon$ parameterisation. Except for the leading edge (where both CFD models overestimate the velocity), the RNG $k \sim \varepsilon$ coarse model simulates the shape and position of the accelerated region better than the standard $k \sim \varepsilon$ parameterisation, and only underestimates the maximum normalised velocity by 0.05 or less. Below the line of equality the RNG $k \sim \varepsilon$ turbulence parameterisation performs much better than the standard $k \sim \varepsilon$ parameterisation, with a more realistic recirculation pattern which only disagrees significantly with the wind tunnel results very close to the surface of the cube.

The CFD model using RNG $k \sim \varepsilon$ closure was run a second time using a finer mesh of minimum cell size of 0.016H in order to examine the dependence of the solution on mesh density. This produced rather mixed results. Except at the leading edge, the model underestimated the maximum normalised wind speed by up to 0.15, i.e. a simulation based on a minimum cell size of 0.016H gave worse results than those based on the coarse mesh models. This was experienced by [66] in simulating the airflow around a bluff-body building using CFD. Cowen [66] attributed the disagreement to inaccuracies created by the discretisation of the advection and diffusion terms. It was not possible to investigate this disagreement in the results since no other differencing schemes (Section 4.2.4b) are available in VECTIS. Below the line of equality the performance of this model in simulating the flow in the recirculation region was an improvement on the standard $k \sim \varepsilon$ parameterisation but not as good as the coarser mesh RNG $k \sim \varepsilon$ parameterisation. At the leading edge, the 0.016H mesh RNG $k \sim \varepsilon$ parameterisation performed the best of all three CFD runs, in that it produced a smaller overestimate of the maximum velocity.

To summarise, these comparisons showed that the CFD models of the channel flow over a cube performed reasonably well above the recirculation region with a maximum underestimate of the absolute velocity of between 4 and 12 % aft of the upwind leading edge of the cube, and a maximum overestimate of about 6 % at the leading edge itself. The size of these errors depended upon the

mesh density and the turbulence closure used, but in general the differences between the three CFD models were small. The worst performing CFD model was the 0.016H mesh using the RNG $k \sim \varepsilon$ closure, which suggested a maximum acceleration of the flow of about 25 % rather than the 40 % suggested by Martinuzzi and Tropea [64] data. Overall the 0.024H mesh RNG $k \sim \varepsilon$ model performed best, closely simulating the shape of the accelerated flow region and predicting a maximum acceleration of 35 %, which was reasonably close to the maximum observed in the wind tunnel.

4.3.3 Boundary layer flow over a cube

Minson et al. [65] examined a boundary layer flow over a surface mounted cube of 0.2 m in height (H), in the 4 m by 2 m environmental wind tunnel at the University of Oxford. The Reynolds number in the wind tunnel, based on the cube height, was 7.7×10^4. The boundary layer flow was normalised by a reference velocity of 5.4 ms^{-1}, measured upstream of the cube at height, H. A 2-component LDA measured the velocity components above the cube.

VECTIS CFD models were used to simulate the air flow through the wind tunnel (Figure 4.4). Velocities around the cube were calculated using both the standard $k \sim \varepsilon$ and the RNG $k \sim \varepsilon$ turbulence parameterisations, each based on a mesh of 280,180 cells. The minimum cell size in the region of interest above the cube was very similar to the grid used in the CFD study of channel flow (Section 4.3.2) and corresponded to 0.023H. For both models the vertical profiles of velocity above the cube were compared to those obtained by [65] (Figure 4.5). In Figure 4.5 the minimum cell sizes are displayed in the legend.

The wind tunnel studies show flow separation behind the upwind leading edge with a recirculation region reattaching to the cube top at a distance of x/H=0.3. Unfortunately the measurements of [65] were not very extensive, with only four measurements per profile between the cube top (z/H=0.0) and height z/H=0.12. A total of only three measurements (Figures 4.5a and b) were made above the line of equality. Nevertheless, the model using the RNG $k \sim \varepsilon$

turbulence closure reproduces the flow pattern in the recirculation region very well. In comparison to the boundary layer flow over the cube the channel flow does not reattach to the cube top and has a far stronger recirculation region (Figure 4.5 f).

4.3.3a The effect of normalising on the wind speed measurements

The CFD simulation of the boundary layer flow over the cube has shown that increases of approximately 1.3 are possible when the wind speed profiles above the cube are normalised by a fixed wind speed of 5.4 ms^{-1}. This normalising method will not produce an absolute wind speed difference from the free stream as the actual free stream wind speed is not constant, but increases with height. Therefore, normalising the wind speed profiles using a wind speed measured at the height of the cube top will lead to an overestimate of the normalised wind speed above the cube. For example, when the RNG $k \sim \varepsilon$ CFD model wind speed profiles were normalised by the boundary layer profile at the inlet and the wind speed maxima were reduced to between 1.10 to 1.15, i.e. a consistent reduction of about 20 %. All wind speed profiles detailed in this thesis were normalised by the actual free stream profiles to avoid the possible overestimates that can be caused by normalising by fixed wind speeds.

4.3.4 Summary

In the channel flow comparison, the VECTIS standard $k \sim \varepsilon$ scheme failed to simulate the flow separation and recirculation, whilst the CFD model using the RNG $k \sim \varepsilon$ turbulence closure agreed well with the measurements of [65] in the recirculation region for a minimum mesh of size 0.024H. The channel height was only twice the height of the cube, therefore large increases (of up to 40 %) in wind speed are expected as the air is constricted between the cube top and the tunnel roof and is not comparable to the later studies of the flow over merchant ships.

Unfortunately, the boundary layer study of flow over a cube [65] did not possess many measurements within the accelerated region above the line of equality. However, the study did show that the maximum normalised wind speed was reduced from about 1.30 to between 1.10 to 1.15 when the wind speed profiles were normalised by the free stream boundary layer profile, in the absence of the model, instead of a fixed wind speed.

4.4 VECTIS models of the generic tanker shape

4.4.1 Introduction

A number of CFD simulations (Table 4.1) of the flow over the generic VOS tanker (of length 170 m) were made in order to examine the dependence of the CFD results in terms of:

1) the dependence of the models on mesh density (Section 4.4.2a).

2) the effect of different turbulence closure models on the solution accuracy (Section 4.4.2b).

3) the shape of the inlet wind speed profile (Section 4.4.2c).

4) the size of the geometry and the effect of the dimensionless distance y^+ (Section 4.4.2d).

In all cases the vertical profiles of the velocity were normalised by the free stream, or undisturbed, vertical profile of velocity 200 m abeam of bridge of the ship. All figures show the normalised wind speed profiles at various distances aft of the upwind edge of the bridge. All distances have been normalised by the step height, H, (bridge to deck height of 13.54 m) of the tanker model.

4.4.2 CFD models of the full-scale tanker

4.4.2a The mesh dependence of the full scale solutions

Three CFD simulations of the 3-dimensional flow over the tanker were made to test the dependence of the solution on the mesh size. Mesh sizes of: 1) 147,293 (RUN A), 2) 270,305 (RUN B) and 3) 427,230 (RUN C) were compared. The RNG $k \sim \varepsilon$ turbulence closure scheme and the boundary conditions defined in Section 4.2.3 were used in all three simulations. The minimum cell size (mesh resolution) of each mesh are indicated in Table 4.1 and ranged from 0.04H to 0.018H. The minimum cell size for RUN A (0.04H) and B (0.038H) were similar because the mesh density in RUN B was mainly increased in other regions of the ship. These regions included the areas in front of and behind the bridge, and in the region around the upwind bow step. This was applied to give a better simulation of the flow over the whole ship. The change in the mesh density around the bridge of these two models is shown in Figures 4.6 and 4.7. RUN C included the refinements in RUN B and had increased cell resolution above the bridge.

Figure 4.8 shows the vertical profiles of the normalised velocities obtained above the bridge of the three CFD tanker simulations using the three different mesh densities. The minimum cell sizes are displayed in the legend. The normalised profiles calculated using RUNS B and C agreed to within 1 %, at distances of less than x/H=0.75 back from the front edge of the bridge. The solution based on the 0.04H mesh (RUN A) agrees with the other simulations on the height of the line of equality, but does not agree with the other models in the position and magnitude of the wind speed maximum. The differences are largest around the upwind leading edge of the bridge. For example, at a distance of x/H=0.25 downstream of the upwind leading edge the normalised wind speed profile simulated on the 0.04H mesh increases to a maximum normalised wind speed of 1.07 at a height of z/H=0.2, whereas the simulations based on higher mesh resolutions predict a maximum normalised wind speed of 1.04 at a height of z/H=0.5. The normalised wind speed profile based on the 0.04H mesh was

unrealistic. At all distances back from the leading edge the wind speed increases to a maximum, decreases rapidly and increases to another wind speed maximum and then decreases in a similar manner to the other normalised wind speed profiles.

From comparing the normalised profiles it was clear that the flow field above the bridge is better represented by not only reducing the cell size above the bridge, but also increasing the cell density around the bridge and at the upwind bow step. The CFD solutions are effectively mesh independent for a minimum cell size of 0.038H above the bridge.

4.4.2b The dependence of the full-scale solutions with turbulence closure

Two CFD simulations of the flow over the tanker using the RNG $k \sim \varepsilon$ (RUN C) and $k \sim \varepsilon$ (RUN D) turbulence closure schemes were compared. Both simulations used an identical mesh of 427,230 cells and used the same boundary conditions (Table 4.1). The minimum cell size used above the bridge of the tanker was 0.018H. Figure 4.9 shows the vertical profiles of the normalised velocities obtained above the bridge of the two simulations. The minimum cell sizes are displayed in the legend.

Figure 4.9 shows that both CFD simulations give very similar results for the general flow pattern. Above the decelerated region the wind speed is accelerated to a maximum at about z/H=0.5, and then decreases again with increasing height to a point where it equals the free stream value. A line of equality, where the measured speed equals the free stream, separates the decelerated and accelerated regions. Apart from around the leading edge, where the $k \sim \varepsilon$ turbulence closure is known to overestimate k [75 to 78] and hence the eddy viscosity (eq. 4.1), there is little change (within 2 %) in the solutions calculated on the same mesh with the two different turbulence parameterisations. However, the RNG $k \sim \varepsilon$ parameterisation gave a better prediction of the wind speed in other bluff body comparisons (Section 4.3) and it is recommended that this closure scheme be used for future CFD models.

4.4.2c Inlet profile specification

The effect of the shape of the inlet profile on the flow field above the bridge was examined. A further CFD model (RUN E) simulated the flow over the tanker with the inlet profile specified as a uniform profile at 10 ms^{-1}, instead of a boundary layer profile which varied with height (Section 4.3.3). With the exception of the inlet velocity profile the CFD simulation was identical to RUN C, i.e. the model used a mesh of 427,230 cells and the RNG $k \sim \varepsilon$ turbulence closure (Table 4.2).

Figure 4.10 shows the vertical profiles of the normalised velocities obtained above the bridge of the two CFD tanker simulations using a uniform and a boundary layer profile. The minimum cell sizes are displayed in the legend. There is an increase of approximately 3 to 4 % when a uniform profile at the inlet is used.

4.4.2d The scaling of the bluff body tanker

The flow simulations in Section 4.4.2 have not defined a small enough absolute mesh size to accurately define the thin boundary layer profile very close to the bridge surface. The velocity at the surface will be zero and increases with height to the value of the main stream flow.

Examination of the value of the dimensionless distance y^+ showed the near wall cells were too large (Table 4.1) for the cell centres to be in the log-law region of the turbulent boundary layer, i.e. the velocity profile close to the wall is not logarithmic (the law of the wall does not hold). y^+ is defined as:

$$y^+ = \frac{\Delta y_p}{\nu}\sqrt{\frac{\tau_w}{\rho}} \qquad (4.1)$$

where Δy_p is the distance of the centre of the near wall cell to the surface, ν is the kinematic molecular viscosity, τ_w is the wall shear stress (assumed to be entirely viscous in origin) and ρ is the density. Ideally, the value of y^+ should

be greater than 11.63 [68] and less than 10^3 [84] for the near wall cells to be in the log-law region of the turbulent boundary layer. The near wall flow is taken to be laminar if $y^+ \leq 11.63$. The number of cells needed by VECTIS to achieve this could not be reached for a full-scale model using the computing power available. Instead, a CFD simulation of the flow over a scaled tanker geometry was performed. The Reynolds number (eq. 3.1) based on the bridge to deck height of this flow for this simulation was 6.3×10^5, and was equivalent to the wind tunnel simulations (Table 3.1).

The mesh and geometry of the RUN C flow simulation was scaled down in size by a ratio of 1:96. An additional simulation (RUN F) was performed at this scale to determine what effects this scaling had on the flow pattern above the bridge. The lower 2.0 m of the boundary layer profile (Section 4.2.3) was used to define the wind speed at the inlet. The step height was reduced to H=0.14 m. The reduction in the mesh size produced an absolute mesh size of 0.003 m above the bridge and the value of y^+ was reduced to between $20 < y^+ < 100$ on the surface of the bridge top. Figure 4.11 shows the vertical profiles of the normalised velocities obtained above the bridge of the RUN C and scaled RUN F simulations. The minimum cell sizes are displayed in the legend.

Comparison of the normalised wind speed profiles in Figure 4.11 show that the general shape of the profiles agree and that scaling the tanker model increases the maximum wind speed by approximately 2 %. Therefore, CFD simulated wind speed profiles based on the same mesh and turbulence closure scheme are generally independent of the geometry scale. This suggests that the value of y^+ has little effect on the shape of the profile above the bridge.

4.4.3 Summary

Various parameters have been examined to determine their impact on the VECTIS solution accuracy. Apart from at the leading edge, changing the various parameters does not alter the predicted position of the line of equality, but the magnitude of the normalised wind speed maximum is altered slightly. The

change in the normalised wind speed maximum by parameters are: using cell sizes of less than 0.038H (<1 %); the turbulence closure scheme (< 2 %); and the scaling of the geometry (< 3 %). The most important factor is the specification of the inlet wind speed profile, which increases the magnitude of the wind speed maximum by up to 4 %.

Figure 4.12 overlays the CFD results from Figures 4.8 to 4.11 and the maximum and minimum limits of the normalised predicted wind speeds are shown as hatched regions. At the upwind leading edge there are variations of up to 20 % in the CFD predicted wind speeds. This variation decreases to 4 % (Figure 4.12d) with distance back from the upwind leading edge. The maximum predicted normalised wind speed is 9 % at a distance of x/H=0.25 back from the upstream leading edge.

4.5 The effect of ship type on the airflow: CFD at wind tunnel scale

4.5.1 Introduction

The effect of ship type, or shape, on the normalised wind speed above the bridge was investigated by comparing ship geometries of the size used during the PIV experiment (Chapter 3). The flow over scaled geometries was used instead of full-scale geometries because an increased mesh resolution could be used to model the flow whilst run times were reduced by three-quarters. This is a valid method to reproduce the full-scale flow, as simulating the flow over a scale model of the geometry has been shown to reproduce the full-scale flow to within 2 % in Section 4.4.2d using a step height greater than H= 0.14 m. The aim of this section was to: 1) compare the flow pattern above each ship type, and 2) determine the effect of the airflow over the bow on the flow above the bridge of the container ship.

4.5.2 Description of the CFD models

Unbounded flows over the wind tunnel scale container ship, tanker and deck house block were modelled. The step heights of the container ship (Figure 3.1), tanker (Figure 3.2) and deck house block (block 1, Figure 3.1) were H=0.106 m, H=0.294 and H=0.422 respectively. The flow over the ship geometries were simulated using the same wind speed and turbulent intensity as the wind tunnel. The inlet profile was a uniform profile of 7 ms^{-1} and the turbulent intensity was 0.2 % of the wind tunnel speed [85]. The simulations used the RNG $k \sim \varepsilon$ turbulence parameterisation and the total number of cells was between 485,669 and 692,638 (Table 4.2). The minimum cell size above the bridge was far smaller (0.031H to 0.008H) than the full-scale CFD models and therefore mesh independent solutions for each CFD model was assumed. The size of the computational domain (Figure 4.13) is approximately the same length as the Southampton University wind tunnel, but had the roof and side walls extended by 10 m to give a blockage ratio (frontal area of the geometry : area of the domain cross section) of less than 1 %. The distance of the inlet to the bow of the tanker and container ship geometry was increased to 8.7BH to allow the flow to be fully developed before reaching the ship. The distance of the inlet to the deck house block was 10BH. The distance of the outlet from the aft end of the ship geometries was 6BH in all three models. A roughness length of $z_0 = 1 \times 10^{-5}$ m was used for the surfaces of the wind tunnel floor and the ship. In all cases the vertical profiles of the velocity were normalised by the free stream, or undisturbed, vertical profile of velocity 8.5 m abeam of bridge of the ship.

4.5.3 Comparison of the flow above different ship types

The vertical profiles of the normalised wind speed above the bridge of the tanker, container ship and deck house block are shown in Figure 4.14. The minimum cell sizes are displayed in the legend. The depth of the recirculation region increases with distance from the upwind leading edge and is located at equivalent heights for the tanker and deck house block geometries. The normalised wind speeds above the tanker and deck house block reach a maximum

normalised wind speed of 1.11 and 1.14 at distances of x/H=0.5 and x/H=0.25 respectively. The normalised wind speed for each ship then decreases slowly with distance back from the front edge.

The depth of the recirculation region for the container ship is far deeper than the other two ship geometries. It is located at an approximate height of z/H=1.0 for all distances back from the upwind leading edge. This result is not consistent with the PIV results, but shows that the air flow over a container ship does behave in a different manner to the tanker. The normalised wind speeds above the bridge of the container ship increased rapidly in height from the line of equality to a wind speed maximum at heights of z/H=1.5. The magnitude of the wind speed increases from 1.03 at the leading edge to 1.07 at a distance of x/H=0.75 down stream.

4.5.4 Investigation into the optimum outlet distance

For accurate CFD solutions the outlet must be placed far enough from the obstacle that the flow has achieved a fully developed state [68]. A sensitivity study to determine any possible change in the normalised wind speed above the deck house block with change in distance from the deck house block to the outlet was performed. The deck house block was positioned 6BH downstream of the bluff body and 10BH from the inlet. The outlet distance was increased to $18 \times$BH and a CFD model was performed, but no change in the flow field above the deck house block was evident. The result remains steady for solutions with an outlet distance greater than 6BH.

4.5.5 The effect of the upwind bow step on the flow pattern above the bridge

It was hypothesised in Chapter 3 that the airflow above the bridge was affected by the flow of air over the upwind bow. Section 3.3.5 details a hypothesis that the underestimate of the wind speed maximum above the container ship bridge was caused by the bridge being in a region of decelerated air. In addition the PIV studies showed that the height above the tanker bridge that the

wind speed returns to the free stream value is z/H=2.5, but at this height the wind speed above the container ship is accelerated by 15 % to 20 %. This section compares the general flow pattern over all three geometries using the wind tunnel scale CFD container, tanker and deck house block models to examine the effect of the flow over the bow step on the wind speed above the bridge.

Figure 4.15 shows the wind speed over the wind-tunnel-scale container ship, tanker and deck house block. The pattern of the flow over the container ship bow step was similar to the flow over the bridge, i.e. the flow of air separates at the upwind leading edge and a region of accelerated air was created (Figure 4.15a). However in this case the air was accelerated again (up to 20 %) as it passes over the second step which was the leading edge of the containers. This accelerated air then travels down stream along the container top and the region of air moving at speeds greater than 7 ms^{-1} extend to 3/4 of the length of the container ship top before reducing to wind speeds of less than 7 ms^{-1}. Below the accelerated region the wind speed is decelerated. This decelerated region increases in depth with distance from the upwind leading edge of the containers. When this decelerated air reaches the bridge it is greater in height than the height of the bridge to the container top. This decelerated air reduces the magnitude of the accelerated air created by the upwind leading edge.

At a height of z/H=2.5 the CFD models show that the wind speed is increased to 1.04 and there is little difference (within 2 %) between the container ship and the tanker. It may be possible that the PIV may be overestimating the container ship wind speed at this height. In summary the CFD models show that the container ship is affected by the ships bow and the normalised wind speed magnitude above the bridge of the container ship is less than the tanker.

4.5.6 CFD compared with the PIV measurements

The positions of the line of equality and the wind speed maximum from the tanker and deck house block CFD model are compared to the scaling laws (eq. 3.2 and 3.3) derived from the PIV measurements in Figure 4.16. The container ship

model results are not included as it is not clear if the CFD has been able to accurately reproduce the flow pattern over the ship. The upwind leading edge of each model was located at x=z=0 and the maximum and minimum position of the CFD models are indicated as an error bar and a symbol indicates the average height. The average of the CFD tanker and deck house block model results of the position of the line of equality agree very well with the PIV derived scaling law. The position of the maximum wind speed does not agree very well with the CFD at the upwind front edge of the bridge, but agrees well at distances greater than x/H=0.5.

The maximum normalised wind speed from each CFD model is compared to the PIV measurements in Figure 4.17. The maximum and minimum position of the CFD models are indicated as an error bar and a symbol indicates the average maximum normalised wind speed. The CFD simulations of the flow over the scaled wind tunnel geometries are approximately 20 % lower than the PIV measurements. The reason for the discrepancy will be examined in Chapter 5.

4.5.7 Summary

The tanker and deckhouse block geometries agree in the position of the line of equality and in the height of the wind speed maximum and predict a maximum normalised wind speed of 1.11 to 1.14. The flow over the container ship is more complex and there is evidence to suggest that the flow above the bridge was effected by the upwind bow step. The CFD modelling suggests the position of the wind speed maximum above the bridge of the container ship is located at a height of z/H=1.5 and has a maximum normalised wind speed of 1.03 to 1.07.

4.6 Summary

The aim of this chapter was to test the performance of VECTIS in modelling the flow over bluff body merchant ships. A number of VECTIS simulations of the flow over the full-scale tanker showed that:

4a) The effect of different parameters on the CFD model solutions were examined and the following was found. The flow above the bridge was independent of the mesh density for minimum cell sizes of less than 0.038H, the $k \sim \varepsilon$ turbulence closure overestimates the velocity field at the upwind leading edge, and the inlet wind speed profile has the largest influence (4 %) on the wind speed above the bridge.

4b) Apart from at the upwind leading edge the CFD models all accurately reproduced the pattern of the flow distortion seen in the PIV wind tunnel study. The CFD predicted a normalised wind speed maximum of 1.08.

Flow simulations over scaled models of the container ship, tanker and deck house block showed that:

4c) All the CFD models reproduce the pattern of the flow reasonably well.

4d) None of the CFD models agreed with the wind tunnel study when predicting the magnitude of the maximum acceleration. The wind tunnel experiment suggested a maximum acceleration of the flow of about 38 % (at 0.40H aft of the leading edge and at a height of 0.46H), whereas the wind tunnel scale CFD models predicted the maximum value would be between 11 % to 14 %.

4e) The heights of the line of equality and the wind speed maximum for the container ship was higher than the other two ships. This was caused by the flow of air over the bow decelerating the air in front of and above the bridge.

An experiment to determine whether the PIV wind tunnel measurements are overestimating the normalised wind speed in comparison with the CFD models will be detailed in Chapter 5. However, even if it is shown that VECTIS does not predict the wind speed maxima well, the CFD code can still be used to predict if an anemometer is in a region of accelerated or decelerated flow.

5. A COMPARISON OF THE PIV AND CFD MODEL RESULTS WITH *IN SITU* SHIP DATA MEASURED ABOVE THE BRIDGE OF A RESEARCH SHIP

5.1 Introduction

The aim of this section is to determine how realistic the predictions developed in Chapter 3 are when applied to the problem of correcting wind speed data measured from a real ship. Chapter 4 showed that the CFD and PIV models agreed on the pattern of the flow above the bridge of a merchant ship, but differed in the magnitude of the predicted maximum wind speed. This section examines these differences.

In situ wind speed measurements were made during two cruises of the *RRS Charles Darwin*. Although the *RRS Charles Darwin* (Figure 5.1) is not a typical Voluntary Observing Ship of the type examined in this thesis, the ship's structure makes it ideal for studying bluff body flows when the wind is blowing on to either beam. In Chapter 4, the PIV and CFD model wind speeds were normalised by the free stream speed in order to quantify the magnitude of the acceleration/deceleration. Measurements of the free stream flow were not available for the *in situ* data, so an estimate has to be made. Yelland *et al.* [9, 29] suggests that 'detailed' CFD models can be used to correct data from anemometers located in regions of low flow distortion for flows within ±30° of the bow. However, this study concentrates on air flows directly over either beam of the ship (at ±90° of the bow) so it is necessary to check that the foremast anemometer is located in a region of low flow distortion. If the flow distortion at the site is low for beam-on flows, the wind speed data from that anemometer will be corrected for flow distortion, using results obtained from detailed CFD models of the ship, and then used to calculate the free stream profile.

The instrumentation used to measure the *in situ* wind speed data is detailed in Section 5.2. The severity of the air flow distortion at the foremast anemometer is examined in Section 5.3, using CFD models of the ship. Section 5.3 also

describes the method used to determine the vertical profile of the free stream velocity. The normalised *in situ* data are then compared in Section 5.4 to the CFD and PIV results.

The bias in the PIV measurements is examined in Section 5.5 by comparing PIV results to CFD simulations of the air flow through the wind tunnel. Section 5.6 examines the sensitivity of the flow above the bridge to changes in wind speed and relative wind direction.

5.2 *In situ* wind speed measurements

The *RRS Charles Darwin* cruises CD140 and CD141 [86] took place in the Indian Ocean (Figure 5.2) for 58 days between May and July 2002. The ship was equipped with 7 anemometers located on the foremast and above the bridge. The instruments used and their accuracy were: one HS sonic[5] anemometer (< ±1 % for winds below 45 ms^{-1}); one R2 sonic[5] anemometer (<1 % rms); one Windmaster sonic[5] anemometer (1.5 % for winds below 20 ms^{-1}) and four Vector cup[6] anemometers (1 %, ± 0.05 ms^{-1}). The HS, R2 and Windmaster sonics output 3-component wind speed measurements at 20 Hz, 21 Hz and 0.1 Hz respectively. The Vector cup anemometers measure the horizontal wind speed component only and were sampled at 0.1 Hz. The wind directions measured by the sonic anemometers are accurate to within ±2°. This effectively leads to a true wind speed accuracy of within 2 % to 4 % depending upon the relative wind speed. Aligning the anemometers relative to the ship may lead to larger errors and is discussed in [29].

The HS sonic anemometer was located on the foremast platform (Figure 5.3) and its position is illustrated in Figure 5.4. A temporary 6 m mast equipped with the R2 sonic anemometer, four Vector anemometers and the Windmaster sonic anemometer was located above the bridge top (Figure 5.5). The anemometers above the bridge were positioned so as to measure wind speeds in

[5] Developed and calibrated by: Gill instruments Ltd., Lymington, UK.

[6] Developed and calibrated by: Vector instruments, Rhyl. N. Wales, UK.

the accelerated region, the region close to the 'line of equality' and the decelerated region close to the bridge top, for flows over either beam. The position of the mast and the anemometer heights were selected using the scaling laws developed in Chapter 4 and are shown in Figure 5.6. Taking the height of the bridge above the waterline as the step height, H=13 m, the mast was located x/H=0.21 from the starboard side and x/H=0.51 in from the port side. The anemometers were located 5.2 m back from the bridge front in a region of good exposure for flows over either beam. The mast position and heights of the anemometers above the bridge are shown in Figures 5.7 and 5.8 respectively.

During the first leg of the cruise from Australia to the Seychelles the Windmaster sonic was positioned closest to the bridge top ('anemometer E' in Figure 5.8) to acquire all three components of the flow in a region where the flow is severely decelerated. During the port call in the Seychelles on the 29th May 2002 the Windmaster sonic was swapped with the Vector anemometer located at a height of z/H=0.27 ('anemometer C' in Figure 5.8) above the bridge top. This was done in order to accurately measure the wind speed maximum for air flows over the starboard beam.

The 20 Hz output from the HS sonic and the 21 Hz output from the R2 sonic were logged for 54 minutes and 52 minutes respectively (64 sampling periods of 1024 data) every hour. Each sampling period was averaged to produce a mean relative wind speed over a 51 second period. Data from the other anemometers were logged at 0.1 Hz and then averaged over the same 51 second period. The *RRS Charles Darwin* results contained approximately 32 days of wind speed data for relative wind directions within ±90° of the bow. The maximum relative wind speed was 21 ms^{-1} and the mean was 10 ms^{-1}.

Pre- and post-cruise calibrations of the HS sonic, R2 sonic and Windmaster sonic were performed to examine any change in the accuracy of the instrumentation during the cruises. The post-cruise HS and Windmaster calibrations showed there was no change in their calibration during the cruise. The post-cruise R2 sonic calibration suggested a 2 % overestimate of the wind

speed for relative wind directions over either beam. The correction was applied to the wind speed data measured by this instrument.

The HS, R2 and the Windmaster sonic anemometers are very accurate at measuring low wind speeds, but could not be used for all the sites on the temporary mast due to the size and weight of the anemometers. Therefore, Vector anemometers were used at four locations above the bridge. The Vector cup anemometers were purchased especially for the cruise. The manufacturer's calibrations were applied, but no facilities were available to perform a post-cruise calibration of these instruments. The Vector anemometers required a cosine correction to calculate the total wind speed;

$$\text{total wind speed} = \frac{v_x}{\cos(\theta)} \qquad (5.1)$$

were v_x is the measured horizontal wind speed component and θ is the angle of the flow to the vertical at the anemometer site. The angle of the flow, θ, was predicted by CFD models (Table 5.1) at a number of relative wind directions. Interpolation between the CFD predicted θ was used for relative wind directions not modelled. Cosine corrections of up to 4 % were applied to the wind speed data at 10° intervals within relative wind directions of ±90°. The cosine corrections were applied to all vector anemometer wind speed data shown in this section. Further, references to anemometers above the bridge will be described in terms of height and named from top to bottom: R2 sonic and anemometers A to E.

5.3 Determination of a free stream value

An estimate of the undistorted, or free stream flow, is required in order to quantify the biases in the measured wind speed. This section will examine the problem of estimating the free stream velocities for the *in situ* data. Yelland *et al*. [9, 29] showed that very detailed CFD models of the *RRS Charles Darwin* reproduced the wind speed at very well exposed anemometer sites to within about 2 % for flows within 30° of the bow. This section will determine the severity of the airflow distortion at the anemometer sites used during voyages CD140 and

CD141 for flows between ±90°, again using very detailed models of the ship. It will be shown that (a) the HS sonic anemometer is in a region of low flow distortion and (b) that the CFD results are a good estimate of the wind speed. These results give confidence that the CFD estimates of the flow distortion can be used to correct the HS sonic wind speed data. These corrected data are then used to calculate the vertical profile of the free stream wind speed.

Descriptions of the methods used to model the flow over the ships are given in detail in Moat and Yelland [25, 87, 88]. The VECTIS discretisation is detailed in Chapter 4, and will only be summarised here. To create a numerical model of the ship the 1:100 scale general arrangement plans were digitised and then converted into a 3-dimensional geometry using the pre-processor FEMGEN [70] at which point the detailed ship geometry was enclosed in a computational volume or 'wind tunnel'. The dimensions of the computational domain used for each ship were similar, with a 'wind tunnel' length and height of 600 m and 150 m respectively. The width of the domain was chosen to ensure that the blockage of the flow in the tunnel by the ship was minimal [56] and therefore depended on the angle of the ship to the flow. For the *RRS Charles Darwin* model the 'wind tunnel' width was 300 m for the bow-on flow, and 1600 m for a flow directly over the beam (90°). The 'wind tunnel' inlet wind speed profile varied logarithmically with height, z, and is defined by Equation 4.1. An open ocean wind speed of U_{zN}=14 ms^{-1} at a height of z=10 m is applied. The method to define the wind speed profile is described in Section 4.2.3.

The domain floor was allocated a small roughness length of 10^{-4} m which is equivalent to typical open ocean conditions. Up to 600,000 computational cells of varying size were used to solve the flow field. The $k \sim \varepsilon$ turbulence parameterisation was used for all the models. Once the cell sizes were specified and the mesh was generated, the models were run until the solution had converged, i.e. the velocities at various monitoring locations were constant to within 0.1 ms^{-1}. The time taken for a solution to converge varied from two weeks using an SGI Origin 200 workstation to 5 weeks using an SGI Indigo workstation. In order to check that the ship did not create a significant blockage to the flow in

the tunnel, the speed of the flow at points well abeam was compared to the speed of the flow at the inlet and outlet. Since no significant blockage was found, the speed of the free stream flow was determined using a vertical profile of the wind speed at a point well abeam (more than 100 m) of the anemometer position.

The *RRS Charles Darwin* was modelled for a 14 ms^{-1} flow at 7 different relative wind directions: a) 90° off the starboard bow, b) 30° off the starboard bow, c) 15° off the starboard bow, d) bow-on (head to wind), e) 15° off the port bow, f) 30° off the port bow and g) 90° off the port bow. In comparison to previous bluff body merchant ship geometries Figure 5.9 shows that the ship was reproduced in great detail in the CFD model. However it must be noted that smaller structures such as the hand-rails around the foremast platform and the instruments themselves were too small to be resolved in the model.

The CFD predicted absolute wind speed errors at anemometer sites are shown in Table 5.2. The HS sonic anemometer is the best exposed instrument for flows over either beam, and the highest 2 or 3 anemometers above the bridge are also reasonably well exposed (low to moderate flow distortion). The accuracy of the CFD predicted wind speeds at the reasonably well exposed anemometer sites was examined by comparing 'relative differences' between data from pairs of anemometers. The relative difference is calculated by dividing the speed at a particular anemometer site by that at the site of the reference anemometer. The reference anemometer used was the foremast HS sonic since this was best exposed. The *in situ* and CFD model estimates of the 'relative difference' at the R2 sonic anemometer, anemometer A and B sites are shown in Figure 5.10. The error bars indicate the standard deviation of the data and the vertical dashed lines indicate the centre of the wake shed by the foremast extension. Bow-on flow corresponds to 0° and flows over the port and starboard beams correspond to –90° and 90° respectively. The relative wind direction was measured using the HS sonic anemometer and has been corrected for the horizontal deflection of the flow.

The presence of the ship not only causes a vertical displacement of the airflow, but also causes the air to be deflected in the horizontal plane. The horizontal deflection of the airflow at the HS anemometer site was predicted using

the CFD models. The HS relative wind directions shown in Figure 5.10 have been corrected by up to 7°. Only measured wind speeds above 3 ms^{-1} were used in the analysis since below this wind speed the data were limited in number and showed a lot of scatter.

In general the *in situ* and CFD model results in Figure 5.10 agree closely for the R2 sonic, and anemometers A and B (all within 2%) for air flows within ±30° of the bow. The exception to this is within the wake region created by the presence of the upstream foremast extension (located above the foremast platform), the centre of which coincides with the position of the anemometers when the air flow is approximately 10° (when corrected for horizontal deflection) off the port bow. Air flows over the port beam are subject to high rates of change in the relative difference with relative wind direction, but the agreement is still very good. The agreement between the *in situ* data and CFD model for flows over the starboard beam is within 5%, which is reasonably good given the size of the error bars.

The HS anemometer was chosen to calculate the free stream wind speed because; it was the best exposed instrument and it was located on the foremast, well away from the bridge top, i.e. the area under investigation in the next section. CFD corrections of 7.3 % and 3.7 % were applied to the HS *in situ* wind speed data for flows over the port and starboard beams respectively. Logarithmic wind speed profiles at three different wind speeds were calculated (using eq. 4.1) to examine the change in free stream wind speed with height between the HS sonic and the bridge anemometers. Free stream wind speeds profiles calculated using U_z = 5, 10 and 15 ms^{-1} showed an increase in speed of about 2 % (about 0.5% per m) from the HS sonic height at 15.2 m to the R2 sonic at 19.6 m. The free stream wind speed measured from the HS sonic was corrected for the change in height and used to normalise the wind speed measurements made by anemometers above the bridge. These normalised wind speed profiles for air flows over the port and starboard beams are compared with the bluff body CFD and PIV results in the next section.

5.4 Comparison of the *in situ* ship data with the model bluff body results

The PIV and CFD derived scaling laws developed in Chapter 4 agree in defining the positions of the lines of equality and the maximum and the minimum wind speeds, but differ in quantifying the magnitude of the wind speed maximum. In this section *in situ* normalised wind speed profiles measured by anemometers above the bridge on the *RRS Charles Darwin*, for beam-on flows, are compared to the PIV and CFD normalised wind speed profiles for a flow directly over the deck house block. The normalised wind speed is defined as the measured wind speed divided by the free stream wind speed. This comparison will be used to confirm the results of Chapter 4 and determine which of the two models may best describe the magnitude of the wind speed maximum. Only flows directly over either beam of the *RRS Charles Darwin* were considered, as at other relative wind directions the ship was not a good representation of a true bluff body shape. In addition, the presence of upwind obstacles, such as satellite domes, prevented other relative wind directions being studied.

The magnitude of the wind speed maximum is dependent upon the type of ship (Figure 4.17). The flow of air over the *RRS Charles Darwin* beam-on has a greater resemblance to the deck house block than to other model geometries, i.e both *RRS Charles Darwin* beam-on and deck house block are effectively single steps. For this reason the normalised CFD and PIV results of the flow over the deckhouse block were compared to the *in situ* data. Flows over the starboard beam are shown in Figure 5.11 and port beam in Figure 5.12. The height above the bridge, z, was scaled by the step height, H, of the respective model. Likewise, x, the distance downstream of the leading edge was scaled by H. The upwind leading edge of the bridge is defined as x/H=0=z/H. The error bars indicate the standard error of the data. The standard error of the *in situ* data was too small to be displayed in Figure 5.12 and ranged from 0.001 to 0.003, and 0.003 to 0.006 for flows over the starboard and port beams respectively.

The *in situ* wind speed data measured by anemometers on the temporary mast were normalised by free stream measurements calculated from the HS sonic. The *RRS Charles Darwin* step height (H=13 m) was defined as the height of the

bridge top above the waterline for beam on flows. Using this step height the scaled distance of the anemometers from the starboard and port upwind leading edges were x/H=0.21 and x/H=0.51 respectively.

The PIV data were extracted at scaled distances of x/H=0.21 and x/H=0.51 back from the front edge of the deck house block. As described in Chapter 3, the resulting PIV wind speed profiles were normalised by free stream profiles measured in the wind tunnel with no model present, and the vertical height, z, was scaled by the PIV model deck house block height of H=0.422 m.

The CFD wind speed profiles were extracted at x/H=0.21 and x/H=0.51 back from the front edge of a simulation of the flow over the scaled deck house block of height H=0.422 m. The CFD simulation (Figure 5.13) is detailed in Section 4.5 and used a large computational volume (24H high by 44H wide) so that the boundary walls had no blockage effect on the wind speed above the deck house block. These data were normalised by a free stream profile obtained from a second CFD simulation with no deck house block present.

Qualitatively, Figures 5.11 and 5.12 show a very good agreement with regard to the shape of the profiles from both model and *in situ* results. Both *in situ* profiles predict a decelerated region above the bridge top, which varies in depth with distance back from the upwind leading edge. The wind speed increases to a maximum (at z/H=0.28, Figure 5.11) and then decreases with increase in height. The scaling laws (Figure 5.6) do well in predicting that anemometers C, D and E (flow over port beam) and anemometer E (flow over starboard beam) are within the recirculation region.

For the first time this confirms that the models do qualitatively predict the general flow pattern above the bridge of a merchant ship. The magnitude of the wind speed maximum for the *in situ* data is 17 %. The CFD model predictions of the increase in the wind speed magnitude agree very well (within 4 %) with the *in situ* data for flows over both beams. The PIV model results overestimate the wind speed maximum by up to 15 % and 22 % for flows over the starboard and port beams respectively in comparison with the *in situ* measurements.

In summary, the CFD model is in far better agreement with the measured full-scale *in situ* data than the PIV measurements made in the wind tunnel. The next section discusses the possible bias present in the PIV wind speed data.

5.5 Investigation of the PIV bias

As discussed in Chapter 3, the PIV measurements are accurate to within about 5 %. The comparisons of CFD simulations over cubes in Chapter 4 showed that there are possible biases in the CFD simulations of up to 5 %, depending on the turbulence closure scheme used. The use of CFD simulations to correct the HS sonic wind speed data and the possible anemometer calibration errors lead to an estimate of about 5 % for the possible bias in the *in situ* data. These biases cannot account for the observed difference of up to 22 % between the *in situ* data and the PIV results. Consideration was therefore given to the possibilities that the problem may be due to wind tunnel and wall contraction effects.

The CFD simulations of the flow of air over the deck house block, used in Figures 5.11 and 5.12, have only been modelled as a unbounded flow (Figure 5.13), i.e. the walls and roof have no effect on the solution and therefore there is a blockage ratio of virtually zero. Two further CFD simulations of the wind tunnel were performed to examine the flow in the wind tunnel. The boundary conditions of the two models are based on the unbounded flow over the deck house block (Section 4.3.3), i.e the flow at the inlet was a uniform profile of 7 ms^{-1}. The only exception was the turbulence parameters at the inlet which were modified to correspond with typical values experienced in the wind tunnel, i.e. a turbulent intensity of 0.2 % of the mean flow [89]. This resulted in a turbulent kinetic energy, k, and a rate of dissipation of the turbulent kinetic energy, ε, at the inlet of 0.014 m^2s^{-2} and 0.0012 m^2s^{-3} respectively. The inlet conditions of all three models were compared and it became apparent that a slight miscalculation of the cross sectional area of the inlet of the unbounded flow model had led to an underestimate of the Mass Flow Rate (MFR). This reduced the inlet velocity of the simulation by 0.5 ms^{-1}. This is evident in a comparison of the velocity fields between the unbounded flow (Figure 5.13) and the flow through the low speed

section (Figure 5.14). This miscalculation of the MFR has no effect on the unbounded flow normalised profiles as the same MFR was used for the free stream flow simulation with no deck house block present. For both CFD models the size and number of cells in the computational grid above the deckhouse block was the same as that used in the unbounded simulation, i.e. the mesh densities were the same for all three models. In the two wind tunnel simulations the roughness length, z_o, of the deck house block surfaces and the wind tunnel floor, walls and roof were increased to z_0=0.001 m to better represent the flow through the wind tunnel. Both CFD models were repeated without the deck house block present in order to determine the free stream.

The first model was a simulation of the flow through the low speed section of the wind tunnel and included the walls and roof (Figure 5.14). Like the unbounded flow, the length of the wind tunnel has been extended by 2.82 m to remove possible errors caused by the down stream wake of the block recirculating through the outlet.

In the Southampton wind tunnel the cross section contracts downstream of the low speed section and the PIV measurement area is located close to the start of this constriction (Figure 5.15). The effect of the blockage caused by the deck house block and the narrowing of the wind tunnel, was investigated by using the second CFD model to simulate the air flow in an exact reproduction of the wind tunnel (Figure 5.15).

Figures 5.16 and 5.17 show the normalised wind speed profiles from the unbounded flow and the full wind tunnel with the contraction. Profiles from the CFD simulation through just the low speed section are not shown as they are almost identical to the unbounded flow (Figure 5.18). It is clear from the CFD simulations that the blockage effect caused by the narrowing of the wind tunnel and the deck house block is increasing the wind speed maximum at the measurement location by 7 % (at x/H=0.21) and 9 % (at x/H=0.51). The CFD simulations also suggest that the re-circulation region close to the top of the deck house block is being reduced in depth with distance from the front edge in the wind tunnel.

Figure 5.18 show the normalised wind speed profiles from the unbounded flow, low speed section of the wind tunnel and the full wind tunnel with the contraction. A comparison of the CFD models of the unbounded flow and the low speed section of the wind tunnel show no change in the magnitude of the normalised wind speed maximum. Modelling the whole wind tunnel showed an increase in the normalised wind speed of approximately 8 %. It is thought that the combined blockage of the deck house block and the contraction is concentrating the acceleration of the flow towards the centre of the lower part of the tunnel. In other words, the deck house block gives a blockage ratio of 1 % (Section 3.1), which in the absence of the contraction has no big effect since the flow is only accelerated by 1 % across the whole cross section of the tunnel. When the contraction is introduced the 1 % blockage ratio seems to result in a flow that is accelerated by 8 % in the lower part of the tunnel (above the deck house block), and shows 0 % acceleration towards the roof and walls.

The results in Figures 5.16 and 5.17 would indicate that the influence of the wind tunnel contraction downstream of the model would seem to partly explain the relatively high values of the PIV measurements.

5.6 Sensitivity study of the flow above the bridge

The above section has partially explained the reasons for differences between the PIV and CFD results, for flows above a bluff body. This section uses the *in situ* data to examine the sensitivity of the results to changes in wind direction and wind speed.

Normalised *in situ* wind speeds were extracted for relative wind directions of 80° to 90° and 90° to 100°, and are compared to the beam on data (at 85° to 95°) in Figures 5.19 and 5.20. There is very little change (within ±1 % at most) in the profile with a 5° change in relative mean wind direction for flows over the starboard beam (Figure 5.19). This increases to 5 % for flows over the port beam (Figure 5.20). This is a large increase for such a small change in relative wind direction and suggests that wind speed may vary significantly with changes in

relative wind direction. In addition, Table 5.2 shows that there are significant changes (in excess of 10 %) in the wind speed errors at anemometer locations with relative wind direction. This implies that the wind speed profiles at other wind directions may vary significantly with changes in relative wind direction. the presence of upwind obstacles distorting the air flow in the *in situ* data from the *RRS Charles Darwin* prevented other relative wind direction being studied. The 5 % increase in the wind speed maximum for relative wind directions of within ±5° for air flows over the port beam may be caused by either a) small scale obstructions above the bridge or b) a change in the distortion of the flow to the foremast anemometer which was used to calculate the free stream speed, but as it cannot be discounted this change should be borne in mind when applying the results of this thesis to merchant ship data.

It has been assumed that the pattern of the flow is not dependent on wind speed, i.e. the shape of the *in situ* normalised profile above the bridge will not change with variations in wind speed. This is tested by splitting the wind speed data into two groups, comprising data above and below the mean wind speed of 10 ms^{-1} and then comparing wind speed profiles from these two groups to the wind speed profile obtained if using the full range of wind speeds (Figures 5.21 and 5.22).

The variation in wind speed for flows over the starboard beam, Figure 5.21, has very little effect (within 1%) on the normalised wind speed profile above the recirculation region. Similarly, the variation in wind speed has little effect (within 2 %) on the normalised wind speed profiles over the port beam, Figure 5.22. Within the recirculation region there are greater variations of up to 3 % and 6 % for flows over the starboard and port beams respectively. Even though the changes between the normalised wind speed profiles are slightly larger for the anemometers within the recirculation region, it is not unexpected as it is known that the wind speed in this region is severely decelerated and the Vector anemometers are not very accurate at low wind speeds.

These results give confidence that the flow above the recirculation region does not vary significantly with variations in wind speed. It has been observed

that the flow above the bridge may be sensitive to small changes in relative wind direction.

5.7 Summary and discussion

The aim of this Chapter was to test the PIV and CFD scaling laws derived in Chapter 3 and 4, which were used to predict the flow over bluff body merchant ships. This chapter examined if the model results apply to real flows over merchant ships and which of the models predicts the more realistic wind speed maximum. Wind speed data from anemometers located above the bridge of the *RRS Charles Darwin* were used to measure beam-on flows, i.e. a flow over a single step bluff body. These normalised *in situ* wind speed profiles were compared to the results of the PIV and CFD models for the flow over a deck house block (single step bluff body).

The bias in the PIV measurements was investigated by performing CFD models of the actual wind tunnel geometry, i.e. the same physical dimensions were used. CFD models of just the low speed section of the wind tunnel showed no change in the magnitude of the normalised wind speed maximum. Modelling the whole wind tunnel showed an increase in the normalised wind speed of approximately 8 %. It is thought that the combined blockage of the deck house block and the contraction is concentrating the acceleration of the flow towards the centre of the lower part of the tunnel. In other words, the deck house block gives a blockage ratio of 1 %, which in the absence of the constriction has no big effect since the flow is only accelerated by 1 % across the whole cross section of the tunnel. When the constriction is introduced the 1 % blockage ratio seems to result in a flow that is accelerated by 8 % in the lower part of the tunnel (above the deck house block), and shows 0 % acceleration towards the roof and walls.

In summary:

5a) Model results are generally confirmed by *in situ* data, in that all agree on the pattern of the flow. The use of *in situ* data has shown that the

CFD model results for flows over bluff bodies can be applied both qualitatively and quantitatively to the real flow above the bridge of real ships.

5b) CFD modelling is accurate in predicting the magnitude of the maximum.

5c) Compared with the *in situ* data the PIV measurements overestimate the magnitude of the normalised wind speed maximum by approximately 20 %, i.e. an increase in the normalised wind speed of 0.2.

5d) The down stream contraction in the tunnel may exaggerate the effect of any blockage by concentrating the resulting acceleration of the flow to the centre of the lower part of the wind tunnel.

5e) *In situ* data shows that the pattern of the flow may be sensitive to relative wind directions, but not to wind speed.

6. OVERALL DISCUSSION

6.1 General

The airflow distortion at anemometer sites on merchant ships was previously unknown. This thesis compares the mean airflow above the bridge of a ship obtained via three standard techniques: wind tunnel measurements, CFD modelling and full-scale wind speed measurements from anemometers located on a ship. The wind tunnel testing and CFD modelling was carried out using wind tunnel scale geometries of simple bluff body representations of merchant ships. The wind tunnel studies and CFD modelling were used to derive scaling rules that predict the extent of the accelerated and decelerated regions of air flow above the bridge of the ships.

During the wind tunnel tests the mean airflow over the generic tanker, container ship and the deck house block were measured using a PIV system. Wind speed measurements in an area of 0.36 m by 0.29 m were made above the bridge of each ship geometry, which corresponded to 31 (z, vertical) and 39 (x, streamwise) velocity measurements. The wind speed measurements were normalised using a free stream wind speed measured with no ship geomerty present. The accuracy of the wind speed measurements is considered to be within 4 %, with the variation in the nominal wind speed being the main contribution to this accuracy. Wind tunnel speed variations caused by density variations, caused in turn by temperature variations were observed. To minimise possible wind speed variations in the wind tunnel, the wind tunnel was run without keeping the dynamic pressure constant, i.e. the speed of the fan was kept constant through out the experiment. Even so, variations in wind speed of 0.2 ms^{-1} (3 %) within a period of 40 minutes were present. The maximum time difference between the PIV measurements made with and without the geometry present is also 40 minutes. Therefore it is possible that errors of up to 3 % could exist in the normalised wind speed data. The wind speed variations could have be minimised by using the high speed section of the wind tunnel. This would mean a significant reduction in the size of the ship geometry and could introduce scaling

problems which may mean that the simulation would not produce the full-scale flow.

A large number of CFD simulations were performed to determine the suitability of the technique for estimating the airflow distortion over merchant ships and the wind speed changes that could be observed. The technique has been proved to be robust and is thought to be reliable and should be used to estimate the flow distortion above merchant ships. CFD agrees well with the PIV measurements in the general flow pattern, but disagrees with the PIV by within 10 % for the magnitude of the wind speed maximum. For a first ever study of this problem this difference is thought to be acceptable and will be applied to wind speed data from merchant ships. So far only the PIV and CFD predictions of the flow over the deck house block have been compared to *in situ* wind speed measurements from a ship. Section 7.5 contains details of future work to instrument a container ship and compare the results to the CFD normalised wind speed predictions in Figure 4.14.

In summary, the airflow above the bridge of a merchant ship scales with the height of the bridge to the deck. Simple equations can be used to describe the general pattern of the flow and using the anemometer position the sign of the bias in the wind speed measurements can be calculated. The magnitude of the wind speed maximum is slightly more complex, as the flow above the container ship bridge is affected by the air flow over the upwind bow and should be treated separately. In general, using CFD the wind speed above the bridge of a tanker/bulk carrier can be increased by up to 11 % above the equivalent free stream wind speed. Large decelerations of up to 90 % can exist for anemometers placed close to the bridge top.

6.2 The pattern of the airflow above the bridge

The mean airflow over the bluff body merchant ships is defined by flow separation at the upwind leading edge, with a decelerated region close to the bridge top which increases in depth with distance from the leading edge. Above

the decelerated region there is a line of equality where the wind speed is equal to the free stream value. Above the line of equality the wind speed increases to a maximum and then reduces to the free stream wind speed with height. In all cases there was no evidence of the flow reattaching to the bridge top.

It was found that the general pattern of the wind speed above the bridge scales with the height of the bridge above the deck, H. The PIV wind tunnel measurements agreed well with the CFD models in predicting the position of the line of equality and the maximum wind speed, and both techniques agreed well with the pattern of the flow measured above the bridge of the research ship. For airflows over generic merchant ships simple equations have been developed to describe the positions of the line of equality and the maximum and minimum wind speeds, from the anemometer position relative to the upwind edge of the bridge and the step height, H. Therefore, as long as the anemometer position and the step height are known, the sign of the bias in the anemometer wind speeds can be predicted. Airflows over the deck house at different relative wind directions were measured in the wind tunnel but airflows over the scaled generic merchant ships at different relative wind directions were not measured and no CFD models were performed.

6.3 The magnitude of the wind speed maximum above the bridge

Figures 6.1 and 6.2 show all the results for distances of x/H=0.21 and x/H=0.51 from the upwind leading edge. These include the *in situ* wind speed measurements made from the research ship *RRS Charles Darwin*, the PIV measurements corrected for the effects of the wind tunnel contraction and the CFD predicted wind speed. Unfortunately, there were no measurements made at x/H=0.51 during the PIV 2000 experiment. There is a reasonable agreement (to within 10 %) between the sets of results. Some of the disagreement could be due to small variations in free stream wind speed caused by temperature changes (up to 3 %). Figures 6.1 and 6.2 only show the flow above the deck house block, as this was more representative of the beam on flows measured over the research ship. The magnitude of the wind speed maxima above the bridge of the tanker

and container ship are between 1.07 and 1.14, Figure 4.14. The thermal probe measurements above the bridge of the tanker predicted wind speeds of about 1.20 (Figure 3.9), which agreed well with PIV measurements corrected for the effect of the tunnel contraction. The thermal probe anemometer is robust, was normalised by a free stream profile measured at the same temperature (to within 1 °C), and is considered to give good accuracy.

In comparison with other known measurements methods the Dantec PIV system has shown spurious differences in wind speed of up to 10 % [89] in measurements made within a recirculation bubble. This discrepancy was not located in the region of accelerated flow, but highlights that wind tunnel measurements using PIV could be prone to measurement errors. These errors could be due to the shape of the boundary layer profile and changes in velocity in the wind tunnel, and the set up of the PIV system. The CFD has been validated against independent wind tunnel studies (Section 4.3) and it is considered that the CFD predicted wind speeds are of adequate standard to correct the wind speed measurements made from research ships. The exception may be around the front edge of the bridge were the CFD predictions suffer from possible numerical error caused by the overestimation of the turbulent kinetic energy, k. In this case the PIV results could be preferable to calculate the airflow distortion for anemometers in this region.

6.4 Applications of the developed techniques

At present, information on the heights of the anemometers above the bridge of merchant ships is limited. The Voluntary Observing Ships' Special Observing Project – North Atlantic (VSOP-NA) selected a subset of 45 VOS operating in the North Atlantic and produced detailed descriptions of the ship type and instrumentation used [3]. The majority of the ships were container ships with anemometers located between 6 m to 10 m above the bridge. Using eq. 2.2 to predict the step height from the LOA, z/H varies between 0.7 to 1.5 and shows that for container ships the majority of anemometers are located outside the

recirculation region and wind speed measurements will have a positive bias of between 3 % to 11 % (Figure 4.14).

Based on the work in this thesis recommendations are made for the best location for placing anemometers on merchant ships. Anemometers should be located as far forwards and as high as possible; ideally, directly above the front edge of the bridge. If an anemometer cannot be located at the front edge of the bridge it should at least be located above a height of z/H=0.3 to measure wind speeds outside the recirculation region. Anemometers should not be placed close to the line of equality as high velocity gradients are present in this region. Canadian coast guard vessels have already made use of these findings [90].

If the height of the anemometer above the bridge (z), the distance of the anemometer from the upwind leading edge (x), and the height of the bridge to the deck (H) is known, then the airflow distortion at a given anemometer position can be estimated from Figure 4.14a) to 4.14d), by finding the closest scaled distance x/H, and reading off the normalised wind speed for the scaled height of the anemometer from the appropriate figure.

A potential subset of 200 Voluntary Observing Ships (VOS) are currently being recruited and meteorological data from these ships will be used in the Voluntary Observing Ship Climate program (VOSClim) project [52]. The scaling laws developed in this Thesis will be used to estimate the bias in the wind speed measurements made by fixed anemometers on tankers and container ships. As pointed out in Section 2, bulk carriers are similar in shape to tankers and will also be included. In light of this study the WMO has already changed its reporting methods to include the necessary information to apply the results of this thesis [52]. The COADS will include additional information concerning the ship type, step type, vessel dimensions, and the position of the anemometer relative to the ship. It will take time for the WMO to implement these changes. In the meantime, the height of the bridge to the deck, H, can either be calculated from: 1) the length overall using eq. 2.1 (tanker) or eq. 2.3 and 2.4 (container ship); or 2) merging ship dimensions from Lloyds of London data base on to the VOSClim data by call sign or International Maritime Organisation (IMO) identification

number. The ship type is included in the Lloyds data and the anemometer height is included in the WMO47 metadata. The application of the method to correct the wind speed data is shown as a flow diagram in Figure 6.3.

7. CONCLUSIONS AND RECOMMENDATIONS

7.1 General

7.1.1 The current investigations using experimental and numerical techniques have contributed to a better understanding of the flow over the bridge of merchant ships. The flow above the bridge of a tanker type shape and container ship scales with the bridge to deck height, H. This is an important result as H can be estimated from the ship length and the pattern of the flow can be calculated for any length of ship. Provided the anemometer position is known, the wind speed measurement above the bridge can be corrected for the effects of airflow distortion.

7.1.2 Wind tunnel, CFD and full-scale *in situ* wind speed measurements from a ship all show good agreement on the pattern of the flow above the bridge. There is a decelerated region of air close to the bridge top where weak recirculation of the flow is likely, with a line of equality (measured wind speed = free stream wind speed) above it. Above the line of equality the wind speed increases to a maximum and then decreases with increasing height to a free stream value. The height of the free stream value varies depending on whether the flow is over a tanker or container ship.

7.1.3 The current investigations have demonstrated that wind speed measurements made from anemometers above the bridge of a merchant ship can be biased high by up to 15 ±5 %, or low by up to 100 %. This is significant, as a 15 % increase in wind speed caused by airflow distortion would cause a 42 % increase in the estimated wind stress between the ocean and the atmosphere. The magnitude of the wind speed above the container ship bridge was affected by the upwind bow step and should be considered separately to the magnitude of the wind speed above the tanker. Validation of the CFD results was successful and, in both cases, it is recommended that the CFD modelling should be used to predict the magnitude of the wind speed at the anemometer locations.

7.2 Wind tunnel investigation

7.2.1 The smoke tests demonstrated that the flow over the bridge of a merchant ship was similar to the flow over a cube. On the front face of the bridge there was evidence of a standing vortex with a stagnation point above. The flow separated at the upwind leading edge of the bridge. No reattachment of the flow to the bridge top was observed.

7.2.2 Wind tunnel tests using two different measurement techniques have provided extensive measurements over the bridge of a tanker and container ship. Simple equations describing the positions of the line of equality:

$$\frac{z}{H} = 0.45\left(\frac{x}{H}\right)^{0.55}$$

and the positions of the maximum wind speed

$$\frac{z}{H} = 0.62\left(\frac{x}{H}\right)^{0.50}$$

and minimum wind speed

$$\frac{z}{H} = 0.31\left(\frac{x}{H}\right)^{0.71}$$

were developed. Comparative studies with CFD results have supported these findings in predicting the general flow pattern above the bridge of the tanker and deck house block.

7.2.3 When corrected for the wind tunnel contraction the PIV measured magnitude of the maximum wind speed for a tanker is approximately 1.20 to 1.25 depending upon distance from the upwind leading edge. The wind speed maximum for the container ship is 10 % less than the tanker geometry.

7.2.4 Close to the line of equality the normalised wind speed varies between 0.2 to 1.1. Such a large gradient suggests that positions along the line of equality are not the ideal position to locate an anemometer.

7.2.5 The thermal probe study showed the presence of a wall jet close to the tunnel floor which varied in magnitude with temperature and position in the tunnel. Therefore, it is recommended that the scaled ship geometry be raised above the wall jet.

7.2.6 Overall, the wind tunnel investigation has demonstrated that if absolute changes from the free stream wind speed are required, then the free stream or normalised wind speed must be measured after each measurement made above the ship. This is necessary to avoid changes in the free stream wind speed due to temperature variations.

7.3 CFD Investigation

7.3.1 Early CFD investigations determined that the CFD code VECTIS is a valid research tool to investigate the flow over bluff bodies. Comparisons with independent wind tunnel data for flows over cubes supported these findings.

7.3.2 The flow above the bridge of the tanker was independent of the mesh density for minimum cell sizes of less than 0.038H. The $k \sim \varepsilon$ turbulence closure overestimates the velocity field at the upwind leading edge, and the inlet wind speed profile has the largest influence (4 %) on the wind speed above the bridge.

7.3.3 Apart from the container ship, the CFD models all accurately reproduced the pattern of the flow distortion seen in the PIV wind tunnel study. The CFD investigation into the airflow in the wind tunnel showed that the wind speed at the measurement location was accelerated by up to 9 % by the downstream wind tunnel contraction. Applying this correction the

magnitude PIV measurements agreed to within 10 % of the CFD measurements.

7.3.6 Overall, the CFD investigations have demonstrated that the technique can be suitably employed for the investigation of the flow over merchant ships.

7.4 *In situ* wind speed measurements from the *RRS Charles Darwin*

7.4.1 The *in situ* data confirmed that the CFD and PIV results predicted the pattern of the flow well. For flow over the deck house block the CFD results and corrected PIV measurements predicted a maximum normalised wind speed of up to 1.14 and 1.23 respectively. The CFD results agreed to within 3 % of the *in situ* wind speed measurement of 1.17, confirming the suitability of CFD for use in this study of airflows over merchant ships.

7.4.2 Analysis of the *in situ* wind speed data showed that the pattern of the flow may be sensitive to the relative wind direction, but not to wind speed.

7.5 Achievement of objectives

7.5.1 It is considered that the objectives of the investigation have been achieved. The numerical and experimental investigations have provided an improved understanding of the airflow distortion about the bridge of merchant ships.

7.5.2 It is well known that airflow distortion could effect the wind speed measurements made by merchant ships, but no knowledge of the sign and magnitude of the distortion was previously known. The current investigation has, for the first time, provided a method to quantify the flow distortion at anemometer sites on merchant ships.

7.6 Recommendations for future work

As a result of the research programme using experimental, CFD and *in situ* wind speed measurements. The following recommendations are put forward:

7.6.1 Full-scale *in situ* wind speed measurements from anemometers on merchant ships should be made to further evaluate the results of this thesis. A contract between the Woods Hole Oceanographic Institution and Southampton Oceanography Centre has been accepted to fund the instrumentation of a container ship with a number of anemometers.

7.6.2 The loading of container ships is generally not even and gaps are left between the containers. The effect of the gaps on the airflow travelling across the container top and ultimately any change in flow pattern above the bridge is currently unknown. A CFD analysis of the effect of the container ship loading on the wind speed measurements above the bridge should be undertaken.

7.6.3 Further work on the effect of different relative wind directions on the airflow properties over the hull and superstructure should be undertaken.

References

[1] Slutz, J. D., S. J. Lubker, S. D. Woodruff, R. L. Jenne, and M. Steurer, 1985: A Comprehensive Ocean-Atmosphere Data Set (COADS). Co-operative Institute for Research in Environmental Sciences, Boulder, CO, 262 pp.

[2] Woodruff, S. D. , R. J. Slutz, R. L. Jenne, and P. M. Steurer, 1987: A Comprehensive Ocean-Atmosphere Data Set (COADS). *Bulletin of the American Meteorological Society*, **68**, 1239-1250.

[3] Kent, E. C., and P. K. Taylor, 1991: Ships observing marine climate: A catalogue of the voluntary observing ships participating in the VOSP-NA. World Meteorological Organisation, Marine Meteorology and Related Oceanographic Activities Report No. 25, 123 pp.

[4] Kent, E. C., P. K. Taylor, B. S. Truscott and J. A. Hopkins, 1991: The accuracy of ship's meteorological observations – Results of the VOSP-NA. World Meteorological Organisation, Marine Meteorology and Related Oceanographic Activities Report No. 26, 86 pp.

[5] Kent, E. C., P. K. Taylor, B. S. Truscott and J. A. Hopkins, 1993: The accuracy of voluntary observing ships meteorological observations – results of the VOSP-NA. *Journal of Atmospheric & Oceanic Technology*, **10**(4), 591 - 608.

[6] Kent, E. C., R. J. Tiddy and P. K. Taylor, 1993: Correction of marine air temperature observations for solar radiation effects. *Journal of Atmospheric & Oceanic Technology*, **10**(6), 900 –906.

[7] Dobson, F. W., 1981: Review of reference height for and averaging time of surface wind measurements at sea. World Meteorological Organisation, Marine Meteorology and Related Oceanographic Activities Report No. 3, 64 pp.

[Available from World Meteorological organization, Case Postale 5, CH-1211 Geneva 20, Switzerland.]

[8] Smith, S. D., 1980: Wind stress and heat flux over the Ocean in gale force winds. *Journal of Physical Oceanography*, **10**, 709-726.

[9] Yelland, M. J., B. I. Moat, P. K. Taylor, R. W. Pascal, J. Hutchings, and V. C. Cornell, 1998: Wind stress measurements from the open ocean corrected for airflow distortion by the ship. *Journal of Physical Oceanography*, **28**(7), 1511-1526.

[10] Ching, J. K. S., 1976: Ships influence on wind measurements determined from BOMEX mast and boom data. *Journal of Applied Meteorology*, **15**, 102-106.

[11] Kidwell, K. B., and W. R. Seguin, 1978: Comparison of mast and boom wind speed and direction measurements on US GATE B-Scale ships, NOAA Technical Report, EDS 28, CEDDA, Washington D.C., USA.

[12] Mollo-Cristensen, E., 1979: Upwind distortion due to probe support in boundary-layer observations. *Journal of Applied Meteorology*, 18, 367-370.

[13] Romanov, Y. A., I. B. Fedorova, M. S. Chervyakov and G. I. Shapiro, 1983: An improvement in the accuracy of shipboard measurements of wind speed and direction based on aerodynamic tests of a ship model. *Oceanology*, **23**(2), 267-270.

[14] Surry, D., R. T. Edey and I. S. Murley, 1989: Speed and direction corrections factors for ship borne anemometers. Engineering Science Research Report BLWT-SS9-89, University of Western Ontario, London, ON, Canada, 83 pp. [Available from University of Western Ontario, London, ON N6A 5B9, Canada]

[15] Thiebaux, M. L., 1990: Wind tunnel experiments to determine correction functions for shipborne anemometers. Canadian Contractor Report of Hydrography and Ocean Sciences 36, Bedford Institute of Oceanography, Dartmouth, NS, Canada, 57 pp. [Available from Bedford Institute of Oceanography, Dartmouth, NS B2Y 4A2, Canada.]

[16] Blanc, T. V., 1986: Superstructure flow distortion corrections for wind speed and direction measurements made from Tarwa class (LHA1-LHA5) ships. NL Report 9005, Naval Research Laboratory, Washington D. C., 20 pp.

[17] Blanc, T. V., 1987: Superstructure flow distortion corrections for wind speed and direction measurements made from Virginia class (CGN38-CGN41) ships. NL Report 9026, Naval Research Laboratory, Washington D. C., 24 pp.

[18] Berlekom, van W. B., 1981: Wind forces on modern ship forms – effects on performance, *Trans. Of the North East Institute of Engineers and ship Builders*, **97**(4), 123 – 132.

[19] Isherwood, R. M., 1972: Wind resistance of merchant ships. *Trans. of the Royal Institution of Naval Architects*. **115**, 327- 338.

[20] Longo, J. and F. Stern, 1996: Technical note: Evaluation of surface-ship resistance and propulsion model-scale database for CFD validation. *Journal of Ship Research*, **40**(2), 112-116.

[21] Kahma, K. K., and M. Leppäranta, 1981: On errors in wind speed observations on R/V Aranda, *Geophysica*, **17**(1-2), 155-165.

[22] Dupuis, H, 1994: Personal communication. University of Bordeaux, France.

[23] Moat, B. I. and M. J. Yelland, 1996: Airflow over *Le Suroit* using the Computational Fluid Dynamics package VECTIS. SOC Internal Document 3, Southampton Oceanography Centre, United Kingdom, 24 pp.

[24] Moat, B. I. and M. J. Yelland, 1996: Airflow over the *RRS Discovery*: variation of velocity errors with wind speed. SOC Internal Document 4, Southampton Oceanography Centre, United Kingdom, 26 pp.

[25] Moat, B. I. and M. J. Yelland, 1996: Airflow over the *RRS Charles Darwin*: the disturbance of the flow at the anemometer sites used during cruises CD43 and CD98. SOC Internal Document 5, Southampton Oceanography Centre, United Kingdom, 41 pp.

[26] Moat, B. I. and M. J. Yelland, 1997: Airflow distortion at anemometer sites on the *OWS Cumulus*, Southampton Oceanography Centre, United Kingdom. 22 pp. [Available from Southampton Oceanography Centre, Empress Dock, Southampton SO14 3ZH, United Kingdom].

[27] Moat, B. I. and M. J. Yelland, 1998: Airflow distortion at anemometer sites on the *RV Knorr*. Southampton Oceanography Centre, United Kingdom. 29 pp. [Available from Southampton Oceanography Centre, Empress Dock, Southampton SO14 3ZH, United Kingdom].

[28] Moat, B. I. and M. J. Yelland, 2001: Airflow over the *RRS Discovery*: the variation of velocity errors with relative wind direction for anemometers mounted on VIVALDI cruise D223 and OMEGA cruise D224. SOC Internal Document 71, Southampton Oceanography Centre, United Kingdom. 107 pp.

[29] Yelland, M. J., B. I. Moat, R. W. Pascal and D. I. Berry, 2002: CFD model estimates of the airflow over research ships and the impact on momentum flux measurements. *Journal of Atmospheric and Oceanic Technology,* **19**(10*)*, 1477-1499.

[30] Tai, T. C. and D. Carico, 1995: Simulation of DD-963 ship airwale by Navier-stokes method. *Journal of Aircraft*. **32**(6), 1399-1401.

[31] Tai, T. C., 1995: Simulation of LPD ship airwake by Navier-stokes method. *6th Asian Congress on Fluid Mechanics*, Singapore.

[32] Cheney, B. T. and S. J. Zan, 1999: CFD code validation data and flow topology for the technical co-operation program AER-TP2 simple frigate shape. National Research Council Canada, Institute for Aerospace Research, Canada, *Report No. LTR-A-035*, 32pp.

[33] Moctar, O. E and V. Bertram, 2002: Computation of viscous flow around fast ship superstructures. 24th Symposium on Naval Hydrodynamics, Fukuoka, Japan. 68-77.

[34] Aage, C, S. Hvid, P. H. hughes and M. L-Anderson, 1997: Wind loads on ships and offshore structures estimated by CFD. 8th International Conference on the Behaviour of Offshore Structures BOSS'97. Delft. 237-251pp.

[35] Jin, E, J. Yoon, and Y. Kim, 2001: A CFD based parametric study of the smoke behaviour of a typical merchant ship. Practical design of ships and other floating structures. Y-S Wu, W-C Cui, and G-J Zhou (Ed.), Elsevier Science Ltd. 459-465.

[36] Moses, H. and H. G. Daubek, 1960: Errors in wind measurements associated with tower-mounted anemometers. *Bulletin American Meteorological Society*. **42**(3), 190-194.

[37] Gill, G. C., L. E. Olsson, J. S. Sela and M. Suda, 1967: Accuracy of wind measurements on towers and stacks. *Bulletin American Meteorological Society*, **48**, 665-674.

[38] Cremak, J. E., 1968: Tower shadow effect. *Journal of Geophysical Research*. **73**(6), 1869-1876.

[39] Dabberdt, W. F., 1968: Tower induced errors in wind profile measurements. *Journal of Applied Meteorology*. **7**, 359-366.

[40] Dabberdt, W. F., 1968: Wind disturbance by a vertical cylinder in the atmospheric boundary layer. *Journal of Applied Meteorology*, **7**, 367-371.

[41] Izumi, Y. and M. L. Barad, 1970: Wind speeds as measured by cup and sonic anemometers and influenced by tower structure. *Journal of Applied Meteorology*, **9**, 851-856.

[42] Camp, D. W. and J. W. Kaufman, 1970: Comparison of tower influences on wind velocity for NASA's 150-meter meteorological tower and a wind tunnel model of the tower, *Journal of Geophysical Research*, **75**, 1117-1121.

[43] Wucknitz, J., 1977: Disturbance of wind profile measurements by a slim mast, *Boundary Layer Meteorology*, **11**, 155-169.

[44] Wucknitz, J., 1980: Flow distortion by supporting structures. Air sea interaction: Instruments and Methods, F. Dobson, L. Hasse and R Davis (Ed.), Plenum Press, 605-626.

[45] Kondo, J. and G. Naito, 1972: Disturbed wind fields around the obsticle in sheared flow near the ground surface. *Journal of the Meteorological Society of Japan*. **50**(4), 345-354.

[46] Thornthwaite, C. W., W. J. Superior and R. T. Field, 1965: Disturbance of airflow around Argus Island tower near Bermuda, *Journal of Geophyscial Research*, **70**(24), 6047-6052.

[47] Davies, M. E. and B. L. Miller, 1982: Wind effects on offshore platforms – A summary of wind tunnel studies. Report number NMI R140, National Maritime Institute, England.

[48] Chen, Q, Z. Gu, T. Sun and S. Song, 1995: Wind environment over the helideck of an offshore platform. *Journal of Wind Engineering and Industrial Aerodynamics*, **54/55**, 621-631.

[49] RINA Ltd., 1990 - 1993: Significant ships. The Royal Institute of Naval Architects, London, United Kingdom. [available from RINA, 10 upper Belgrave street, London, SW1X 8BQ, United Kingdom.]

[50] Kent, E. C., 2002: Personal communication, Southampton Oceanography Centre, Southampton. UK.

[51] WMO47, 1992: International list of Selected, Supplementary and Auxiliary ships. WMO/OMM No. 47, World Meteorological Organisation, Geneva, Switzerland.

[52] Kent E. C. and P. K. Taylor, 2002: Line Selection, VOSCLIM-III/DOC 2.3, Prepared for the Joint WMO/IOC Technical Commision for Oceanography and Marine Meteorology (JCOMM), VOS Climate Project third meeting, Southampton Oceanography Centre, UK.

[53] ISL, 1997: Shipping statistics yearbook, Institute of Shipping Economics and Logistics, (ISL), Universitätsallee GW1, Bremen, Germany, 473 pp.

[54] Davies, P. O. A. L., 1961: The new 7×5 Ft. and 15×12 Ft low speed wind tunnel at the University of Southampton. A.S.S.U Report Number No. 202. University of Southampton, UK.

[55] Barlow, J. B., W. H. Rae and A. Pope, 1999: Low speed wind tunnel testing (3rd edition), John Wiley and Sons, USA. 713 pp.

[56] Castro, I. P., and A. G. Robins, 1977: The flow around a surface-mounted cube in uniform and turbulent streams, *Journal of Fluid Mechanics*, **79**(2), 307-335.

[57] Romanov, Y. A., I. B. Fedorova, M. S. Chervyakov and G. I. Shapiro, 1983: An improvement in the accuracy of shipboard measurements of wind speed and direction based on aerodynamic tests of a ship model. *Oceanology*, **23**(2), 267-270.

[58] Molland, A. F. and T-E, Barbeau, 2002: An investigation into the aerodynamic drag on the superstructure of fast catamarans. *International Journal of Maritime Engineering*, Royal Institution of Naval Architects, London.

[59] Dantec, 1998 : Flowmap Particle Image Velocimetry Instrumentation. Dantec Measurement Technology A/S, Tonsbakken 18, DK-2740 Skovlunde, Denmark. [Available from Dantec Dynamics Ltd. Bristol. UK.]

[60] Raffel, M., C. Willert and J. Kompenhans, 1998: Particle Image Velocimetry. A practical guide. Springer –Verlag, Germany, 253 pp.

[61] Hunt, J. C. R., C. J. Abell, J. A. Peterka and H. Woo, 1978: Kinematical studies of the flows around free or surface-mounted obstacles; applying topology to flow visualisation. *Journal of Fluid Mechanics*. **86**, 179 – 200.

[62] Muakami, S, A. Mochida and Y. Hayashi, 1993: Comparison of various turbulence models applied to a bluff body. *Journal of Wind Engineering and Industrial Aerodynamics*, **46 & 47**, 21-36.

[63] Synergy Software, 2000: KaleidaGraph, Reading, PA, USA. 288pp. [available from GeoMEM Consultants, 1 High Street, Blairgowrie, Perthshire. UK]

[64] Martinuzzi, R. and C. Tropea, 1993: The flow around surface-mounted, prismatic obstacles placed in a fully developed channel flow, *Journal of Fluids Engineering*, **115**, 85-92pp.

[65] Minson, A. J., C. J. Wood, and R. E. Belcher, 1995: Experimental velocity measurements for CFD validation, *Journal of Wind Engineering and Industrial Aerodynamics*, **58**, 205-215pp.

[66] Cowen, I. R., I. P. Castro, A. G. Robins, 1997: Numerical considerations for simulations of flow and dispersion around buildings. *Journal of Wind Engineering and Industrial Aerodynamics*, **67&68**, 525-545.

[67] Ricardo, 2001: VECTIS Computational Fluid Dynamics (Release 3.5) users guide, Ricardo Consulting Engineers Ltd., Shoreham-by-Sea, United Kingdom, 262 pp. [Available from Ricrado Consulting Engineers Ltd. Bridge Works, Shoreham-by-Sea, West Sussex, BN43 5FG, United Kingdom].

[68] Versteeg, H. K., and W. Malalasekera, 1999: An introduction to Computational Fluid Dynamics. The finite Volume method. Longman, UK. 257pp.

[69] Carrol, B, 2002: Personal communication. Ricardo consulting Engineers, Shoreham-by-sea, U.K.

[70] Femsys, 1999: FEMGV User manu*al*. Femsys Ltd. Leicester, United Kingdom. 598 pp. [Available from Femsys Ltd. 158 Upper New walk, Leicester. LE1 7QA, United Kingdom]

[71] Stull, R. B., 1988: An introduction to boundary layer meteorology. Kluwer Academic, Netherlands. 666 pp.

[72] Launder, B. E., and D. B. Spalding, 1974: The numerical computation of turbulent flows, *Computer Methods in Applied Mechanics and Engineering*, **3**, 269 - 289pp.

[73] Yakhot, V., S. A. Orszag, S. Thangam, T. B. Gatski, and G. Speziale, 1992: Development of turbulence models for shear flows by a double expansion technique, *Physics of Fluids*, **A4**(7), 1510-1520.

[74] Ricardo, 2001: VECTIS Computational Fluid Dynamics (Release 3.5) Theory manual, Ricardo Consulting Engineers Ltd., Shoreham-by-Sea, United Kingdom, 77 pp. [Available from Ricrado Consulting Engineers Ltd. Bridge Works, Shoreham-by-Sea, West Sussex, BN43 5FG, United Kingdom].

[75] Murakami, S, 1993: Comparison of various turbulence models applied to a bluff body, *Journal of Wind Engineering and Industrial Aerodynamics*, **46 & 47**, 21-36 pp.

[76] Rodi, W., 1997: Comparison of LES and RANS calculations of the flow around bluff bodies, *Journal of Wind Engineering and Industrial Aerodynamics*, **69-71**, 55-75pp.

[77] Murakami, S., A. Mochida and Y. Hayashi, 1990: Examining the $k \sim \varepsilon$ model by means of a wind tunnel test and large-eddy simulation of the turbulence structure around a cube, *Journal of Wind Engineering and Industrial Aerodynamics*, **35**, 87-100 pp.

[78] Lun, Y. F., A. Mochinda, S. Murakami, H. Yoshino and T. Shirasawa, 2003: Numerical simulations of flow over topographic features by revised $k \sim \varepsilon$ models. *Journal of Wind Engineering and Industrial Aerodynamics*, **91**, 231-245 pp.

[79] Murakmi, S. and A. Mochida, 1989: Three-dimensional numerical simulation of turbulent flow around buildings using the $k \sim \varepsilon$ Turbulence model, *Building and Environment*, **24**(1) 51-64 pp.

[80] Eason, G., 2000: Improved Turbulence models for Computational Wind Engineering. PhD. Thesis, University of Nottingham, Nottingham, United Kingdom. 219pp.

[81] Zhu, J., and W. Rodi, 1991: A low dispersion and bounded convection scheme, *Journal of Computer Methods in Applied Mechanics and Engineering*, **92,** 87-96.

[82] B. P Leonard, 1979: A stable and accurate convective modelling procedure based on quadratic interpolation, *Computing Methods in Applied Mechanics and Engineering*, **19**, 59-98.

[83] Spalding, D. B., 1972: A novel finite-difference formulation for differential expressions involving both first and second order derivatives, *International Journal of Numerical Methods and Engineering*, **4**, 551-559pp.

[84] D. C. Wilcox, 2000: Turbulence modeling for CFD. Second edition. DCW Industries Inc. California, USA. 540pp.

[85] Castro, I, 2002: Personal communication, Southampton University, UK.

[86] New, A., and Co-authors, 2003: *RRS Charles Darwin* Cruise 141, 1st June – 11th July 2002. *SOC Cruise Report No. 41*. Southampton Oceanography Centre, Southampton, UK.

[87] Moat, B. I., and M. J. Yelland, 1996: Airflow 15° off the port bow of the *RRS Charles Darwin*: The disturbance of the flow at the anemometer sites for cruises CD98 and CD43. Southampton Oceanography Centre, UK. *Unpublished report*, 41 pp.

[88] Moat, B. I., and M. J. Yelland, 1996: Air flow 30 degrees off the port bow of the *RRS Charles Darwin*: the disturbance of the flow at anemometer sites for cruises CD98 and CD43, Southampton Oceanography Centre, Southampton, UK. *unpublished report*, 40 pp.

[89] I. Castro, 2003: Personal communication, Southampton University, UK.

[90] R. Fordice, 2001: Personal communication. Marine data Unit, Meteorological Service of Canada.

[91] Speziale, C. G. and S. Thangam, 1992: Analysis of an RNG based turbulence model for separated flows. *International Journal of Engineering Science*, **30** (10), 1379-1388.

APPENDIX A

A MATHEMATICS MODELS

A.1 Governing equations of fluid flow

The Navier-Stokes equations describe the behaviour of Newtonian fluids. A Newtonian fluid is one for which the components of stress are linearly related to the components of the rate of strain, and the fluid properties are uniform in all directions, i.e. isotropic. Most common liquids and gases at ordinary temperatures and pressures conform to the Newtonian model.

In principle any flow of a Newtonian fluid is completely determined by:

a) the three Navier-Stokes equations of motion, which are represented by a single vector equation

$$\rho\frac{D\underline{q}}{Dt} = -\underline{\nabla}p + \mu\nabla^2\underline{q} + \frac{1}{3}\mu\underline{\nabla}\left(\underline{\nabla}.\underline{q}\right) + \rho\underline{B} \qquad \text{(A.1)}$$

where $\underline{q} = \{u,v,w\}$, the differential operator $\frac{D}{Dt} = \frac{\partial}{\partial t} + u\frac{\partial}{\partial x} + v\frac{\partial}{\partial y} + w\frac{\partial}{\partial z}$ and $\underline{B} = \{x,y,z\}$ is the body force vector. The coefficient of viscosity of the fluid is defined as μ; u,v,w are the x,y,z components of velocity; and ρ is the density.

b) the equation of continuity. (No fluid can be created or destroyed)

$$\rho\underline{\nabla}.\underline{q} + \frac{D\rho}{Dt} = 0 \qquad \text{(A.2)}$$

c) an internal energy equation

$$\frac{\partial(\rho i)}{\partial t} + \underline{\nabla}.\left(\rho i\underline{q}\right) = -p\underline{\nabla}.\underline{q} + \underline{\nabla}.\left(k\underline{\nabla}T\right) + \Phi + S_i \qquad \text{(A.3)}$$

where i is the specific internal energy and Φ is the dissipation of the internal energy, and S_i is a source term for internal energy and T is the temperature.

d) any thermodynamic relations between density (ρ), temperature (T) and pressure (p), and ρ, T and internal energy (i).

e.g. for a perfect gas:

$$p = \rho RT \tag{A.4}$$

$$i = C_v T \tag{A.5}$$

where R is the universal gas constant, T is the temperature and C_v is the specific heat capacity of a gas at a constant volume.

A.2 The Boussinesq concept

For turbulent flows, Boussinesq proposed that the Reynolds stresses are exactly proportional to the rates of strain, with the proportionality coefficient defining the turbulent (or eddy) viscosity of the fluid. This can be expressed mathematically (in tensor notation) as:

$$-\overline{u_i u_j} = \nu_t \left(\frac{\partial u_i}{\partial x_j} + \frac{\partial u_j}{\partial x_i} \right) - \frac{2}{3}\delta_{ij} k \tag{A6}$$

where u_i is the velocity vector $\{u, v, w\}$ and x_i is the position vector $\{x, y, z\}$, ν_t is the kinematic eddy viscosity, k is the turbulent kinemtic energy and δ_{ij} is the Kronecker delta function defined by:

$$\delta_{ij} = \begin{cases} 0 & if \quad i \neq j \\ 1 & if \quad i = j \end{cases} \tag{A7}$$

Therefore, the unknown correlation terms can be estimated if ν_t and k can be parameterised.

A.3 The $k \sim \varepsilon$ parameterisation

The $k \sim \varepsilon$ parameterisation uses an eddy viscosity hypothesis for the turbulence. An exact equation for k and ε can be derived from the Navier-Stokes equations [84]. The derivation will not be shown here. The complete $k \sim \varepsilon$ parameterisation equations are as follows:

$$\frac{\partial(\rho k)}{\partial t} + \underline{\nabla}.(\rho k \underline{q}) = \underline{\nabla}.\left(\frac{\mu_t}{\sigma_k}\underline{\nabla} k\right) + P - \rho\varepsilon \qquad \text{(A8)}$$

$$\frac{\partial(\rho k)}{\partial t} + \underline{\nabla}.(\rho \varepsilon \underline{q}) = \underline{\nabla}.\left(\frac{\mu_t}{\sigma_k}\underline{\nabla} \varepsilon\right) + \left(C_{1\varepsilon}\frac{\varepsilon}{k}P - C_{2\varepsilon}\rho\frac{\varepsilon^2}{k}\right) \qquad \text{(A9)}$$

$$\nu_t = C_\mu \frac{k^2}{\varepsilon} \qquad \text{(A10)}$$

where μ_t is the eddy viscosity, $\nu_t = \frac{\mu_t}{\rho}$ is the kinematic eddy viscosity, ρ is the density, $\underline{q} = \{u, v, w\}$, and P is the rate of turbulent production of k. The equations contain five adjustable constants C_μ, σ_k, σ_ε, $C_{1\varepsilon}$ and $C_{2\varepsilon}$. The standard $k \sim \varepsilon$ parameterisation employ values for the constants that are arrived at by comprehensive data fitting for a wide range of turbulent flows, and are listed in Table A1.

A.4 The RNG based $k \sim \varepsilon$ parameterisation

The RNG $k \sim \varepsilon$ parameterisation is derived from a Renormalisation Group analysis of the Navier-Stokes equations and differs from the standard model only through a strain-dependant modification to the term $C_{\varepsilon 1}$ and the use of a different set of model constants. According to Speziale and Thangam [91] the complete RNG $k \sim \varepsilon$ parameterisation equations are as A8, A9, and A10 with the exception of:

$$C_{\varepsilon 1} = 1.42 - \frac{\eta(1 - \eta/\eta_0)}{1 + \beta\eta^3} \qquad \text{(A11)}$$

where $\eta = \frac{Sk}{\varepsilon}$ is the ratio of the turbulent time scale and the mean flow time scale; and $S = \left(2\overline{S_{ij}}\,\overline{S_{ij}}\right)^{0.5}$ where $\overline{S_{ij}} = \frac{1}{2}\left(\frac{\partial \overline{u_i}}{\partial x_j} + \frac{\partial \overline{u_j}}{\partial \overline{u_i}}\right)$ is the mean rate of strain tensor; and constants $\eta_0 = 4.38$ and $\beta = 0.015$.

	C_μ	σ_k	σ_ε	$C_{1\varepsilon}$	$C_{2\varepsilon}$
$k-\varepsilon$	0.09	1.00	1.30	1.44	1.92
RNG $k-\varepsilon$	0.085	0.7179	0.7179	-	1.68

Table A.1 The coefficients for the two turbulence closure models.

TABLES

Name	Type	Length overll (LOA) (m)	Bridge to sea level (BH) (m)	Deck to sea level (F) (m)	Bridge length (L) (m)	Breadth (B) (m)
Siam	VLCC	332	26	11	14	58
Okinoshima Maru	VLCC	333	30	12	20	60
New Wisdom	VLCC	334	31	12	19	59
New Vitality	VLCC	330	29	10	18	56
Knock Clune	COT	274	25	8	-	44
GlenRoss	COT	247	25	7	15	42
George Shultz	COT	259	26	8	16	48
Eridge	BULK	266	22	7	14	41
EOS	COT	244	28	12	15	46
ELEO Maersk	VLCC	344	28	9	23	56
Cosmo Delphinus	VLCC	322	27	10	17	58
Berge Sigval	VLCC	332	28	10	17	58
Arosa	VLCC	328	27	9	18	58
Wilomi Tanana	COT	274	25	8	13	43
Nisyros	COT	274	24	8	15	45
New Fortuner	COT	277	27	8	16	44
Mayon Spirit	COT	245	27	9	12	41
Golar Stirling	VLCC	332	24	10	16	58
Chevron Atlantic	COT	269	24	7	14	46
Bergeland	BULK	339	24	10	15	55
Arabat	PT	183	23	6	11	32
Bunga Siantan	POT	143	17	6	11	22
Congor	ChT	170	19	7	12	25
Fandango	MT	183	4	10	13	32
Front Driver	OBO	285	22	7	15	45
Jo Alder	ChT	139	14	6	18	21
Katarina	ChT	102	16	2	15	18
Knock Allen	COT	274	26	8	16	44
Landsort	CO/PT	274	22	8	16	48
Olympic Serenity	COT	232	20	6	13	42
Salamina	PT	183	22	8	13	32
Solidarnosc	BULK	228	22	8	13	32
TS Prosperity	VLCC	338	30	11	14	58
Tirumalai	AT	175	21	4	-	31
Western Bridge	BULK	250	27	5	17	38
Yeoman Burn	BULK	245	24	6	13	32
BP Admiral	PT	176	21	7	16	31
China Pride	BULK	225	22	6	19	32
Dicto Knutsen	COT	243	26	10	15	43
Hanjin Gladstone	BULK	309	24	7	15	50
Jahre Traveller	COT	269	23	9	14	45
Onzo Spirit	COT	245	26	8	13	41
Sea Duke	COT	326	29	11	19	56
Zafra	CO/PT	229	22	6	14	32

Table 2.1 Dimensions (to the nearest meter) and type of tankers/bulk carriers taken from *Significant Ships* 1990 to 1993 [49].

ship dimension $= a + b * LOA$	tankers and bulk carriers		
	a	b	R^2
bridge to waterline, HB	10.65	5.15×10^{-2}	0.65
freeboard, F	1.54	2.54×10^{-2}	0.52
bridge length, L	10.16	1.98×10^{-2}	0.24
breadth, B	-3.00	0.18	0.93
Bridge to deck, H (H=HB-F)	9.11	2.6×10^{-2}	0.29

Table 2.2 Coefficients of the linear fit to the principal dimensions of tankers and bulk carriers extracted from *Significant Ships* 1990-1993 [49].

	Deck to Bridge Height	Bridge Height (BH)	Freeboard (F)	Bridge Length (L)	Breadth (B)
Tanker 1 (LOA= 170m)	13.5	19.4	5.9	13.5	27.3
Tanker 2 (LOA= 250 m)	15.6	23.5	7.9	15.1	41.6
Tanker 3 (LOA= 330 m)	17.7	27.6	9.9	16.7	55.9

Table 2.3 Dimensions of the three simple tanker ship shapes.

Name	Aft loading	LOA (m)	BH (m)	F (m)	L (m)	B (m)	H (m)	C_{bow} (m)	B_{aft} (m)
Contship Pacific	-	164	27	9	17	28	5	17	-
San Lorenzo	-	167	26	10	16	27	5	16	-
Tokyo Senator	-	216	31	13	13	32	4	21	-
Betelgeuse	4 Single	192	29	10	10	32	4	22	39
Cape Bonavista	-	140	22	9	9	23	-	-	-
Cape Hatteras	-	147	25	10	8	24	6	22	-
Hanjin Osaka	5 Single	290	31	13	20	32	7	25	52
Hyundi Admiral	4 long 1 single	275	32	12	15	37	7	21	68
Kairo	-	150	23	10	6.	22	4	15	-
Muscat Bay	2 Single	182	27	11	11	28	6	18	18
R. J. Pfeiffer	4 Long	218	30	16	10	32	7	22	59
Secil Angola	-	124	19	7	9	21	3	12	-
Uni Crown	2 Long	152	20	8	11	26	3	14	29
Zim Hong Kong	2 Long	236	32	13	14	32	8	18.9	32
Bunga Kenari	2 Single	177	26	12	12	28	7	25	26
Hanjin Bangkok	-	121	17	5	11	20	-	-	-
Hannover Express	3 Large	294	32	13	11	32	8	19	56
Kota Wijaya	4 Single	185	20	11	8	28	6	20	33
Nedlloyd Europa	4 Large 2 Single	266	31	13	18	32	7	9	73
Vladivostok	2 Single	237	31	13	13	32	10	21	35
Cap Polonio	-	200	29	12	15	32	7	19	-
CGM Provence	-	177	26.0	10	12	28	6	17	-
Katherine Sif	-	134	26	8	7	23	5	15	-
Nordlight	2 Single	157	25	9	9	23	6	19	22
Roberta Jull	-	93	18	7	5	15	3	13	-
Sea Bird	-	94	15	6	7	16	2	9	-
Serenity	2 Single	159	22	9	12	23	3	19	42

Table 2.4 Dimensions (to nearest meter) of two types of container ship: 1) forward loading and 2) aft loading.

dimension = $a + b * LOA$	Forward loading		Forward and aft loading	
	a	b	a	a
bridge to waterline height, BH	5.54	0.12	10.95	7.7×10^{-2}
free board, F	0.66	5.59×10^{-2}	5.37	2.9×10^{-2}
bridge length, L	-0.91	7.68×10^{-2}	2.96	4.42×10^{-2}
breadth, B	2.28	0.145	15.32	6.7×10^{-2}
bridge to container top, H	-3.28×10^{-2}	3.01×10^{-2}	1.2	2.3×10^{-2}
container front to bow, C_{bow}	4.63	7.55×10^{-2}	18.70	2.78×10^{-3}
bridge aft to aft edge of hull, B_{aft}	not used	not used	-13.16	0.254

Table 2.5 Coefficients of the linear fit to principal dimensions of container ships extracted from *Significant Ships* 1990-1993 [49].

y	Forward loading		Forward and aft loading	
	Container 1 LOA = 125 m	Container 2 LOA = 180 m	Container 3 LOA = 180 m	Container 4 LOA = 270 m
BH	20.5	27.1	24.8	31.7
F	7.7	10.7	10.6	13.2
L	8.7	12.9	10.9	14.9
B	20.4	28.4	27.4	33.4
H	3.7	5.4	5.3	7.4
C_{bow}	14.1	18.2	19.2	19.5
B_{aft}	not used	not used	32.6	55.5

Table 2.6 Dimensions of the fore, and fore and aft loading generic container ship shapes.

	Ship length, l (m)	Wind speed, U (ms^{-1})	Reynolds number, R_e
Wind tunnel scale	3.7	7	1.8×10^{6}
Full-scale	170	10	1.2×10^{8}

Table 3.1 A comparison of the Reynolds number, R_e, for the full scale and wind tunnel scale flows.

LOA, m	Container top to waterline height, m H	Bow to waterline height, m H	Container front to bridge distance, m	Depth of recirculation region at bridge, m		Bridge to deck height, m
	Case (a)	Case (b)		(a)	(b)	
100	14.57	6.25	81.05	16.8	11.5	2.97
150	19.35	9.05	123.43	24.1	17.1	4.48

Table 3.2 The predicted depth of the decelerated region in front of the bridge of a container ship.

Name	Model size	Step height, H (m)	Mesh resolution	Turbulence model	Total number of cells	y^+	Section model was included in
Channel flow [64]	full	0.025	0.024H	k-eps and RNG k-eps	243,696	14 <y^+ <40	4.3.2
Channel flow [64]	full	0.025	0.016H	RNG k-eps	519,886	12 <y^+ <40	4.3.2
Boundary layer flow [65]	full	0.2	0.023H	k-eps and RNG k-eps	280,180	15 <y^+ <30	4.3.3
Tanker (RUN A)	full	13.54	0.040H	RNG k-eps	147,293	3000 <y^+ <4000	4.4.2a
Tanker (RUN B)	full	13.54	0.038H	RNG k-eps	270,305	3000 <y^+ <4000	4.4.2a
Tanker (RUN C)	full	13.54	0.018H	RNG k-eps	427,230	2500 <y^+ <4000	4.4.2 a, b, c, d
Tanker (RUN D)	full	13.54	0.018H	k-eps	427,230	2500 <y^+ <4000	4.4.2b
tanker (RUN E)	Full. (uniform inlet profile)	13.54	0.018H	RNG k-eps	427,230	2500 <y^+ <4000	4.4.2c
Tanker (RUN F)	scaled	0.14	0.018H	RNG k-eps	427,230	20<y^+< 100	4.4.2d
container ship	scaled	0.106	0.031H	RNG k-eps	692,638	40<y^+< 200	4.5
tanker	scaled	0.294	0.011H	RNG k-eps	631,754	35 <y^+< 300	4.5
deck house	scaled	0.422	0.008H	RNG k-eps	485,699	40<y^+< 200	4.5

Table 4.1 The various CFD models used to predict the flow over the bluff body shapes.

Anemometer	Height (m)	Angle, θ, (degrees) for relative wind direction						
		-90°	-30°	-15°	0°	15°	30°	90°
HS sonic	15.2	6	7	7	7	8	8	9
R2 sonic	19.6	11	2	3	4	3	4	13
anemometer A	18.45	11	2	3	5	4	4	14
anemometer B	17.45	11	2	3	5	3	3	15
anemometer C	16.45	9	0	3	4	2	0	16
anemometer D	15.78	6	-2	3	3	0	-3	16
anemometer E	14.45	-1	-5	1	-14	-5	-12	13

Table 5.1 The CFD predicted angle, θ, of the flow to the horizontal at the anemometer sites on the *RRS Charles Darwin*.

Anemometer	Height (m)	Absolute wind speed error (%) for relative wind direction						
		-90°	-30°	-15°	0°	15°	30°	90°
HS sonic	15.2	**7.3**	-1	-6.1	-8.4	-6.9	-6.1	**3.8**
R2 sonic	19.6	**7.6**	7.7	6.9	4.4	5.6	5.9	**7.5**
anemometer A	18.45	**5.2**	9.0	8.4	1.9	6.8	7.0	**8.2**
anemometer B	17.45	**-0.4**	9.2	9.1	-2.5	7.3	7.4	**8.4**
anemometer C	16.45	**-18**	5.5	8.4	-7.6	6.7	7.1	**6.9**
anemometer D	15.78	**-38**	3.8	3.6	-13.4	3.2	5.9	**0**
anemometer E	14.45	**-78**	-36	-61	-87	-50.2	-15.0	**-47.8**

Table 5.2 The CFD predicted wind speed error for anemometers on the *RRS Charles Darwin*. A negative value indicates that the anemometer is located in a region of decelerated air flow.

FIGURES

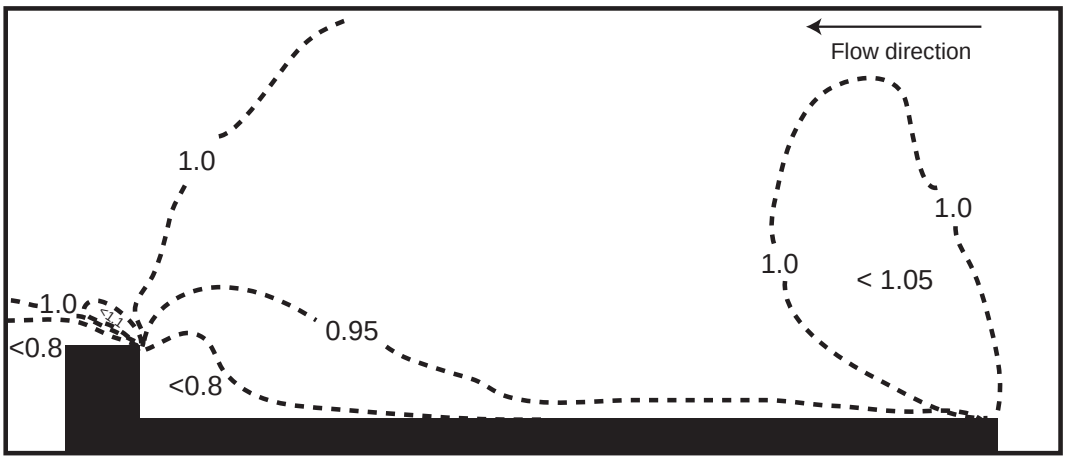

Figure 1.1 A numerical simulation of the air flow over a simple generic tanker ship shape.

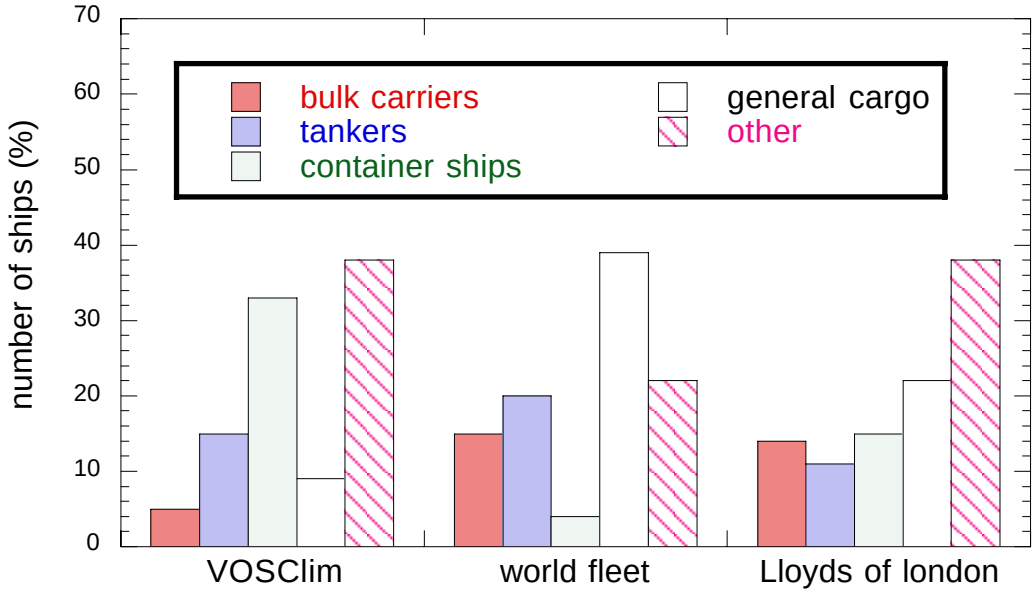

Figure 2.1 Merchant ships as a proportion of the VOSClim project [52] and as a percentage of the world fleet (ISL, [53]) and as a percentage of the ships registered by Lloyds of London during 1999.

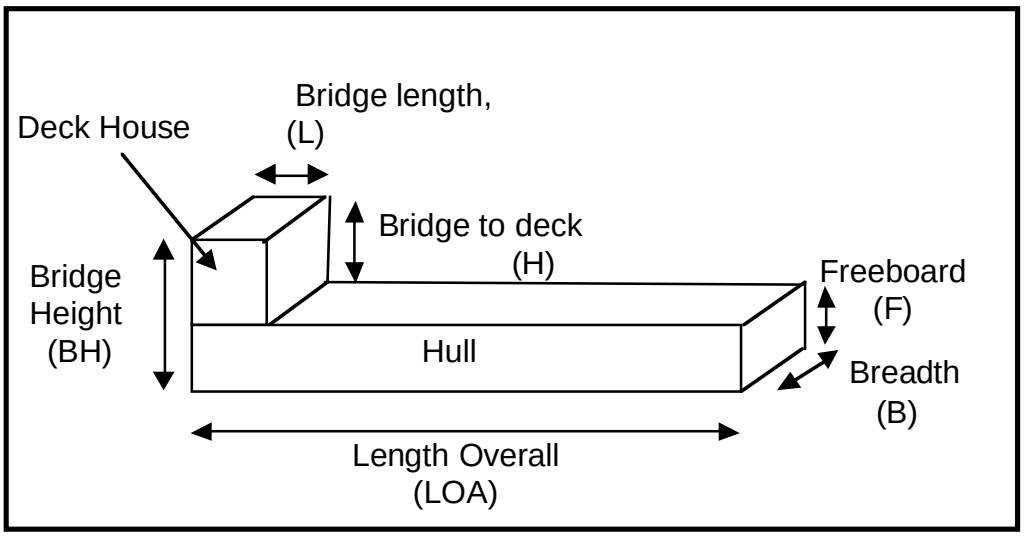

Figure 2.2 The shape and principal dimensions of a block geometry representation of a tanker.

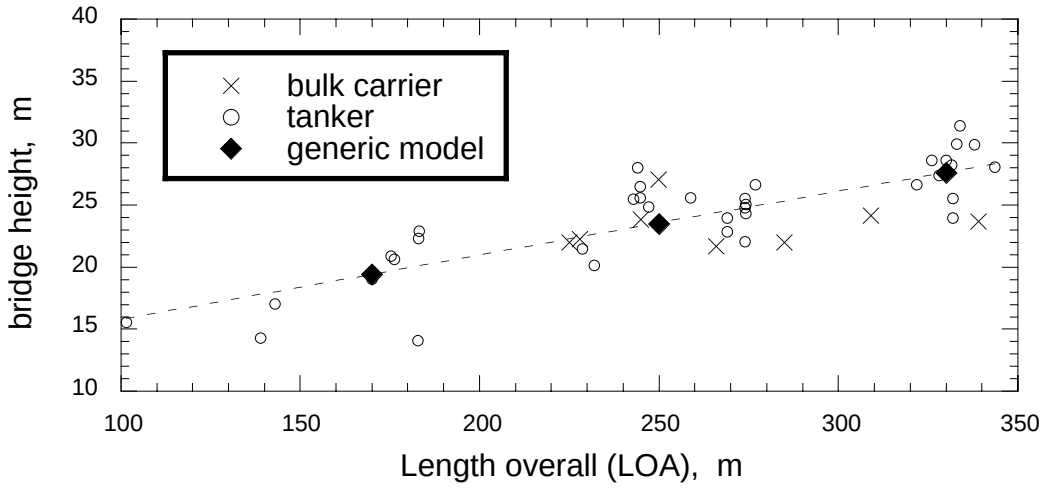

Figure 2.3 The bridge to waterline height (BH) from [49]. The dimensions of the generic model are overlaid.

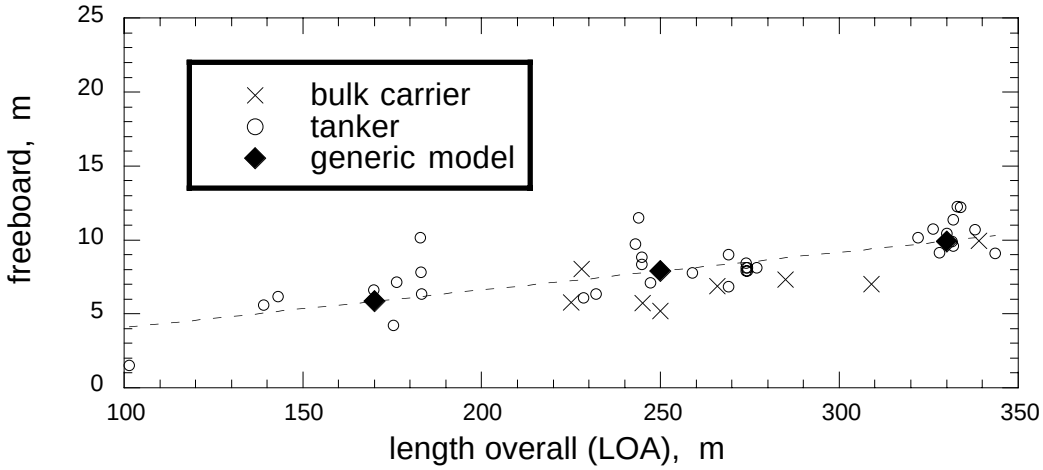

Figure 2.4 As Figure 2.3, but for the height of the freeboard (F).

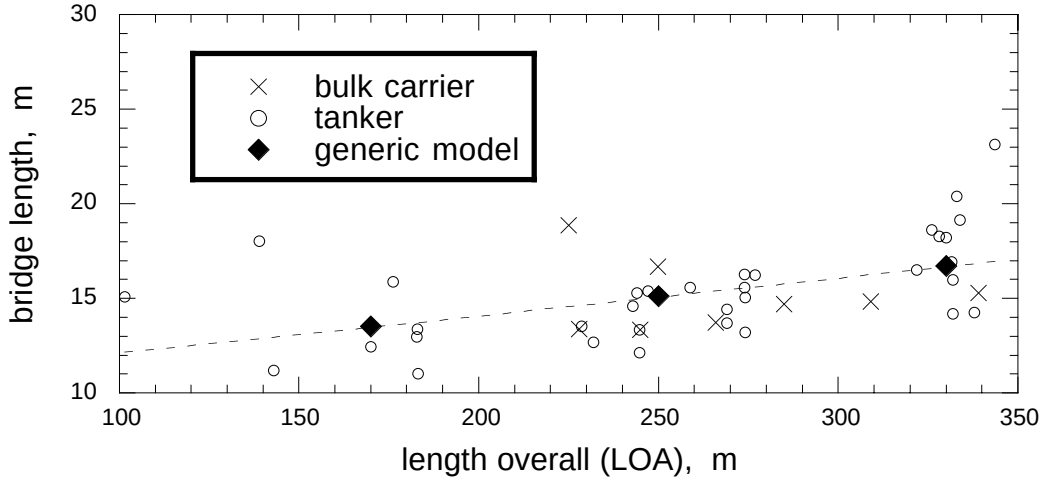

Figure 2.5 As Figure 2.3, but for the bridge length (L).

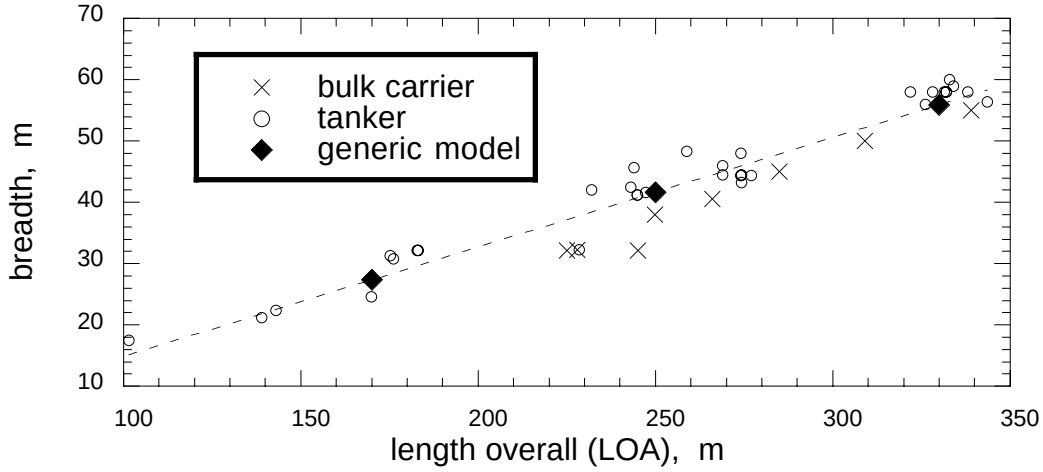

Figure 2.6 As Figure 2.3, but for the ship's breadth (B).

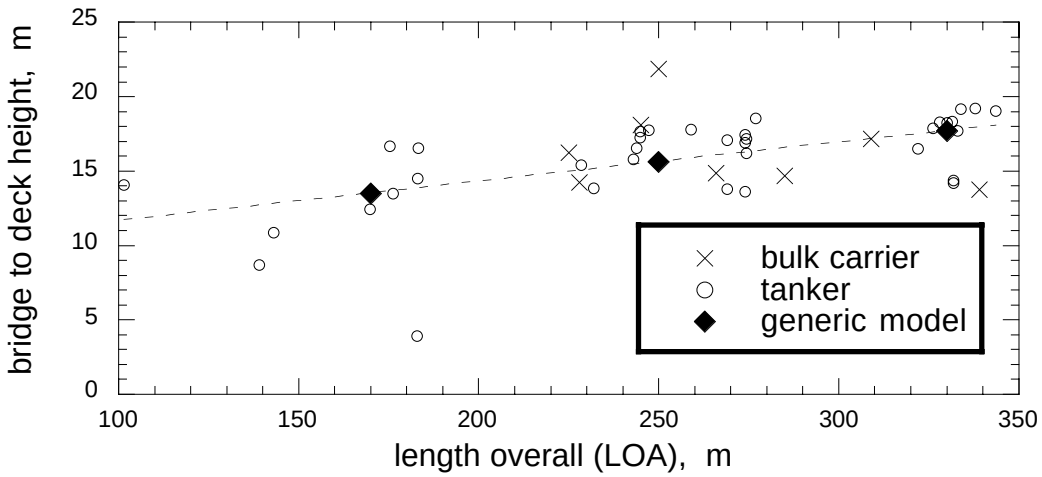

Figure 2.7 As Figure 2.3, but for bridge to deck height (H).

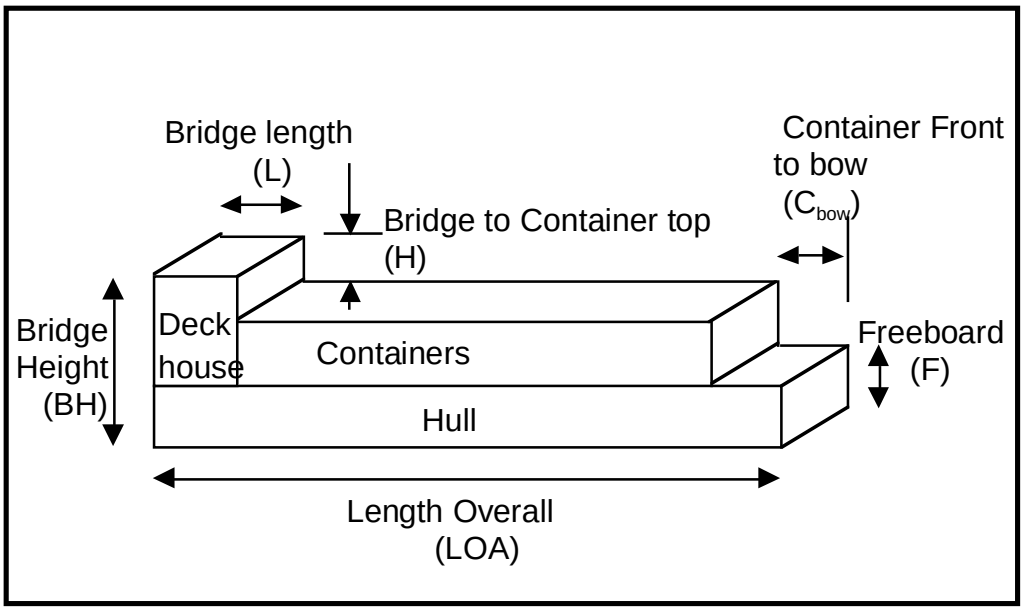

Figure 2.8 a) Illustration showing dimensions of a forward loading bluff body generic representation of a container ship.

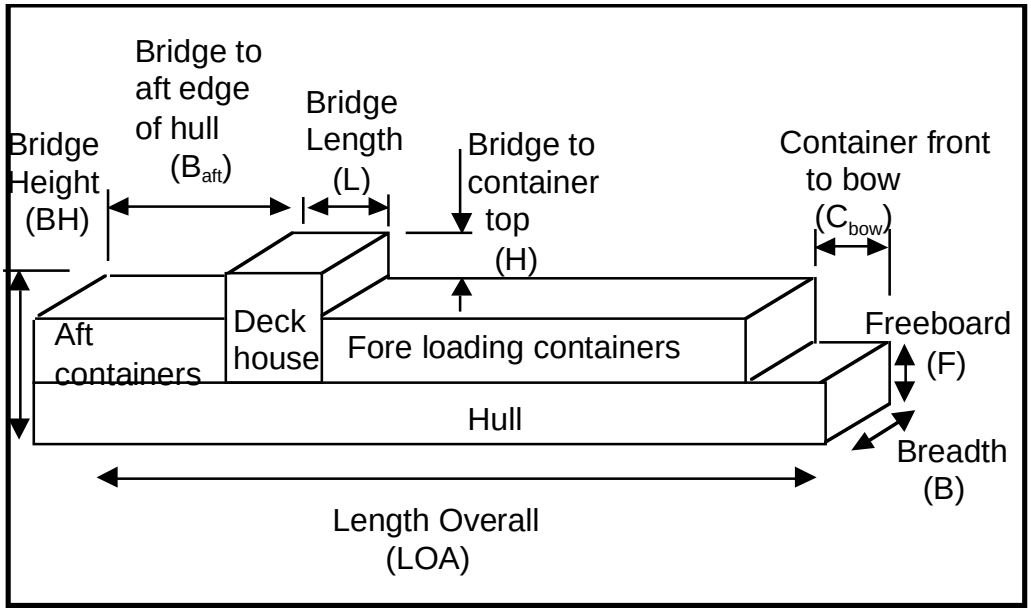

Figure 2.8 b) Illustration showing dimensions of a fore-and-aft-loading bluff body representation of generic container ship. Containers are loaded in front and behind the deck house.

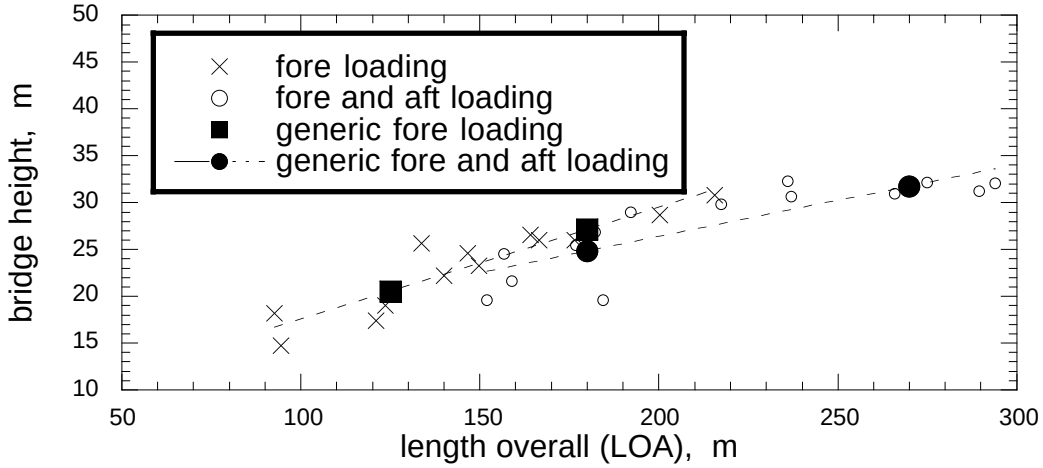

Figure 2.9 The bridge height above the sea surface, BH, for container ships with forward loading containers and fore and aft loading containers.

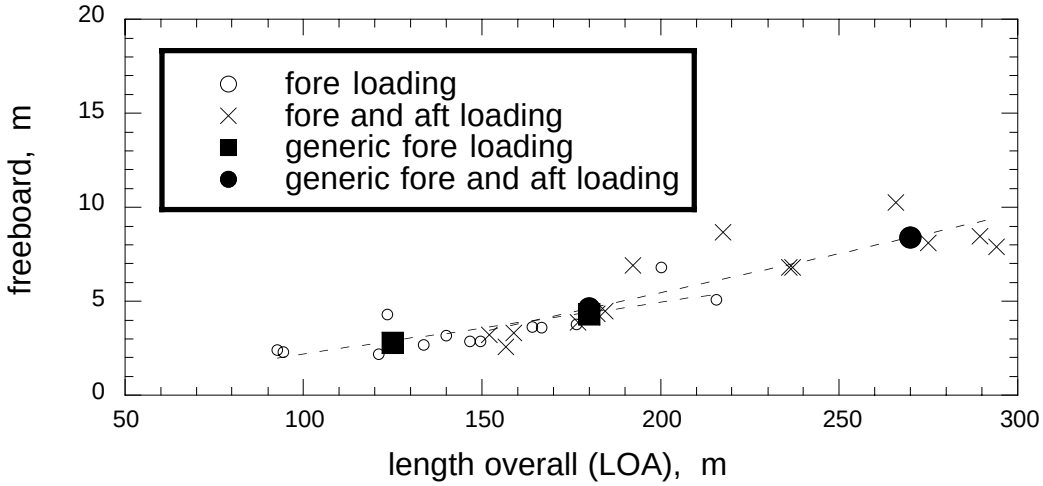

Figure 2.10 As for Figure 2.9, but for the freeboard (F).

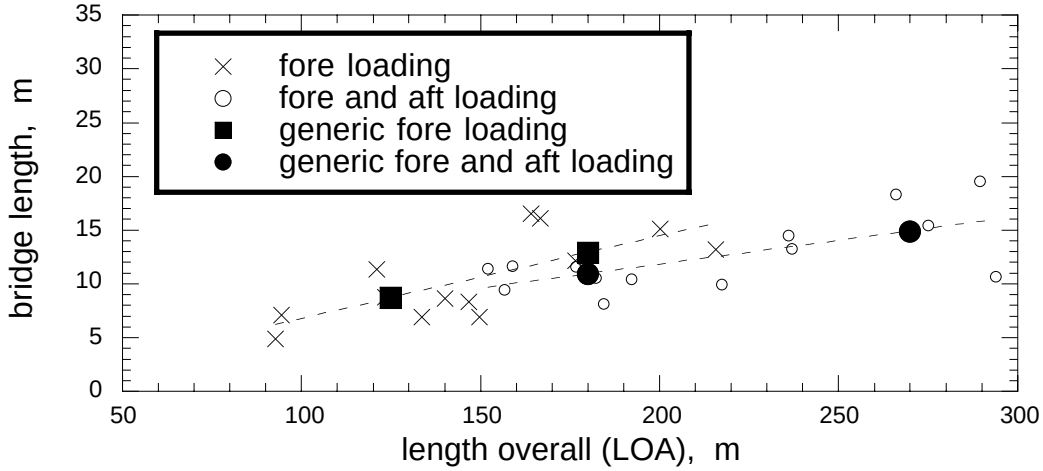

Figure 2.11 As for Figure 2.9, but for the bridge length (L)

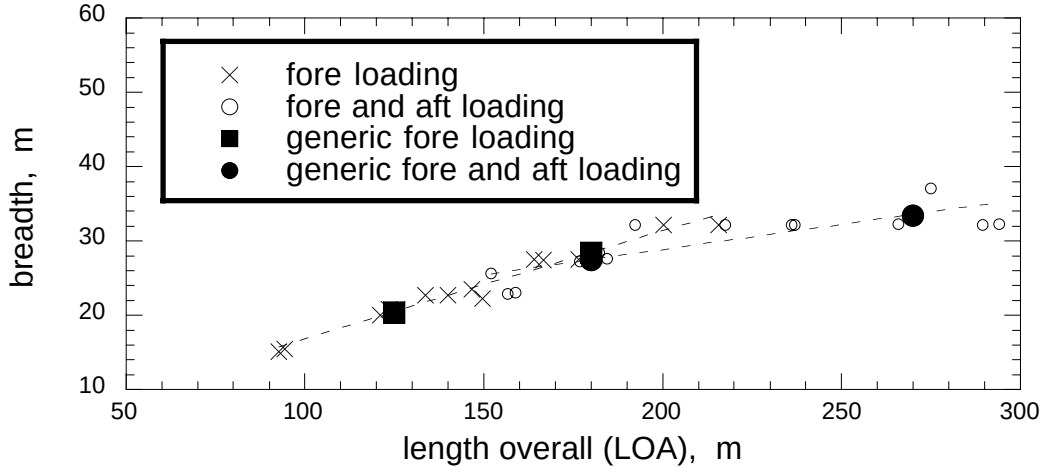

Figure 2.12 As for Figure 2.9, but for the ship's breadth (B).

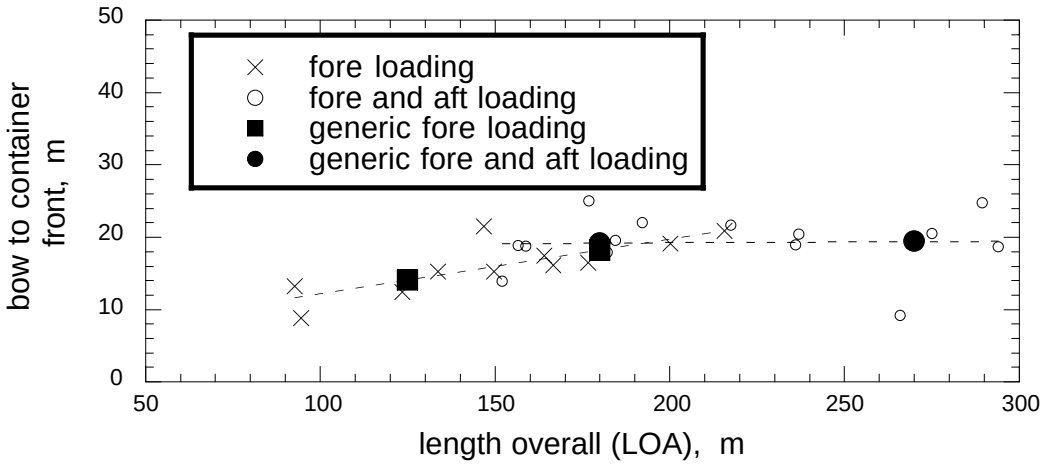

Figure 2.13 As for Figure 2.9, but for the distance from the container front to the bow (C_{bow}).

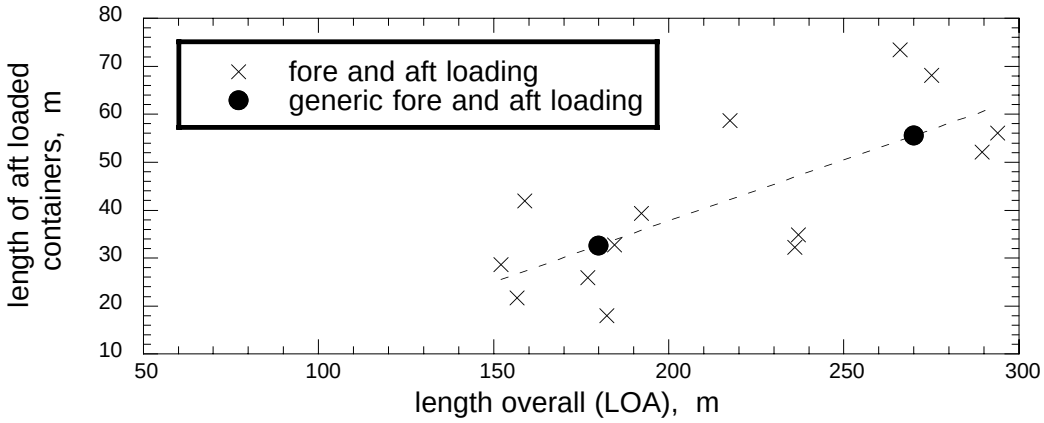

Figure 2.14 As for Figure 2.9, but for the length of the aft loaded containers (B_{aft}).

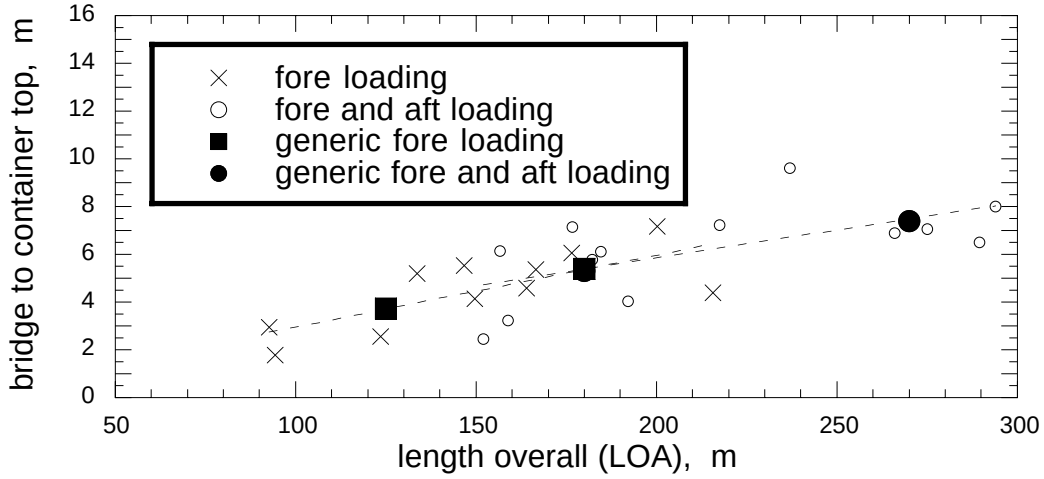

Figure 2.15 As for Figure 2.9, but for the bridge to container top height (H).

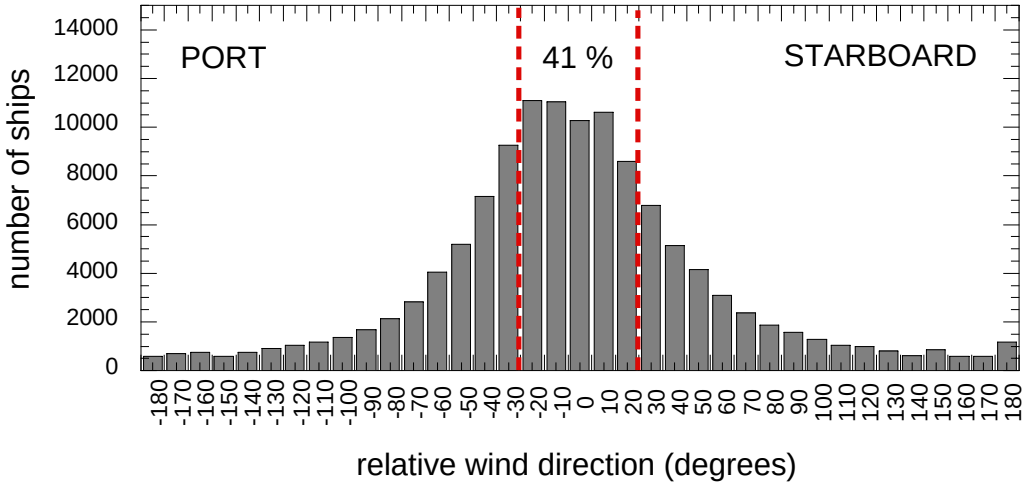

Figure 3.1 Relative wind speed distribution for merchant ships reporting to the Combined Ocean Atmosphere Data Set COADS for July 1986.

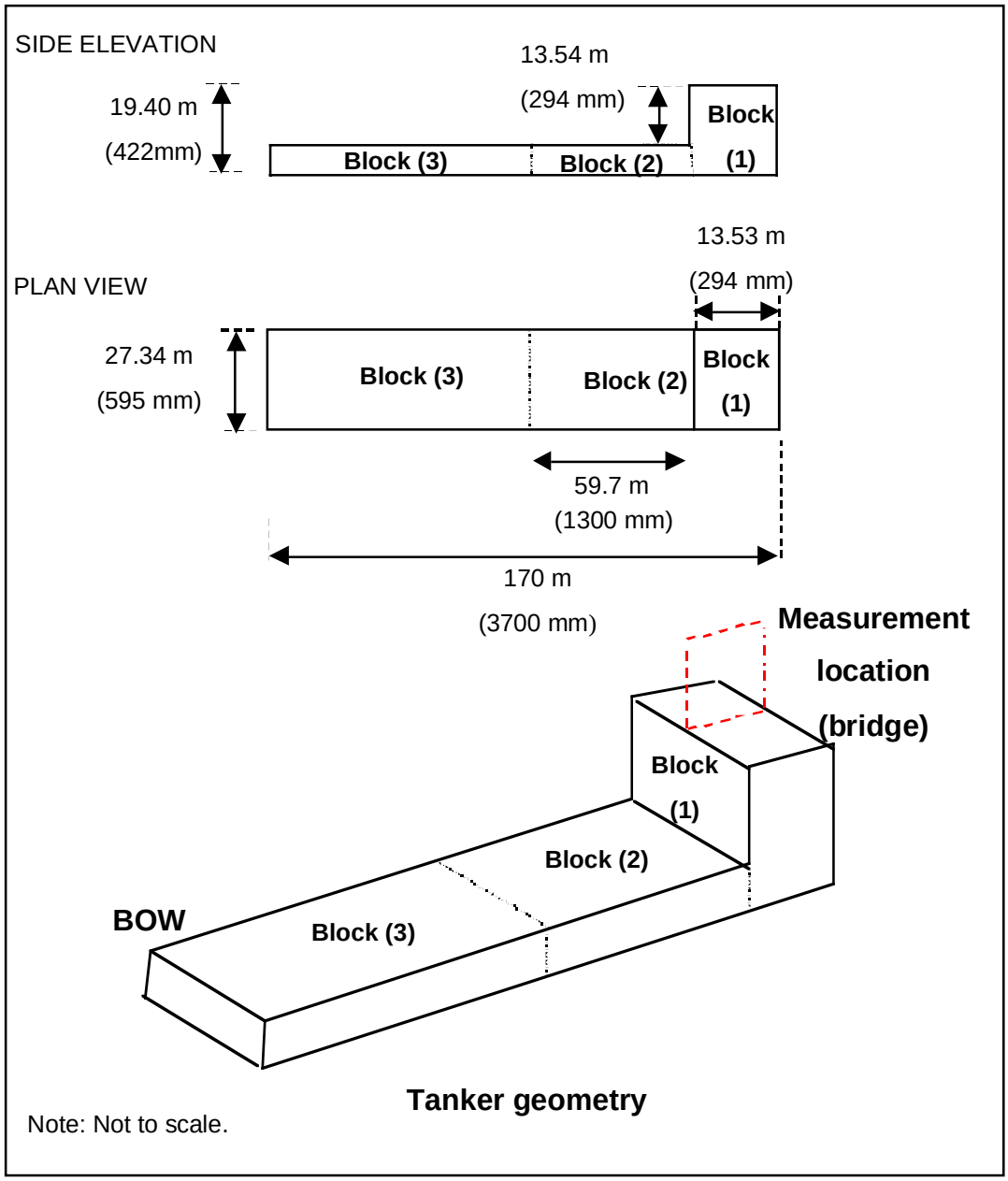

Figure 3.2 A schematic of the generic tanker geometry, with actual dimensions in parenthesis adjacent to scaled dimensions.

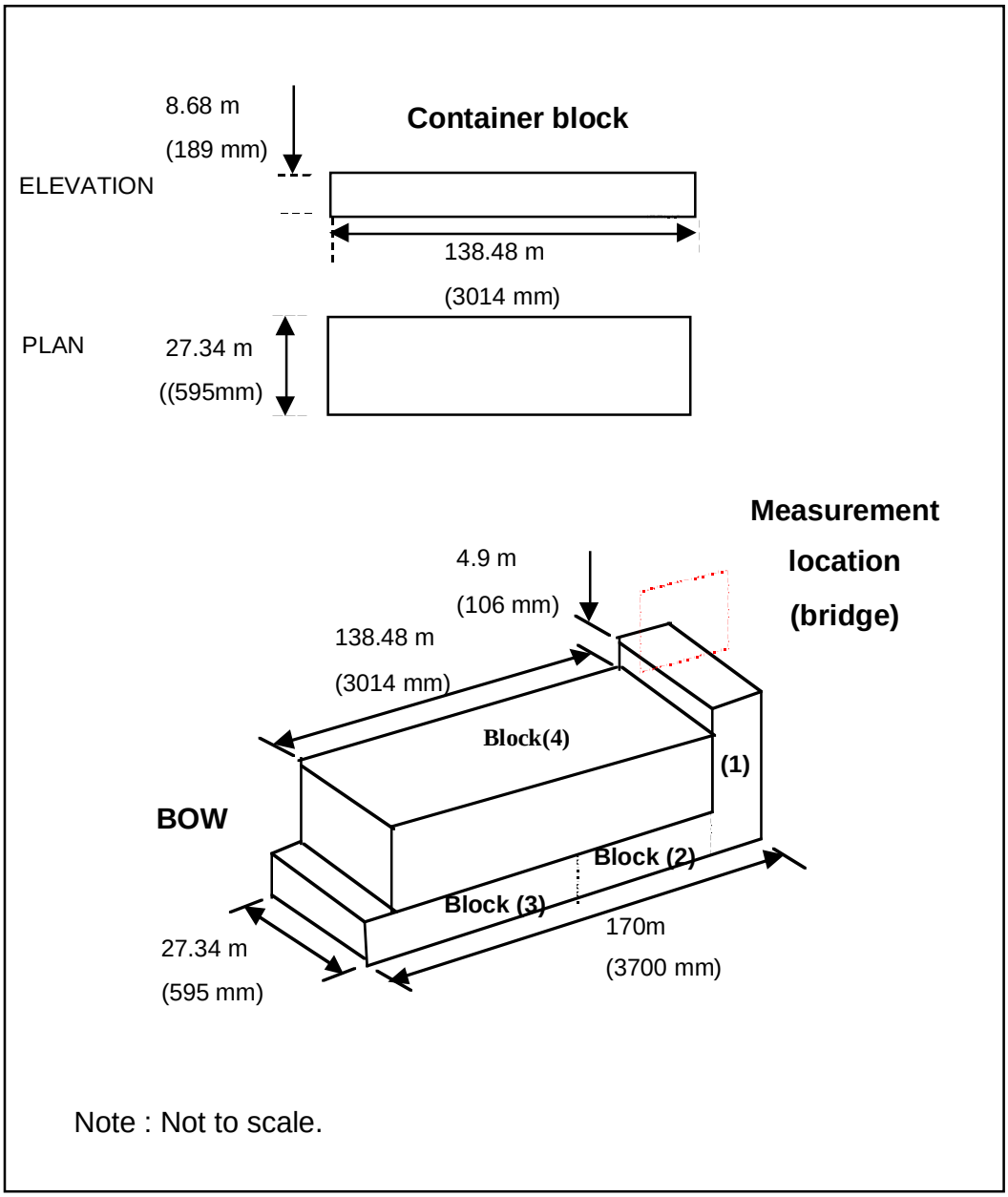

Figure 3.3 As Figure 3.2, but including a block which converts the tanker geometry into a model of a front-loading container ship.

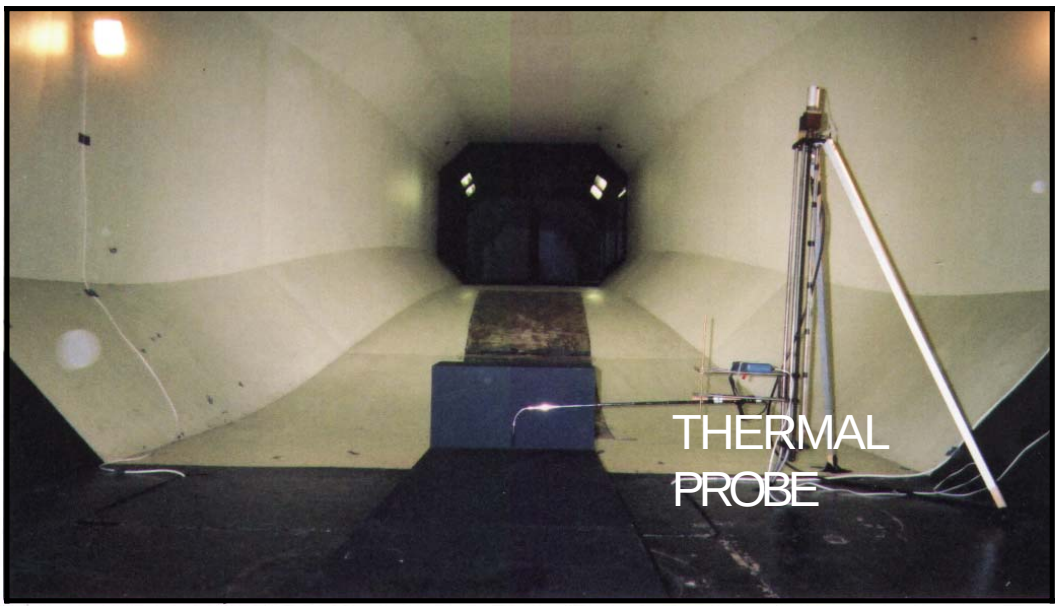

Figure 3.4 The Southampton University wind tunnel. The thermal probe is located in front of the bridge of the tanker and the view is looking downstream towards the high speed section.

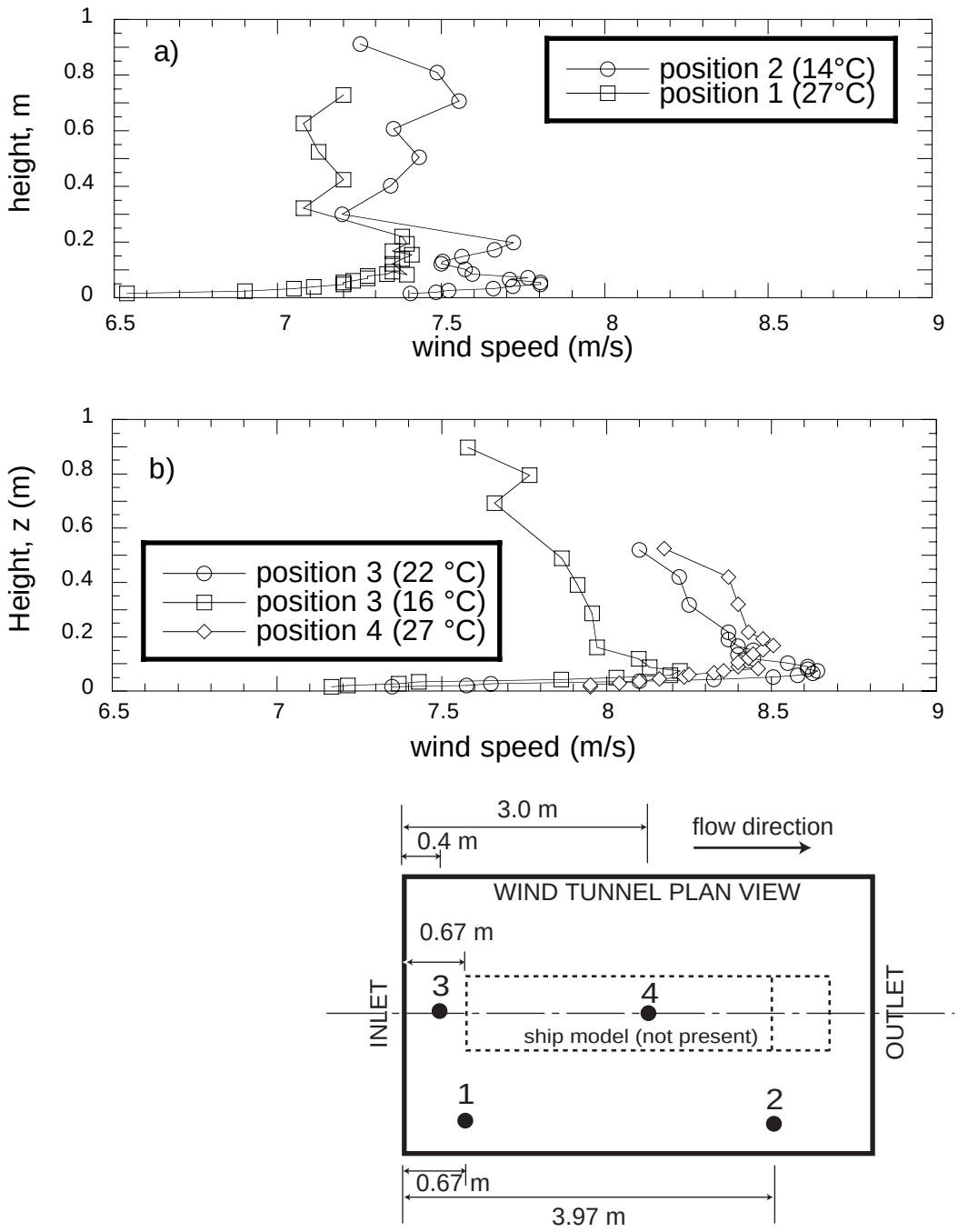

Figure 3.5 The variation in the free stream wind speed in the tunnel with variation in temperature.

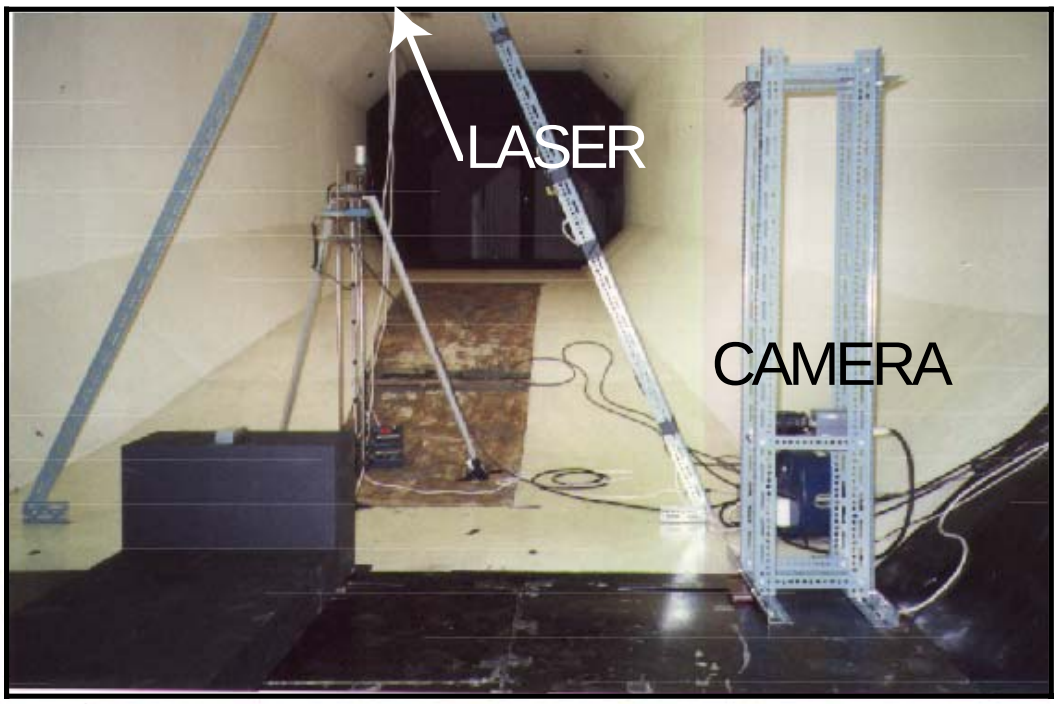

Figure 3.6 As Figure 3.4, but showing the PIV system.

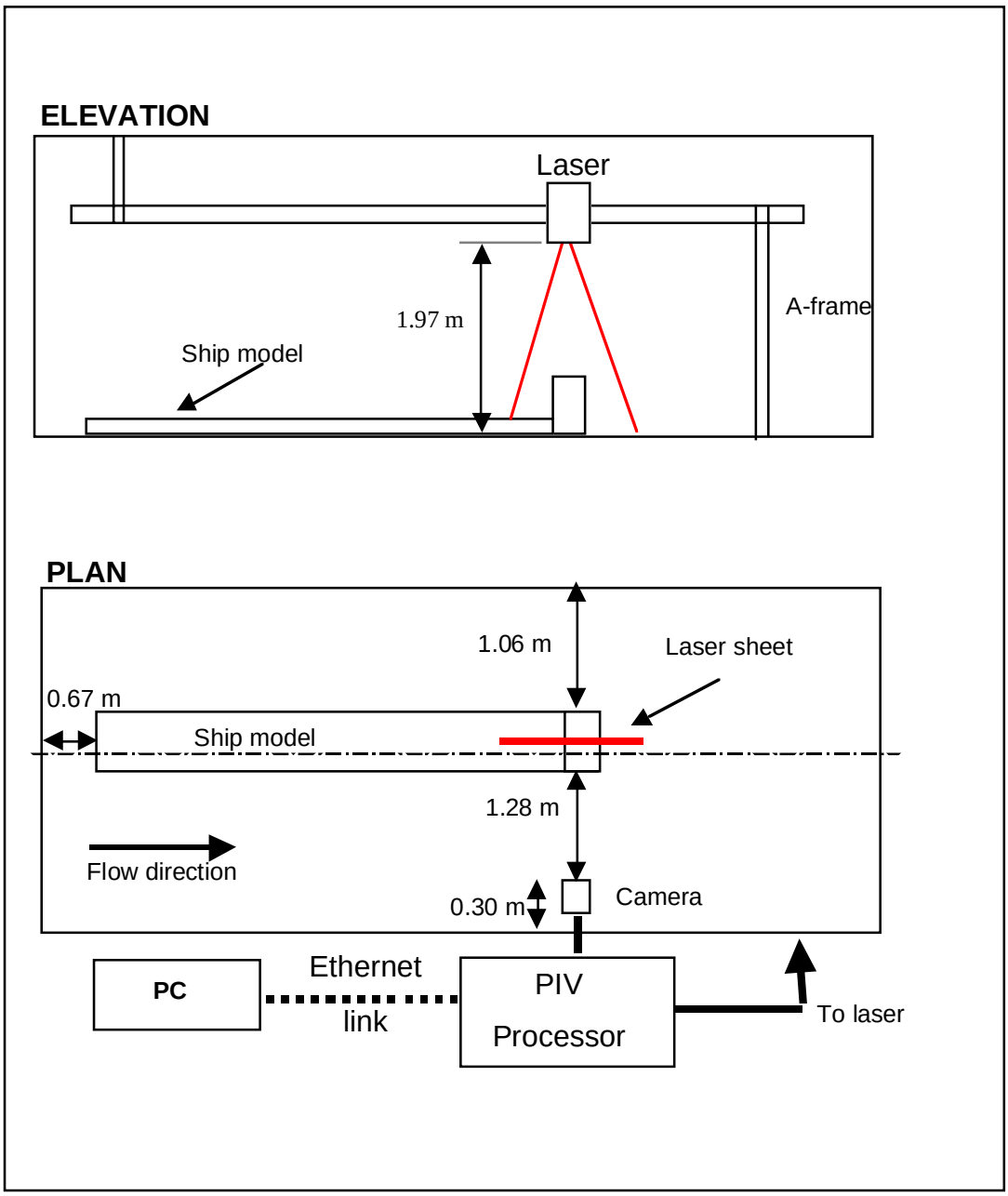

Figure 3.7 Schematic representing the PIV experiment.

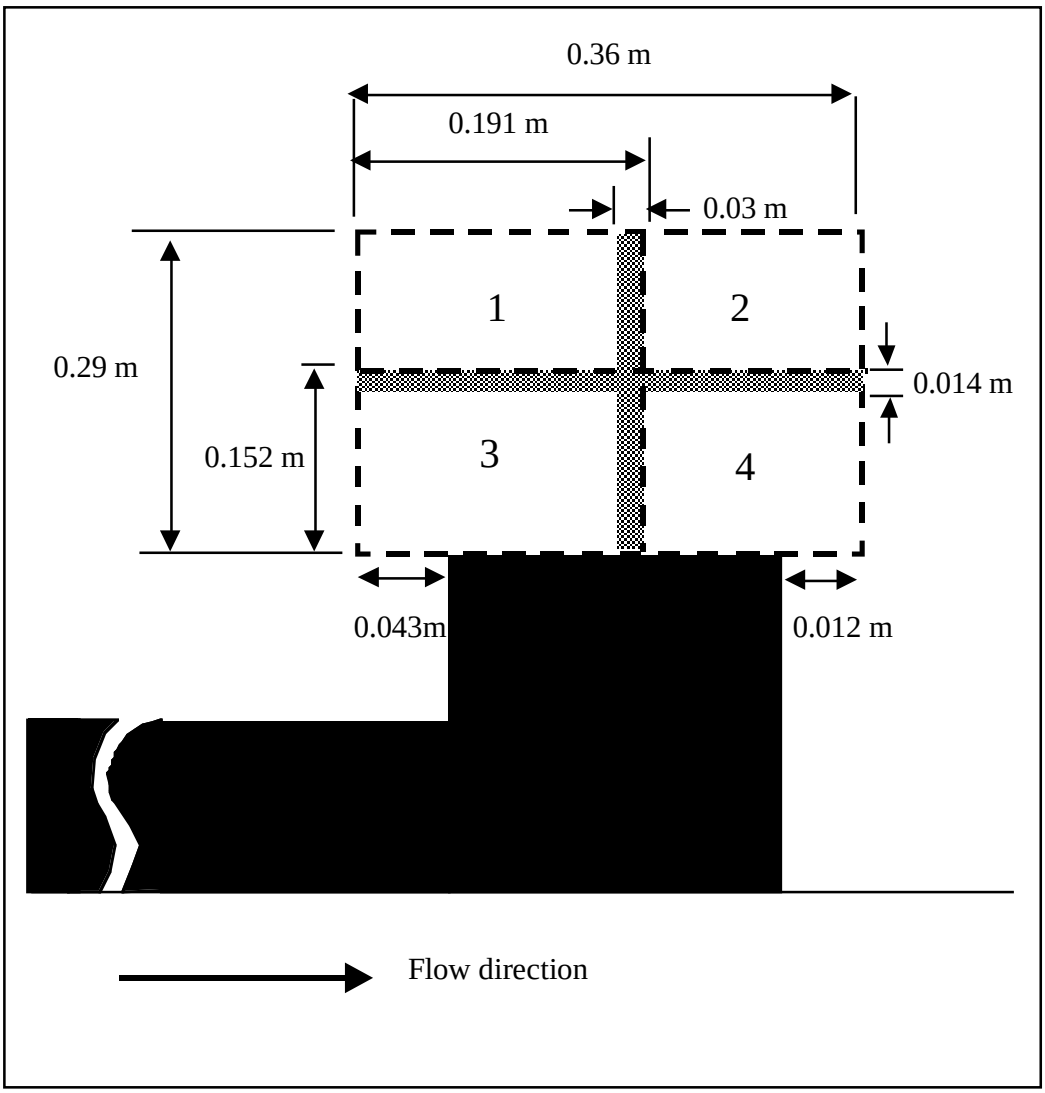

Figure 3.8 The four PIV measurements areas above a model geometry. The shaded areas defined the overlap between measurement areas.

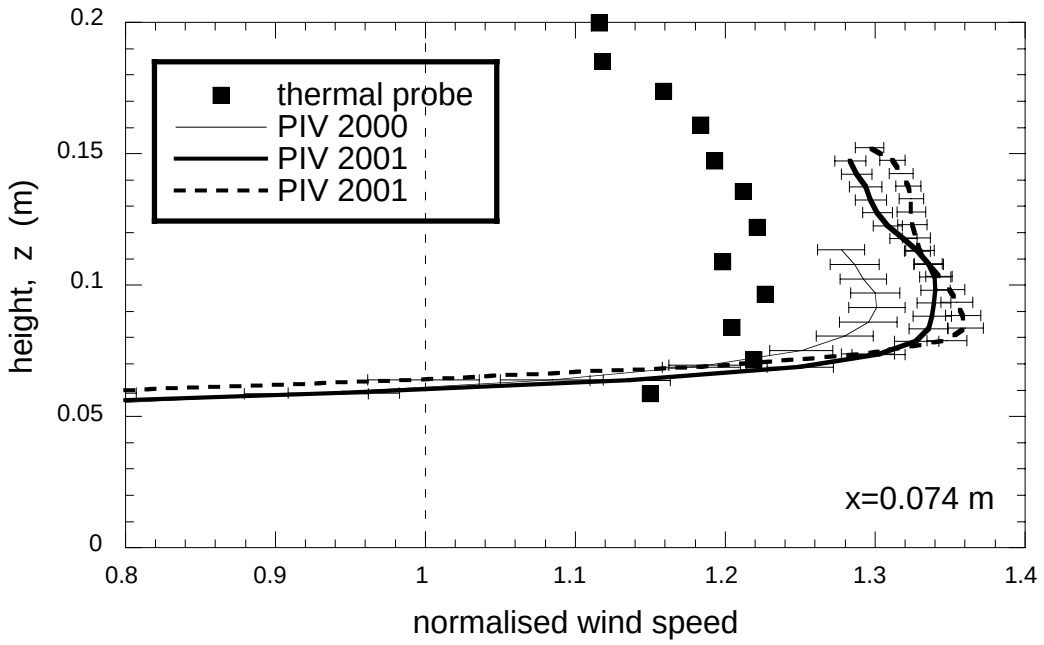

Figure 3.9 Normalised wind speed profiles above the bridge of the tanker.

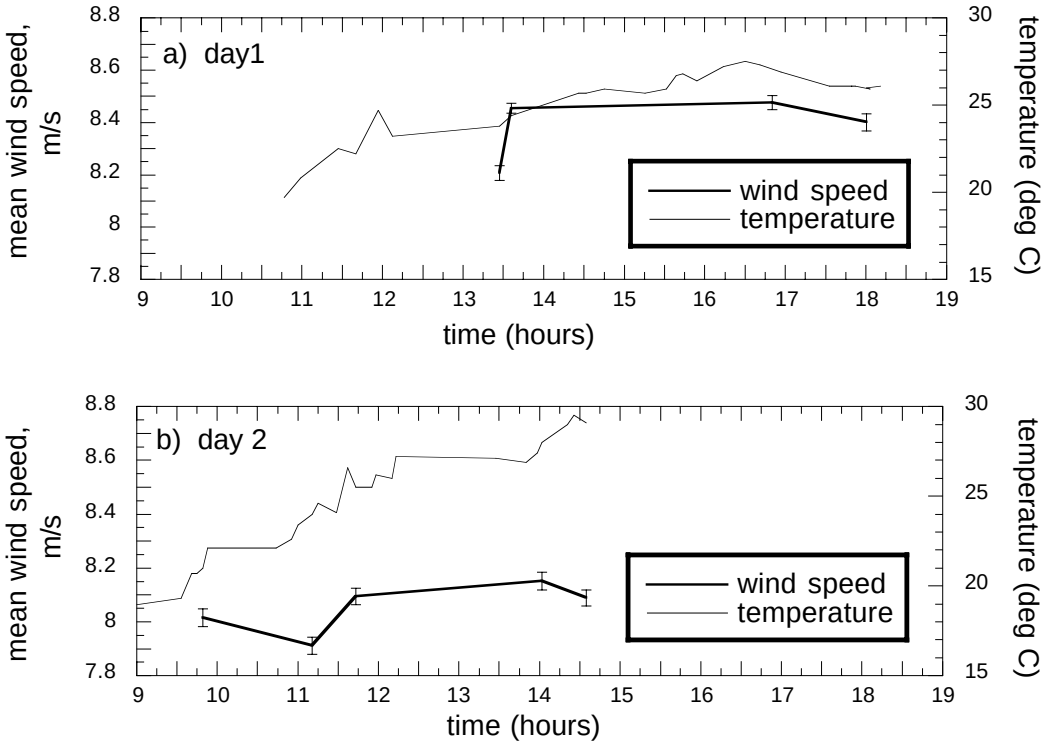

Figure 3.10 A time series of the thermal probe measured free stream wind tunnel speed and temperature during the PIV 2000 experiment.

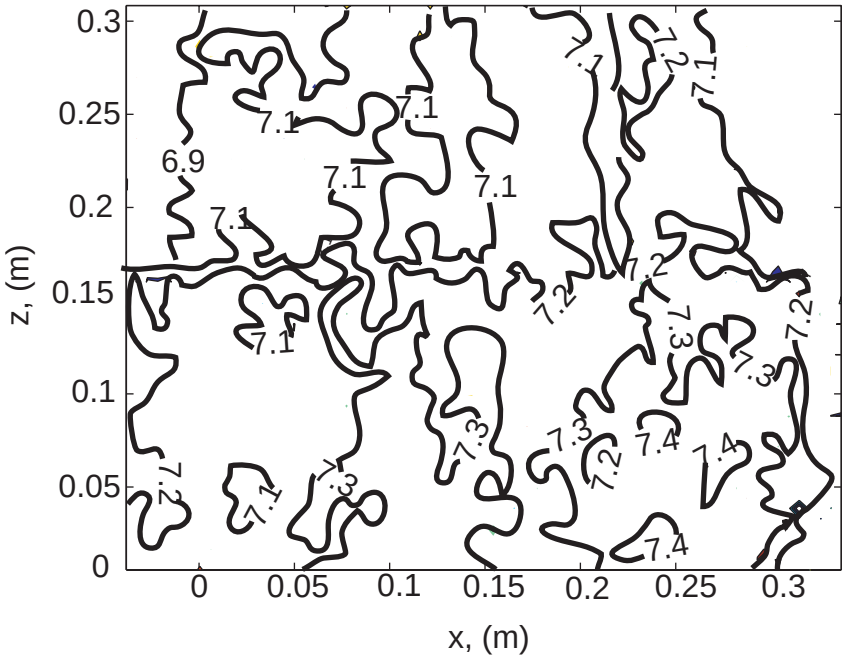

Figure 3.11 The PIV measured free stream wind speed in the Southampton University wind tunnel during the PIV 2000 experiment with no ship geometry present.

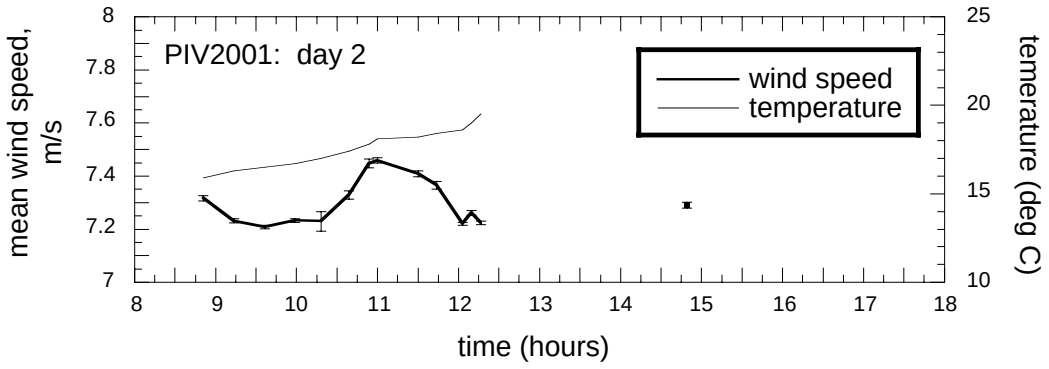

Figure 3.12 Time series of the mean free stream wind tunnel speed and temperature with the wind tunnel run with varying dynamic pressure.

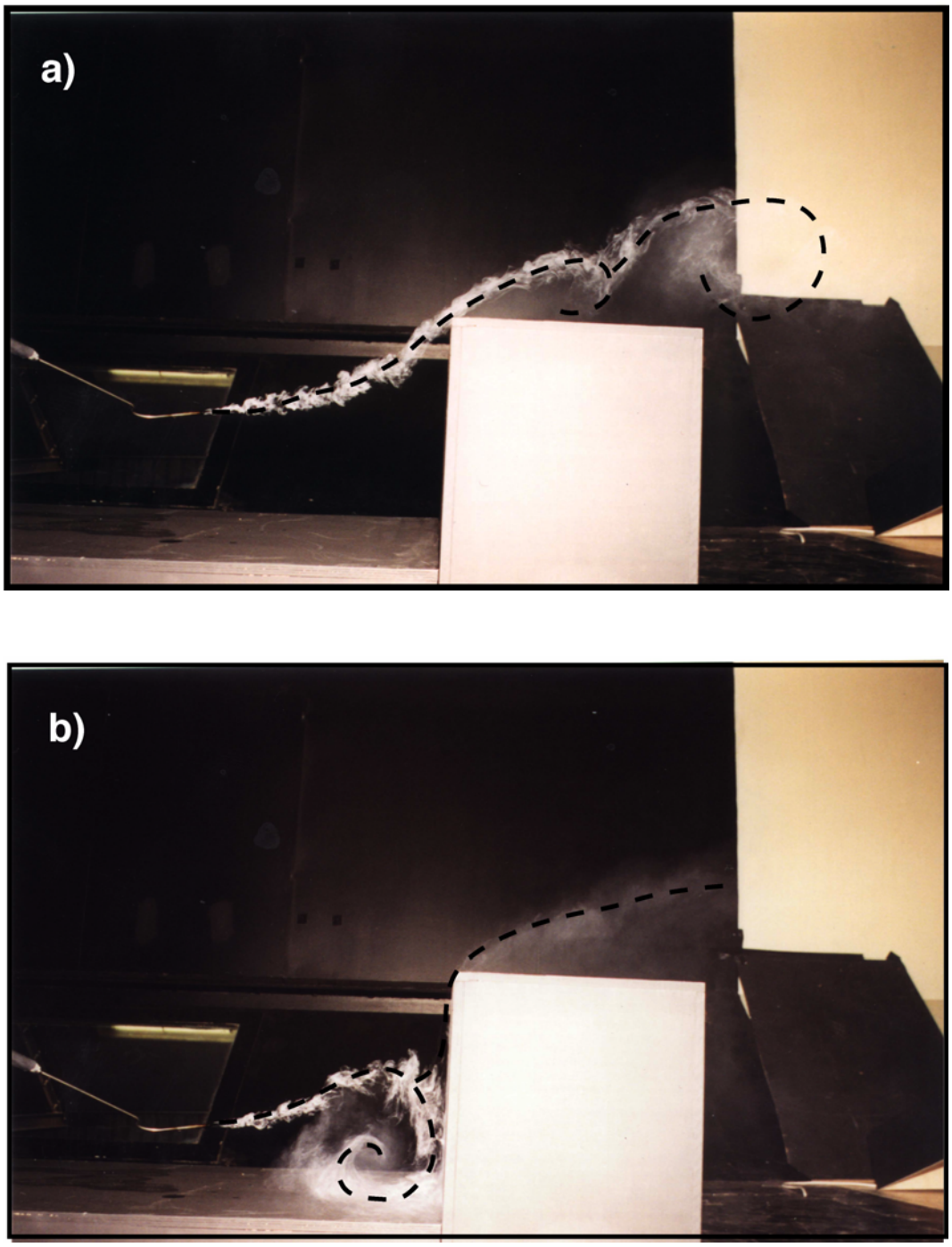

Figure 3.13 Flow visualisation above (a) and in front of (b) the bridge of the generic tanker geometry. The dashed line indicates the path of the smoke.

Figure 3.14 Flow visualisation above the bridge of the container ship. The dashed line indicates the path of the smoke.

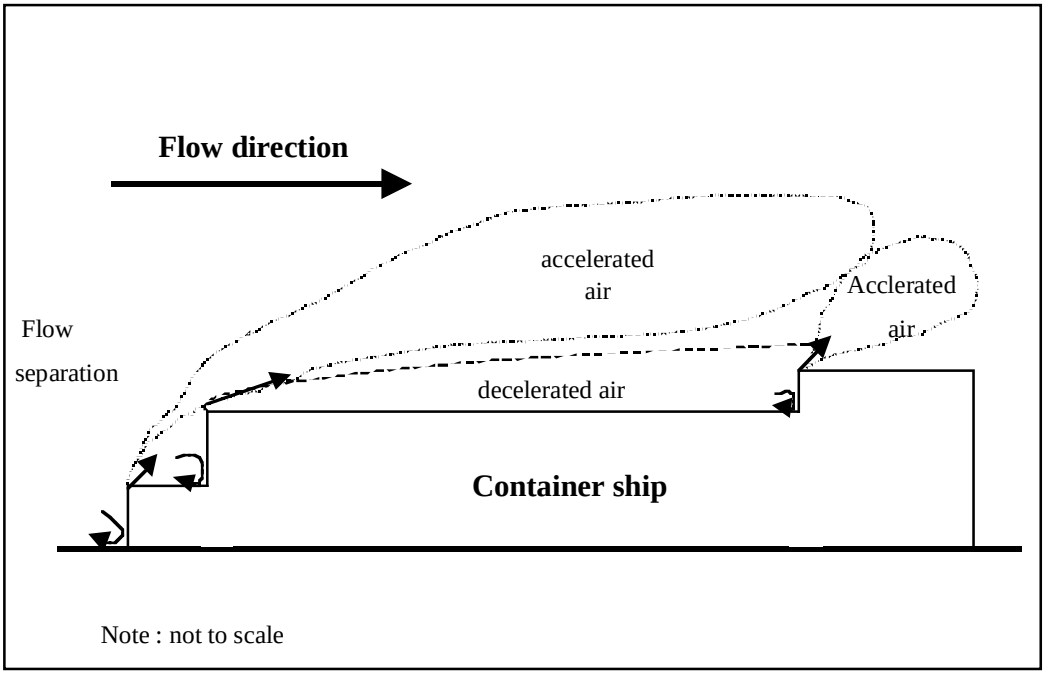

Figure 3.15 An illustration of the possible flow field over the bow and bridge of a container ship.

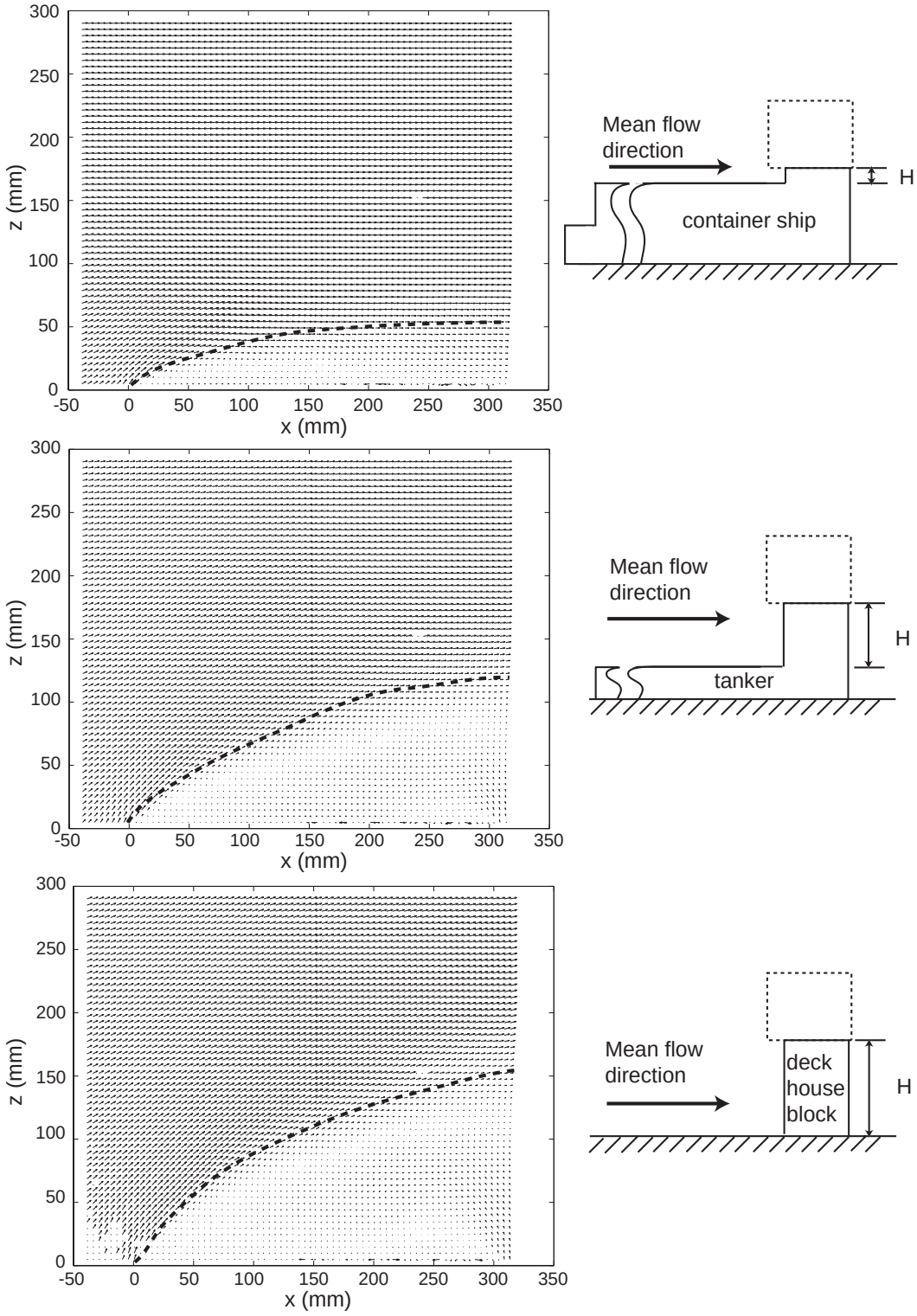

Figure 3.16 PIV measured velocities; top row - above the bridge of the containership geometry (step height=H=0.10 m); middle row - above the bridge of the tanker model (step height H=0.29 m), and bottom row - above the deck house block (step height H=0.42 m).

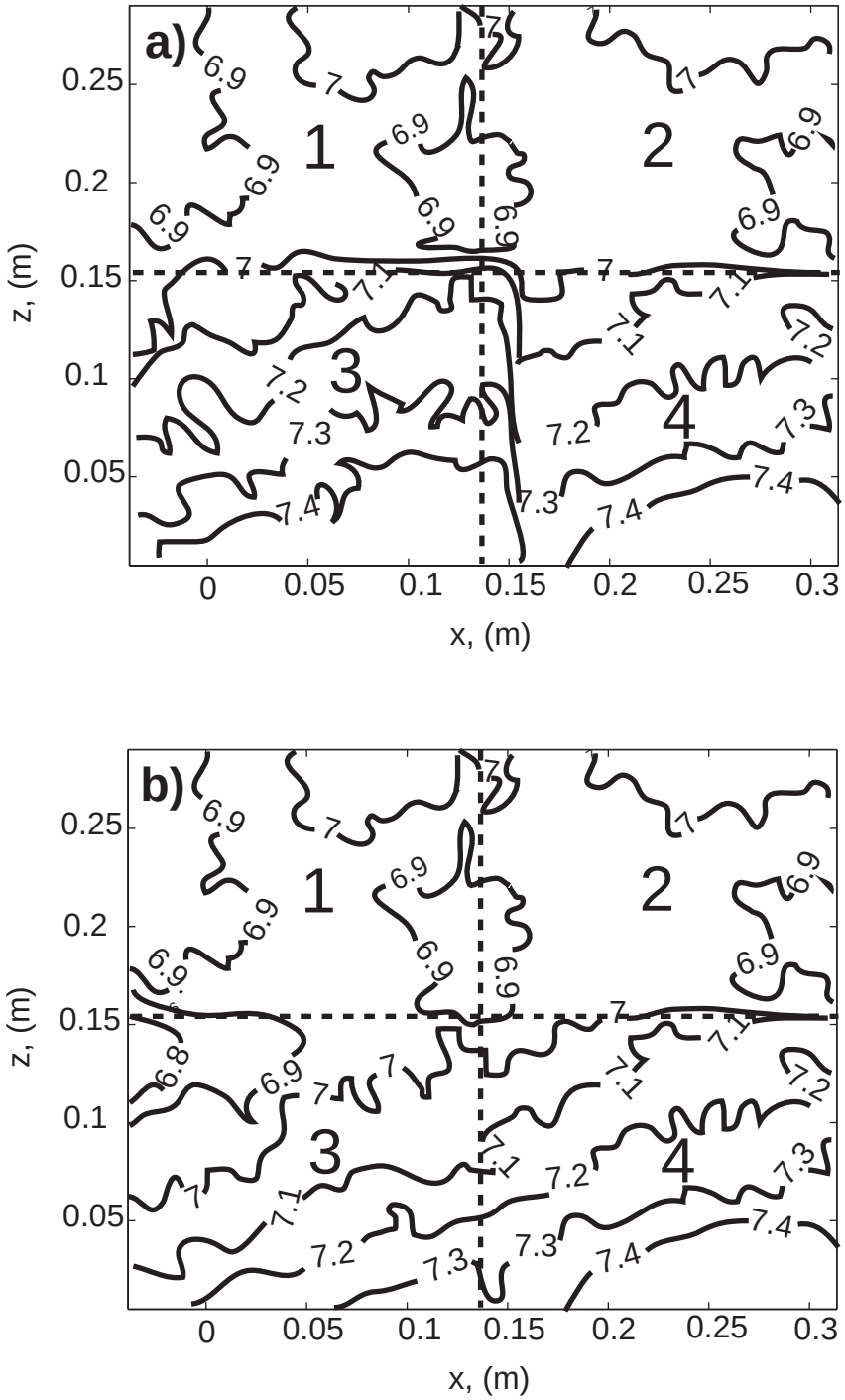

Figure 3.17 The PIV measured free stream wind (ms^{-1}) without a), and with b) the wind speed correction in area 3. Each separate measurement area is indicated.

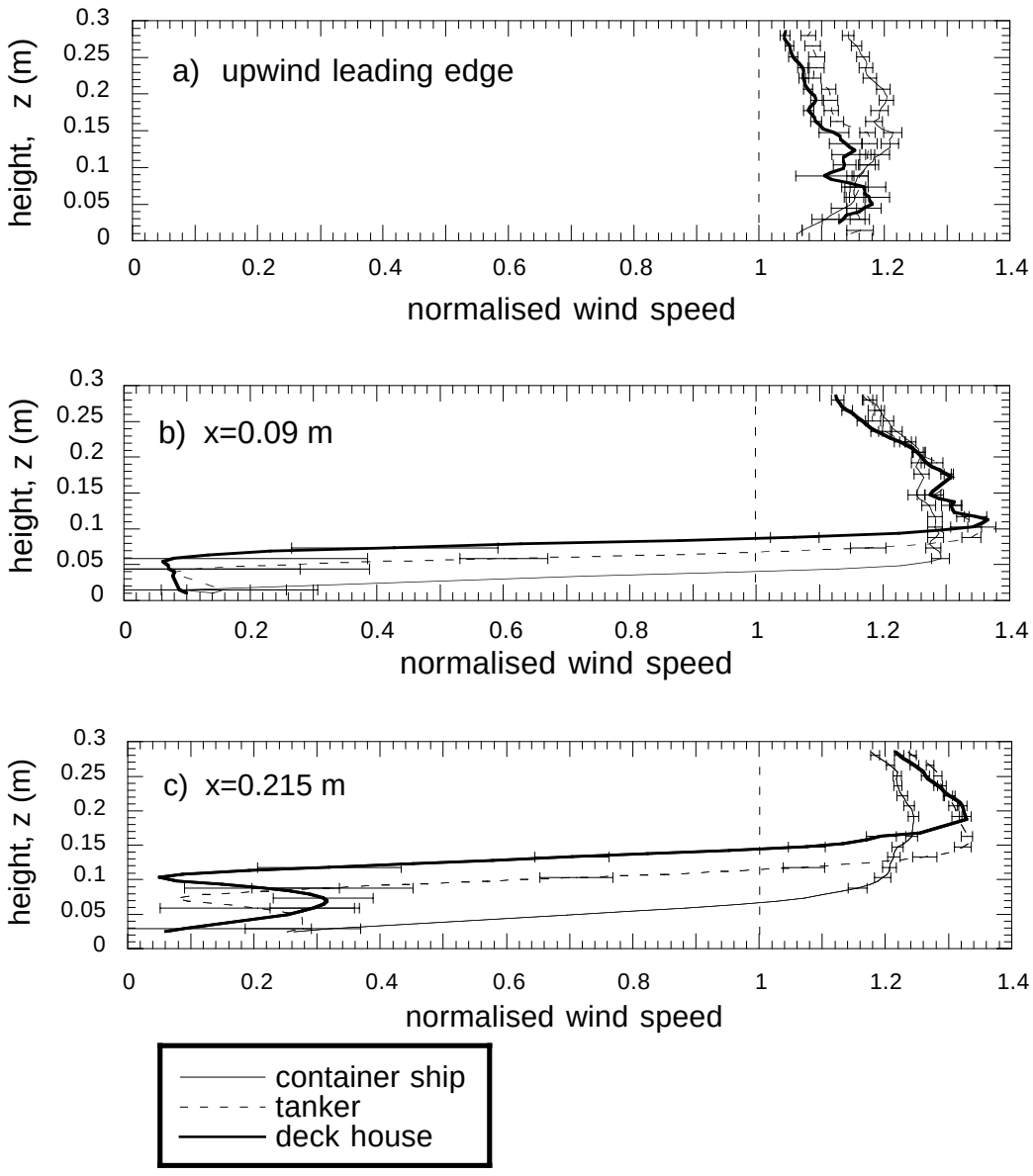

Figure 3.18 Normalised PIV wind speed profiles above the bridge of the three ship geometries.

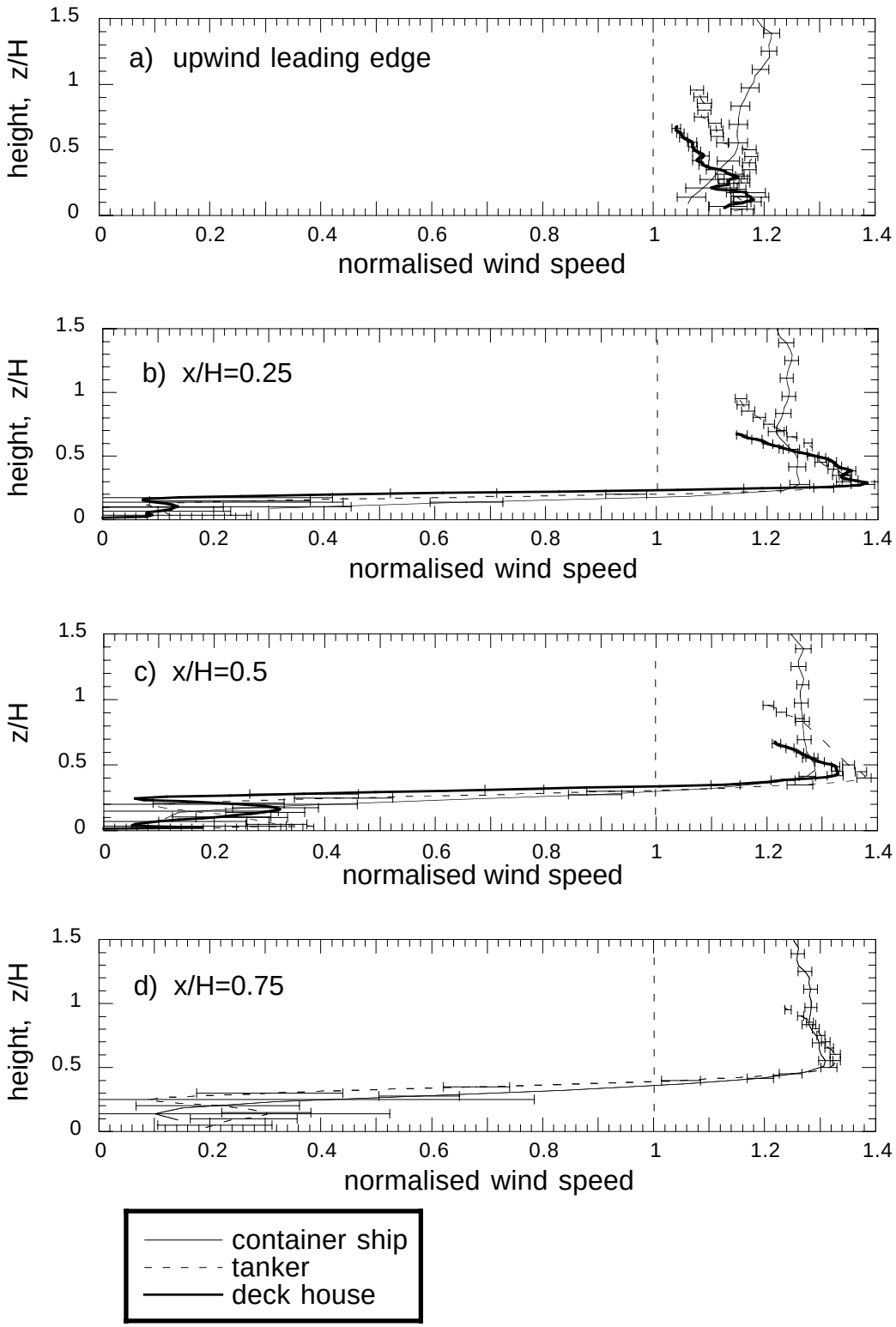

Figure 3.19 As Figure 3.18, but both the heights and the distance aft of the upwind edge are scaled by the step height, H, of the appropriate ship geometry.

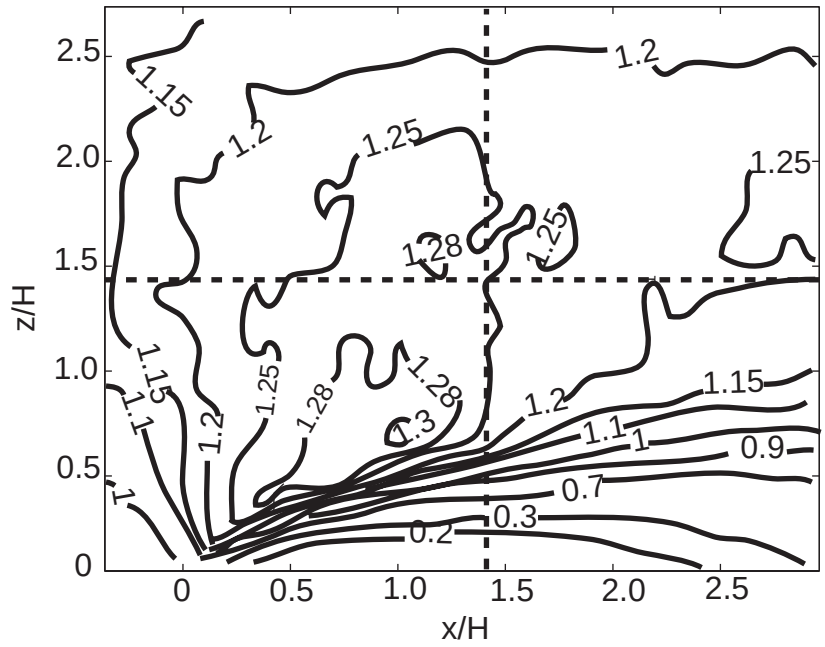

Figure 3.20 The normalised wind speeds above the bridge of the container ship. Distances are scaled by the step height H=0.106 m.

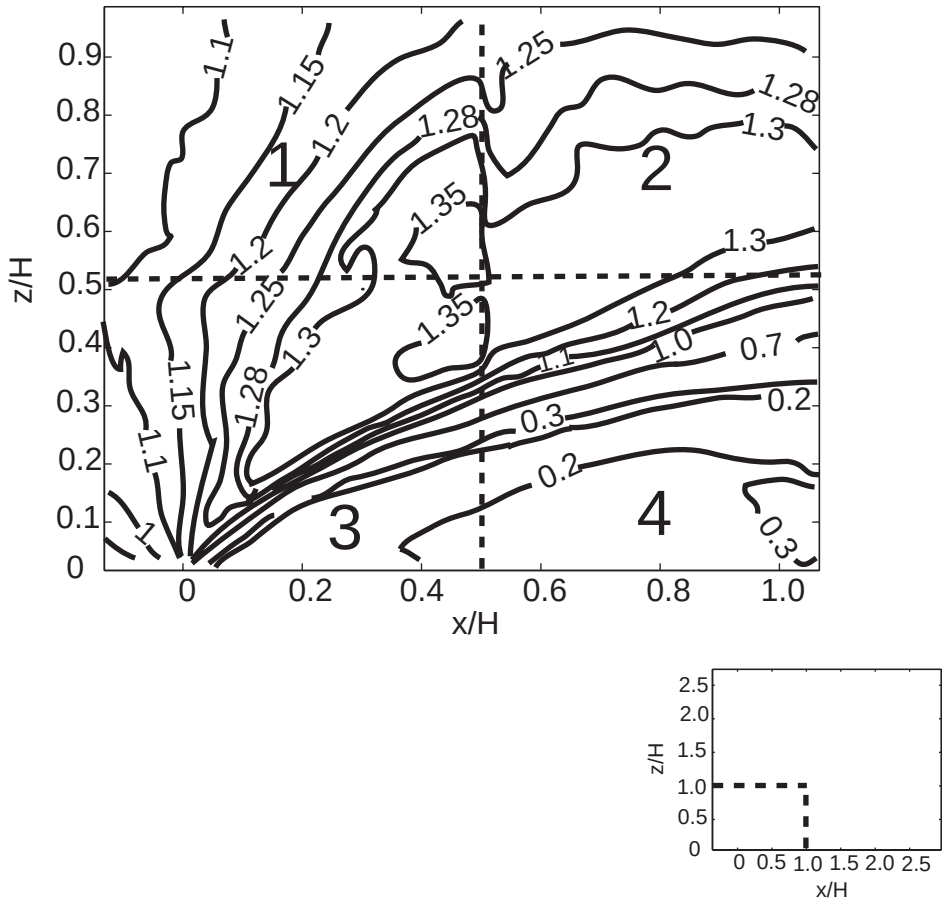

Figure 3.21 Main panel as Figure 3.20, but for the tanker with step height H=0.294 m. Small panel shows the region of Figure 3.20 represented.

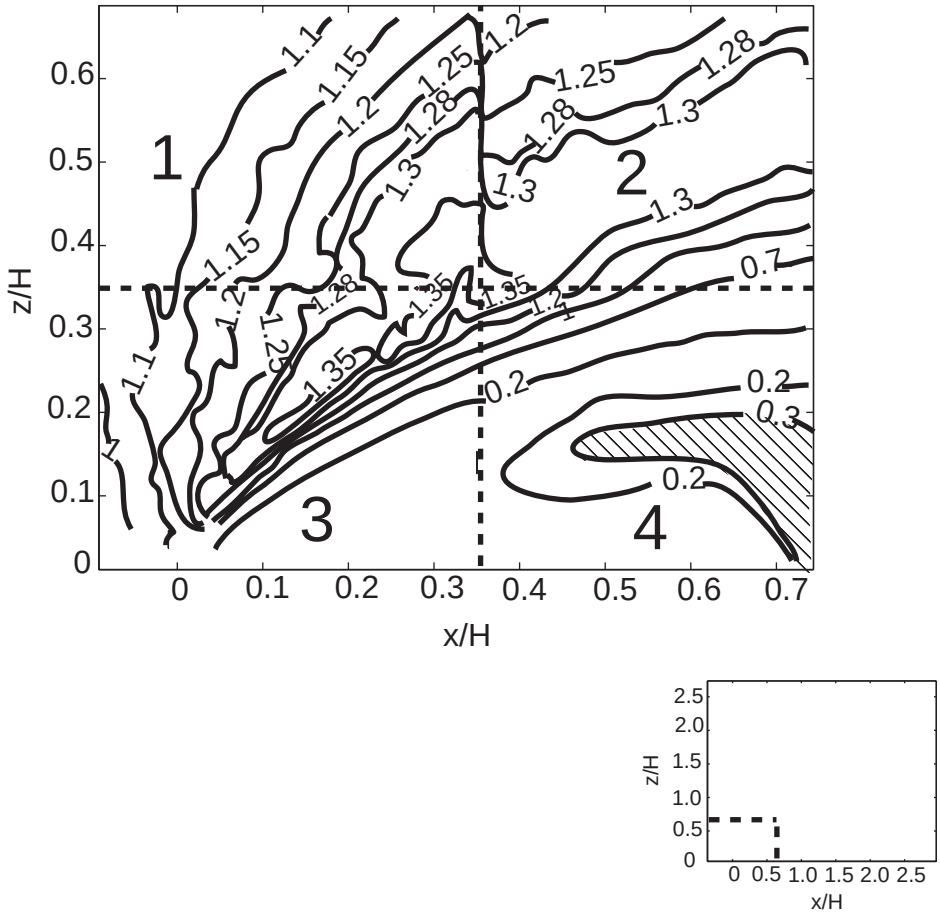

Figure 3.22 Main panel as Figure 3.20, but for the deck house with step height H=0.442 m. Small panel shows the region of Figure 3.20 represented.

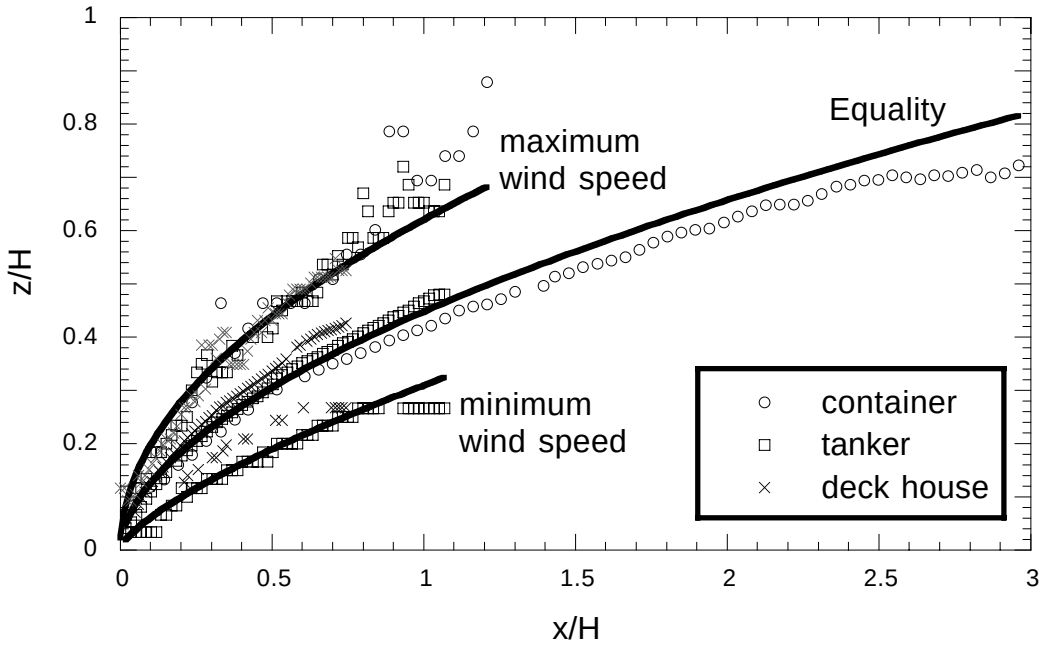

Figure 3.23 Normalised wind speed from the PIV measurements.

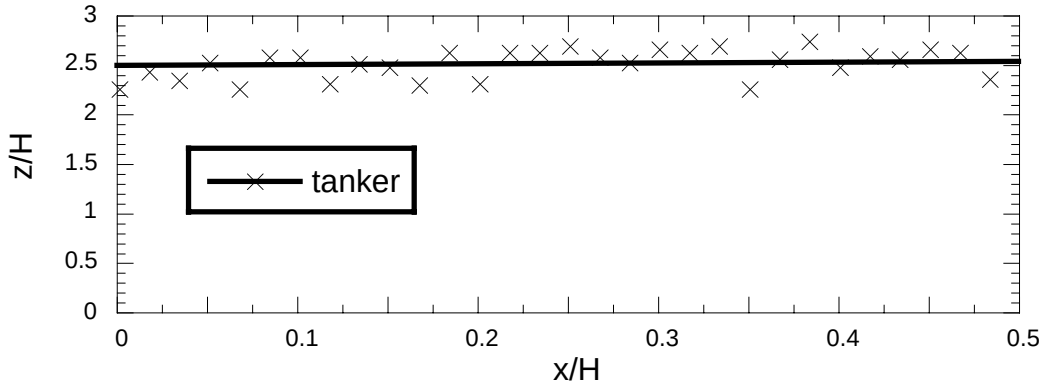

Figure 3.24 The height that the wind speed returns to the free stream, or undisturbed, wind speed.

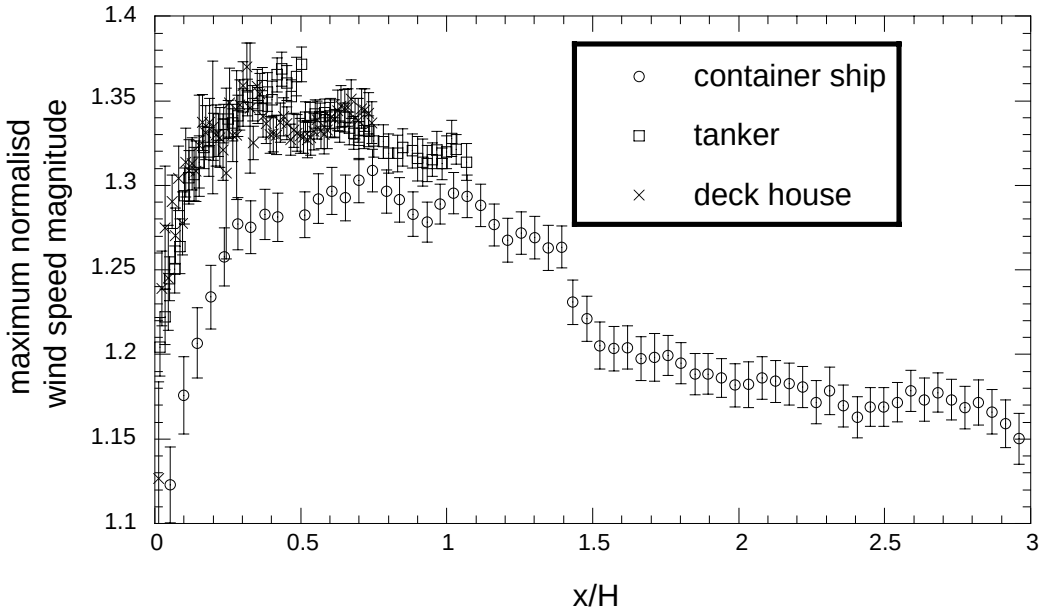

Figure 3.25 The PIV measured wind speed maxima.

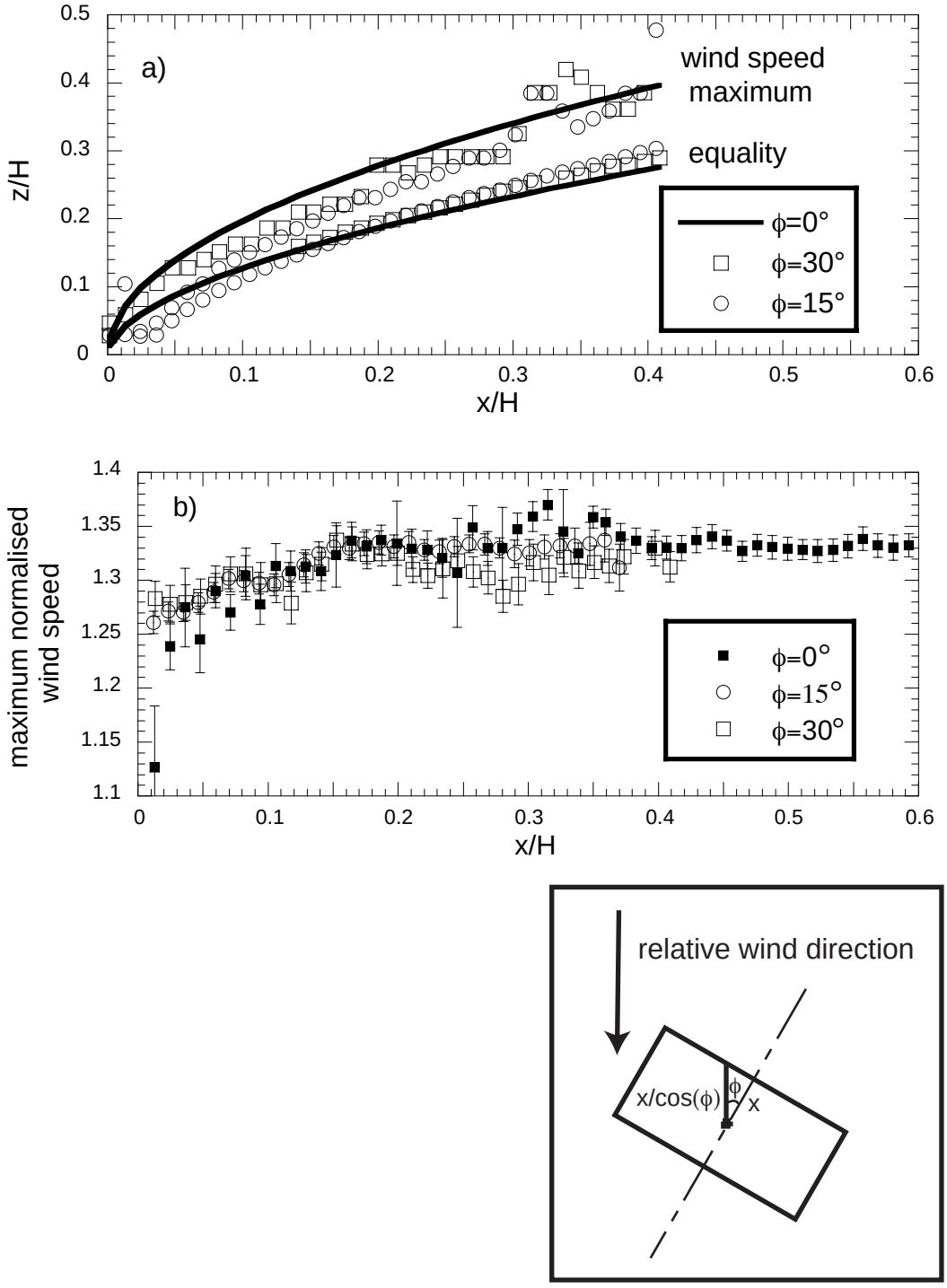

Figure 3.26 The variation in the flow pattern and wind speed magnitude above the deck house block at three different wind directions.

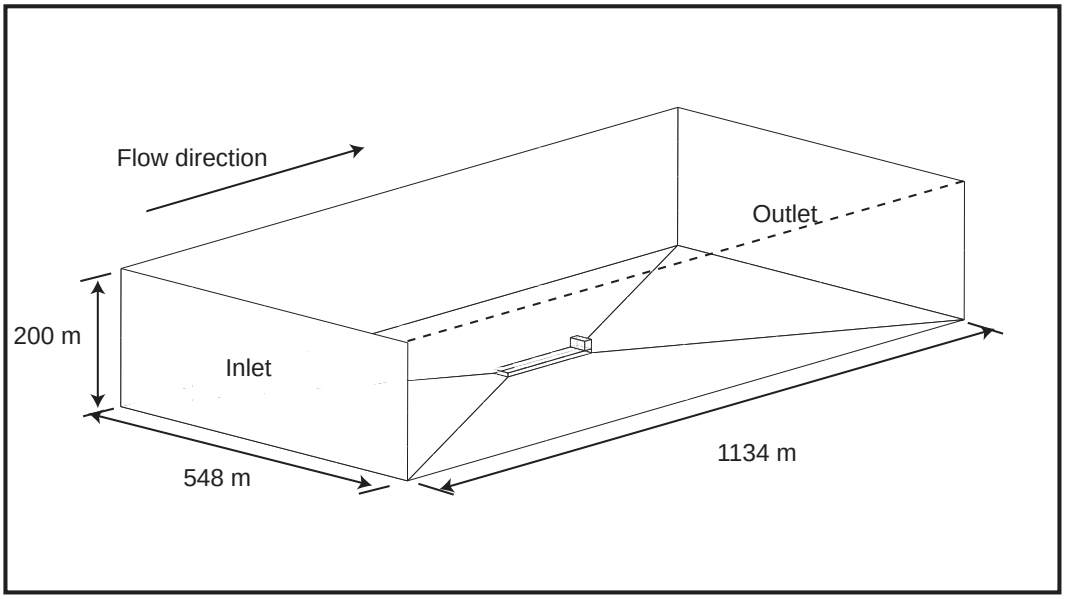

Figure 4.1 The dimensions of the computational domain for the flow over the full-scale generic tanker geometry (LOA=170m). The tanker geometry is located in the centre of the tunnel floor.

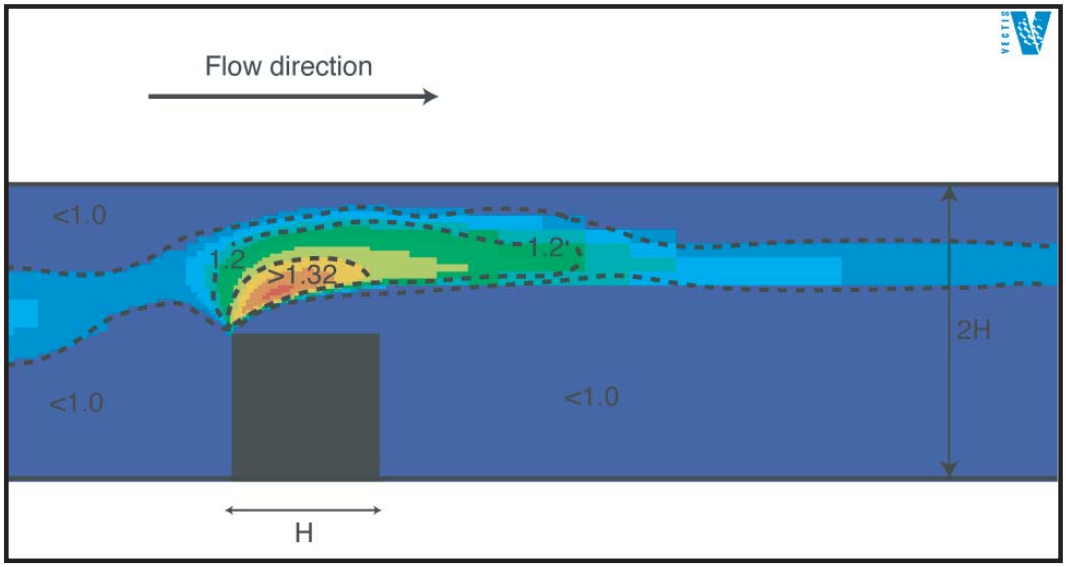

Figure 4.2 The CFD simulation reproducing the flow of air over a cube of height H=0.025 m in the wind tunnel experiment of Martinuzzi and Tropea [64]. The figure shows the velocity field normalised by the inlet wind speed of U=25 ms^{-1}.

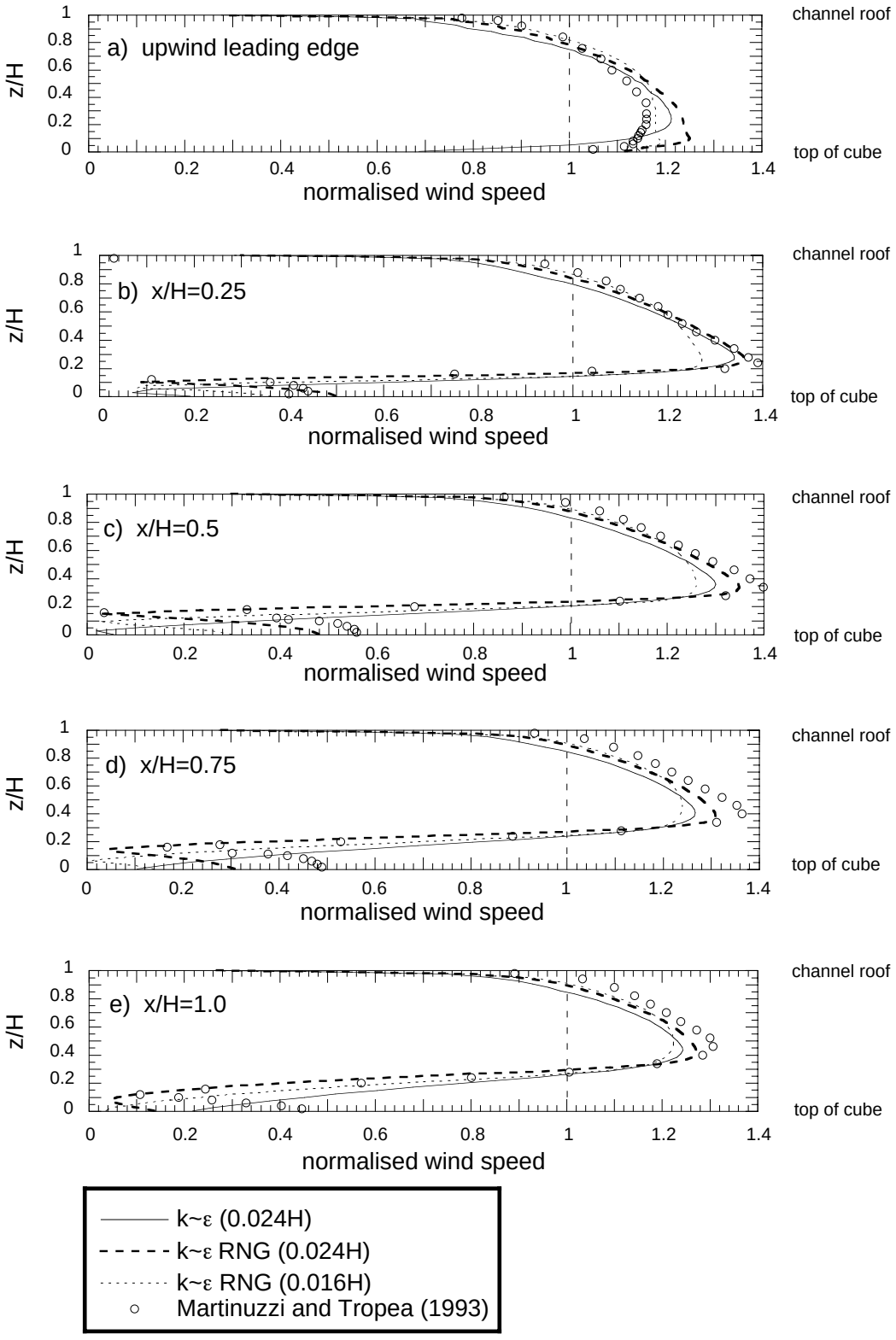

Figure 4.3 Flow above a surface mounted cube in a channel. Vertical profiles of the normalised wind speed above the cube centreline at distances of x/H downstream of the leading edge of the cube are shown.

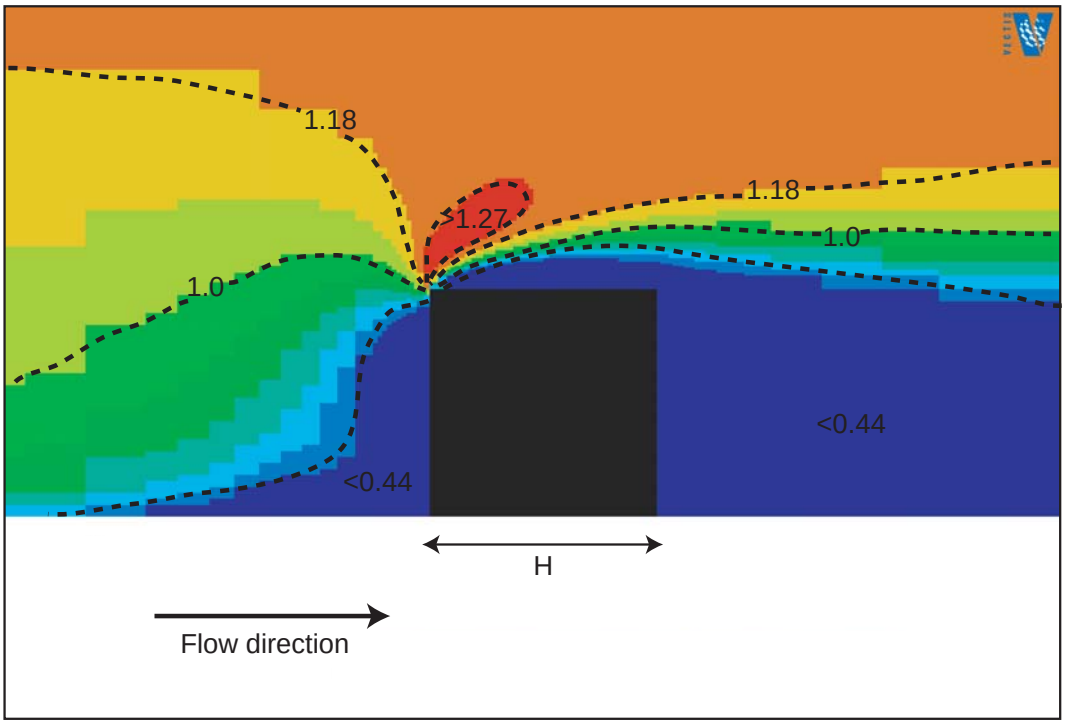

Figure 4.4 The CFD simulation of the flow over a cube of height H=0.2 m in a boundary layer wind tunnel [65]. The figure shows the velocity field normalised by the upstream wind speed, at height H, of 5.4 ms^{-1}.

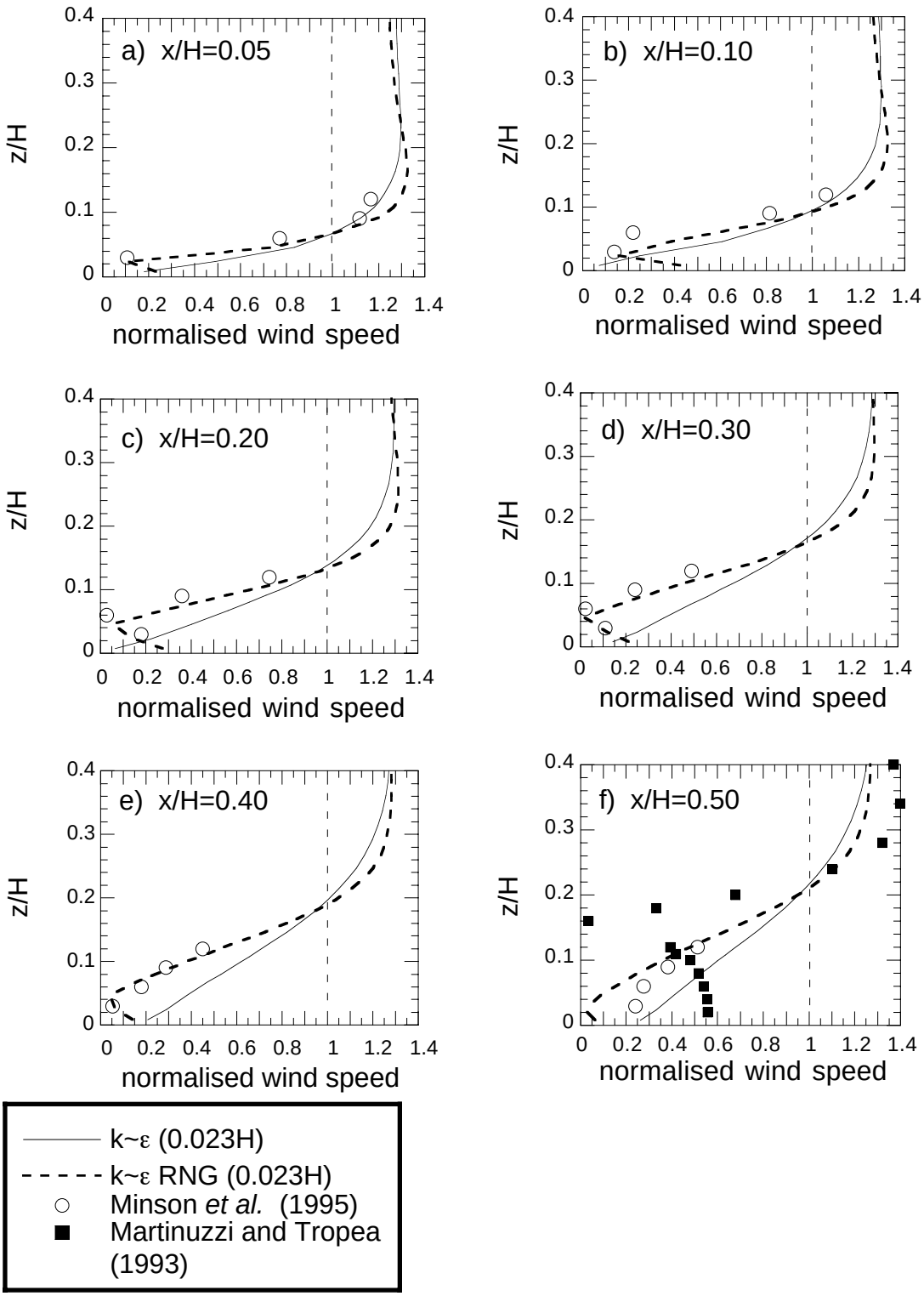

Figure 4.5 Boundary layer flow over a surface mounted cube of height, H=0.2 m. Profiles are shown on the centreline of the cube at distances of x/H downstream of the upwind leading edge.

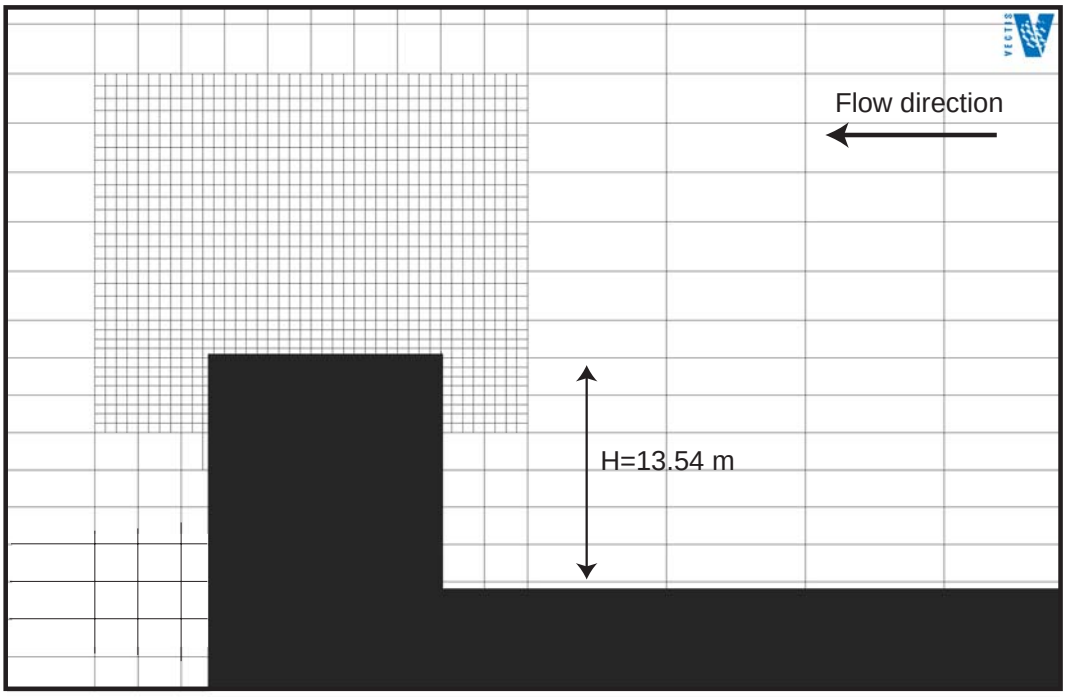

Figure 4.6 A streamwise view of the coarse mesh resolution (RUN A) above the bridge of the tanker.

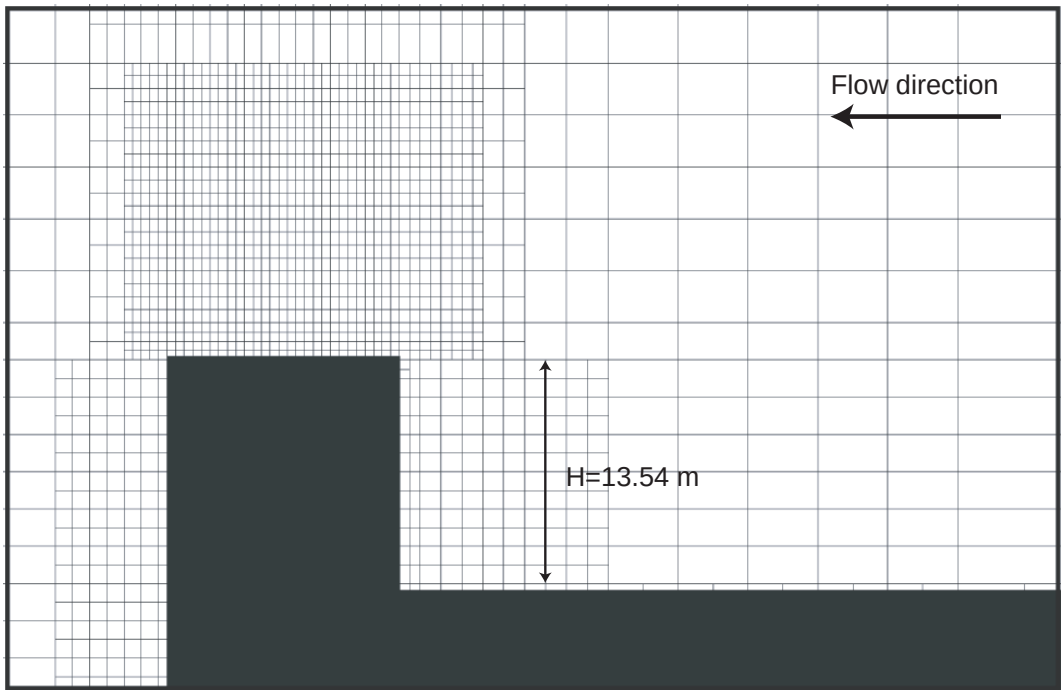

Figure 4.7 A streamwise view of the fine mesh resolution (RUN B) above the bridge of the tanker.

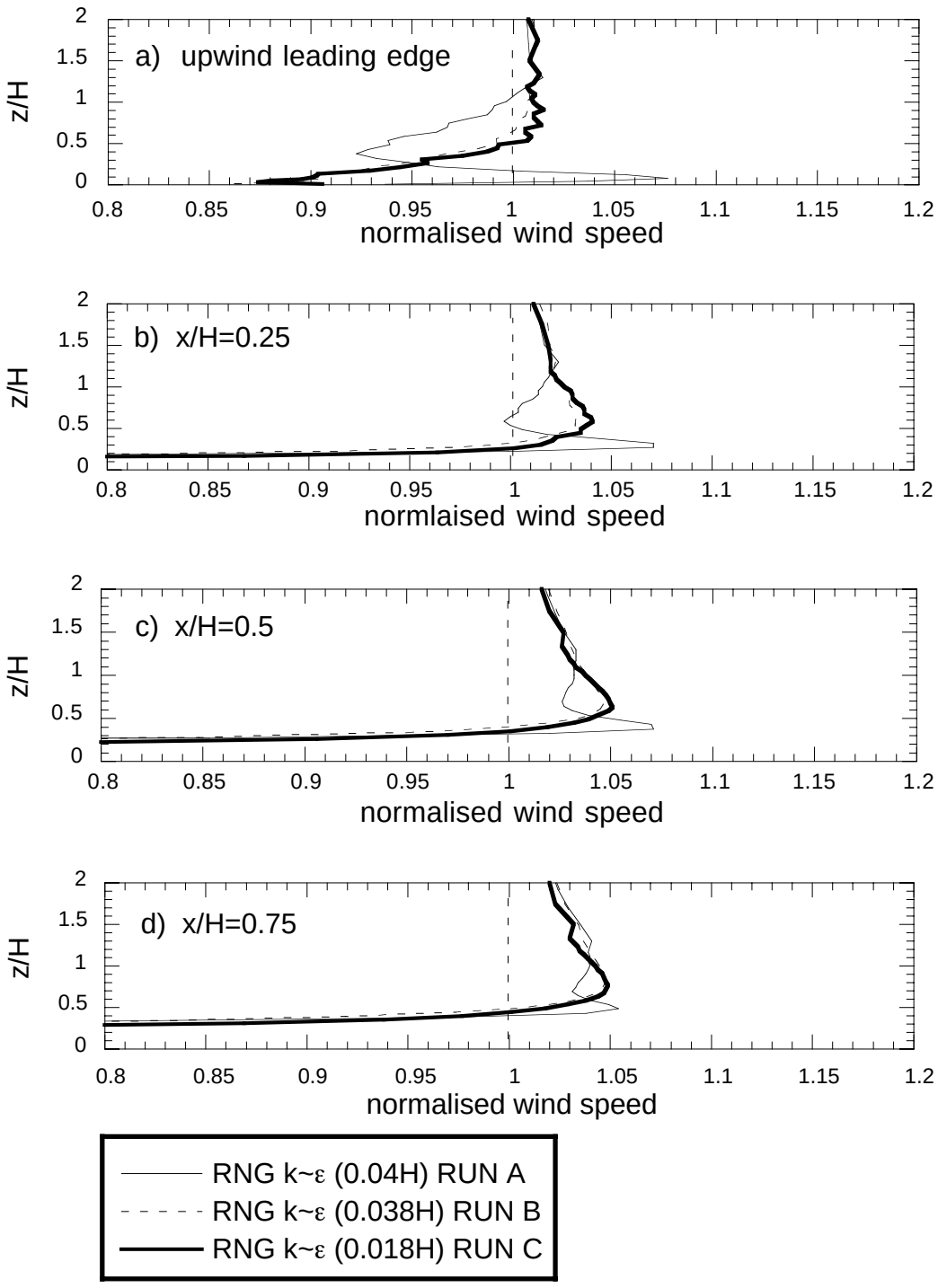

Figure 4.8 Vertical profiles of normalised velocities obtained from three simulations for the 170 m tanker modelled with different mesh densities.

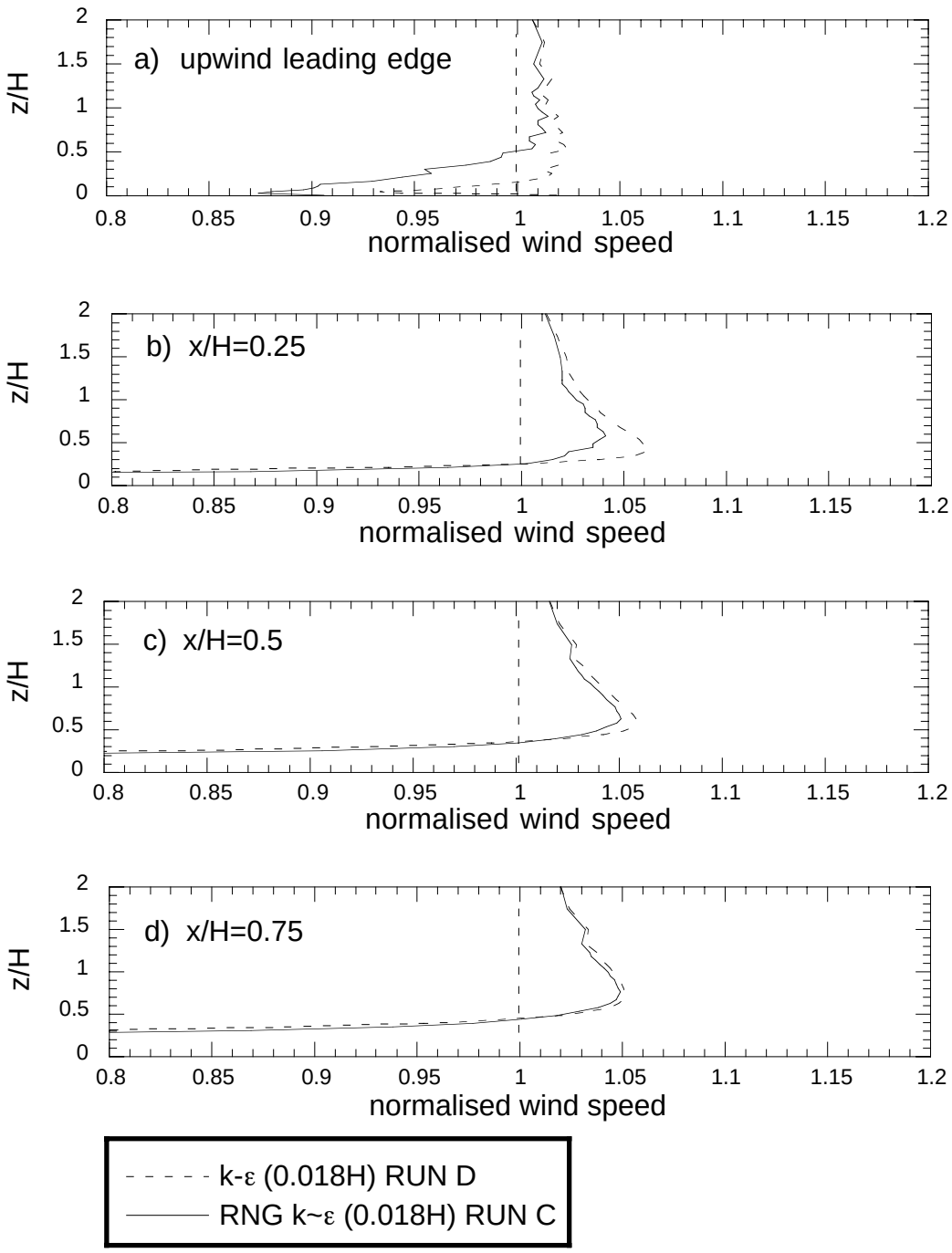

Figure 4.9 Vertical profiles of normalised velocities obtained from two simulations of the 170 m tanker modelled with different turbulence closures.

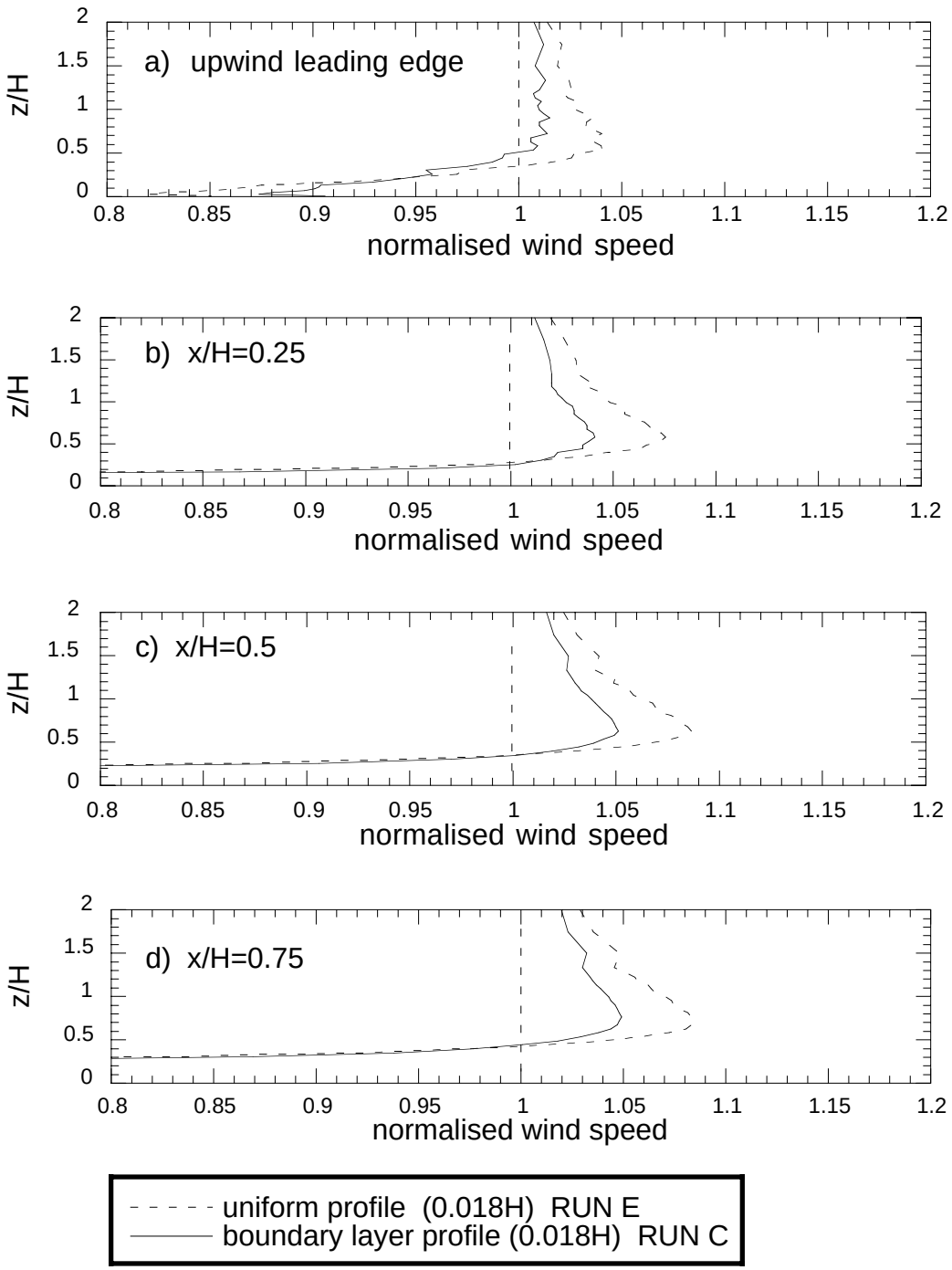

Figure 4.10 Vertical profiles of normalised velocities obtained from two simulations for the 170 m tanker modelled with different inlet wind speed profiles.

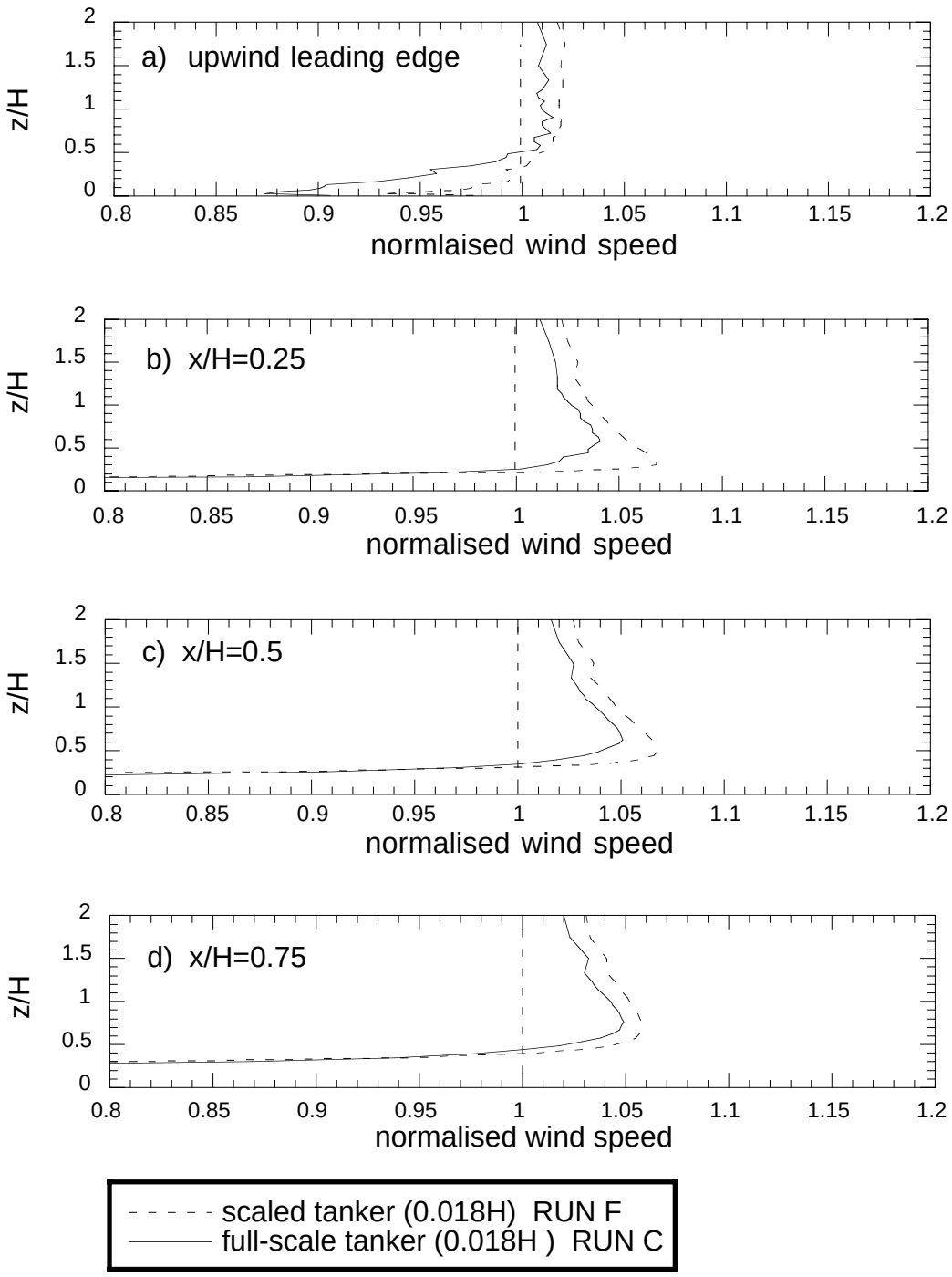

Figure 4.11 Vertical profiles of normalised velocities obtained from two simulations for the 170 m tanker modelled at different geometric scales.

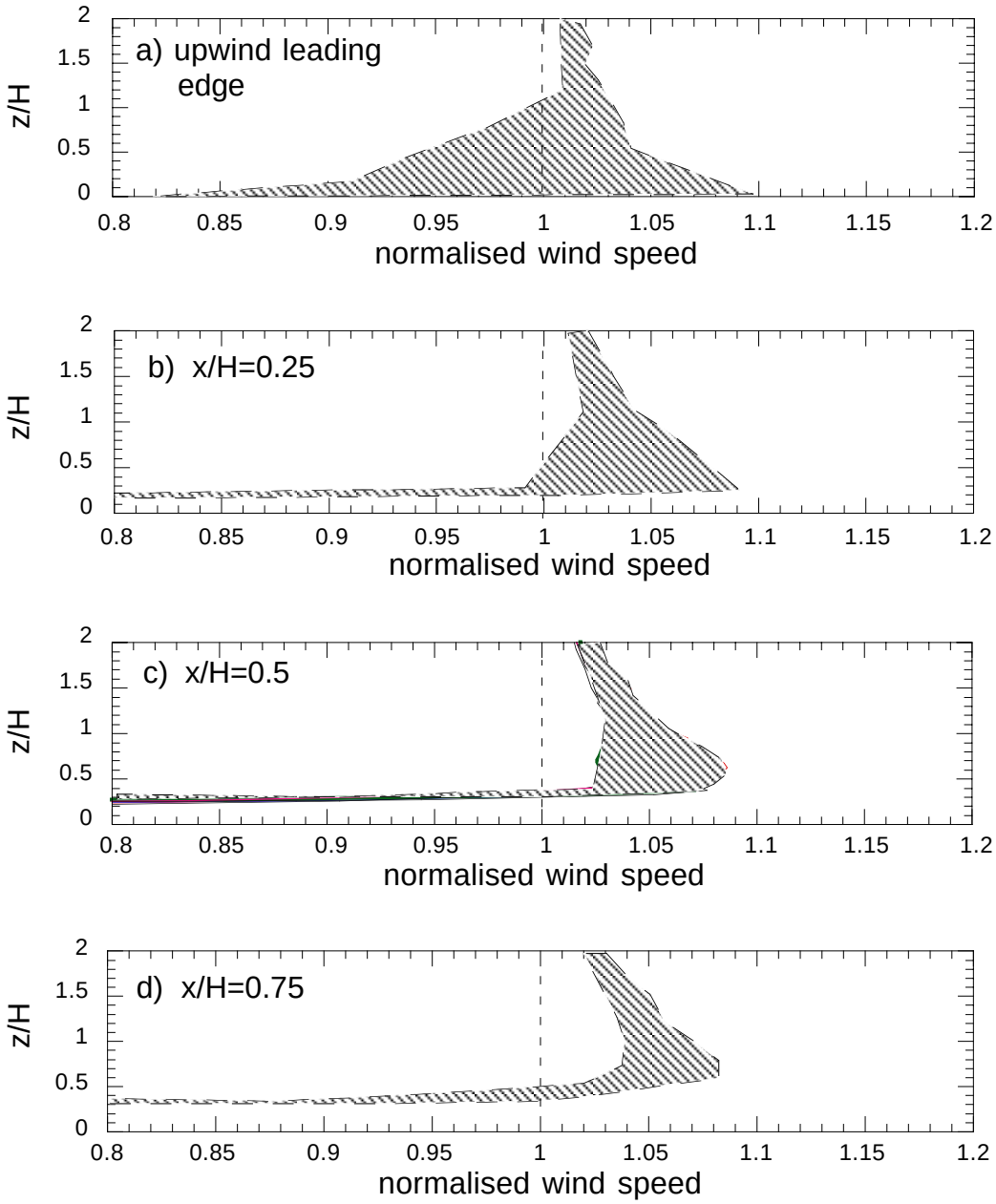

Figure 4.12 The region of variability of the CFD predictions of the flow above the bridge of the full-scale tanker geometry.

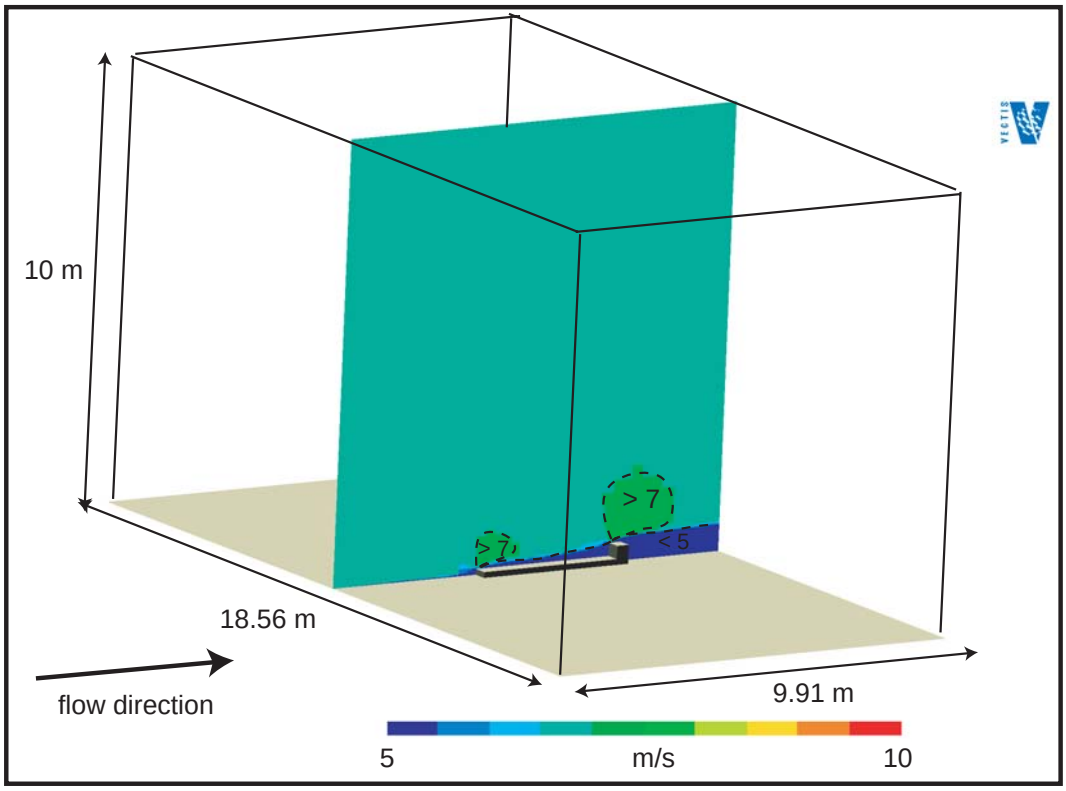

Figure 4.13 The CFD simulation of a free surface flow over the tanker. The velocity field in the centre of the wind tunnel is displayed.

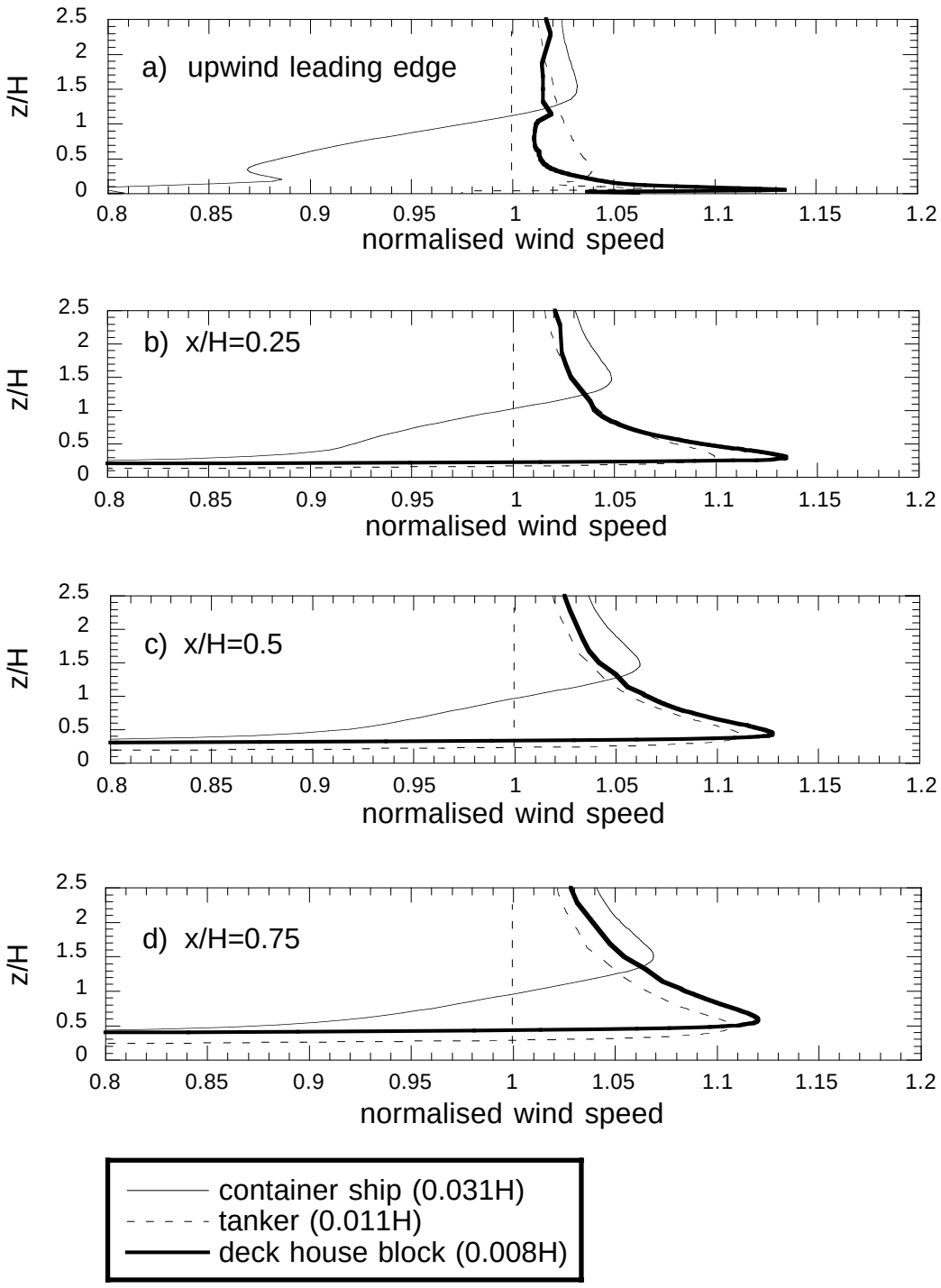

Figure 4.14 CFD predicted vertical profiles of normalised velocities obtained from the wind tunnel scale models.

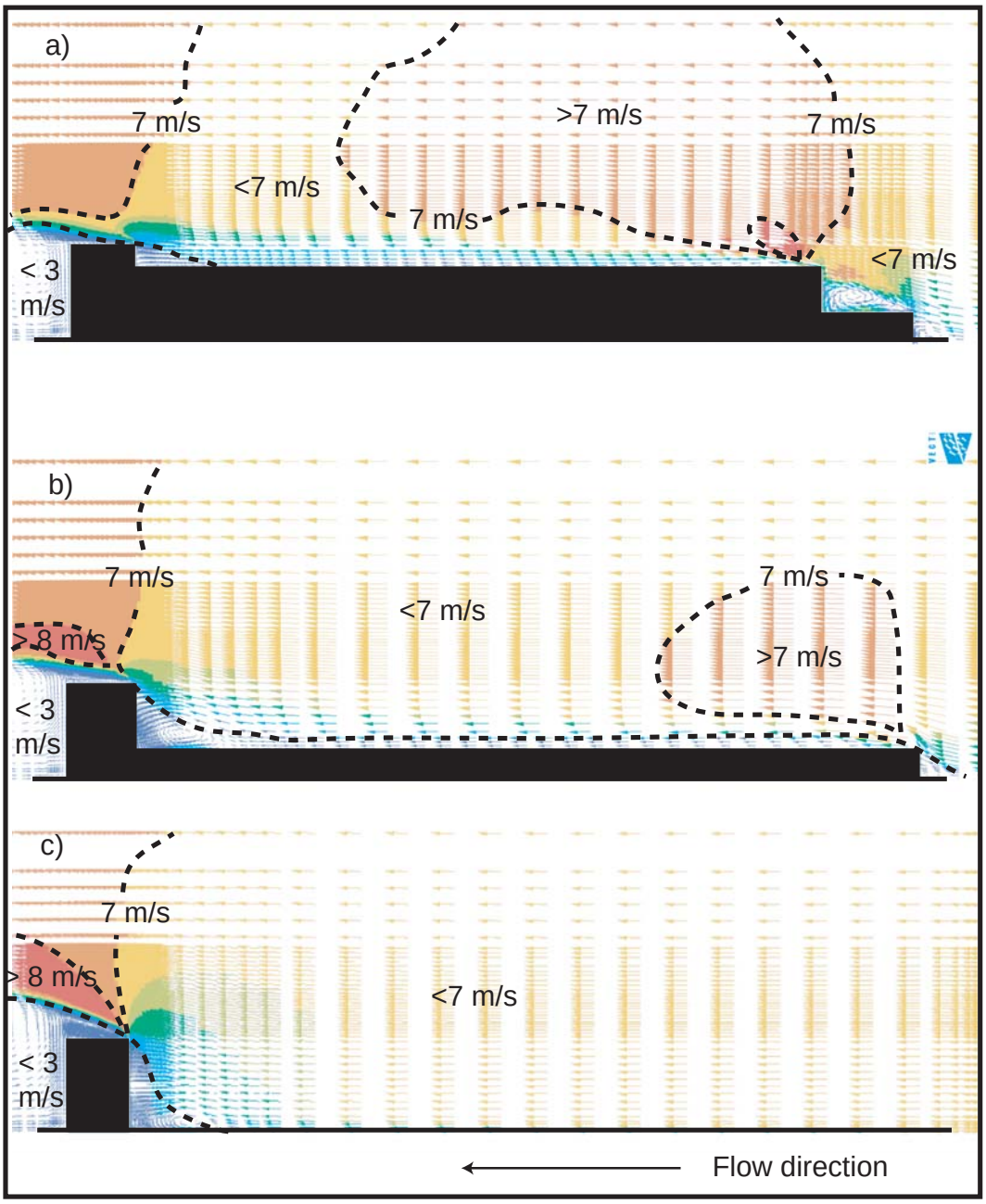

Figure 4.15 The CFD predicted velocity on the ships centreline over the scaled geometries of the (a) container ship, (b) tanker and (c) deck house block.

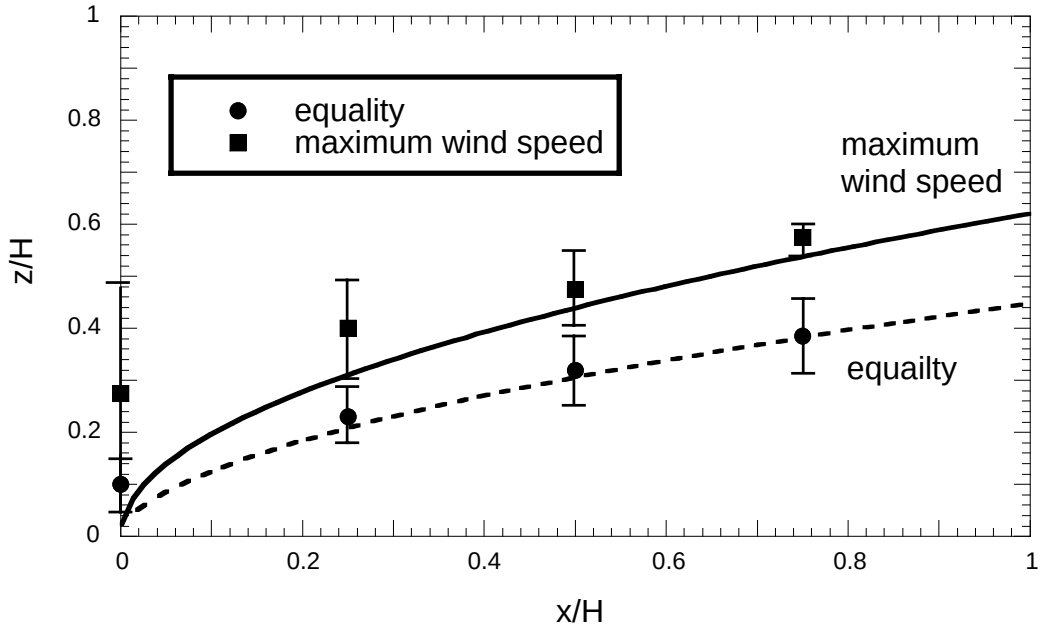

Figure 4.16 Flow above the bridge of the scale geometries from CFD simulations (symbols). The lines indicate the fits to experimental PIV data as given by Equations 3.2 and 3.3.

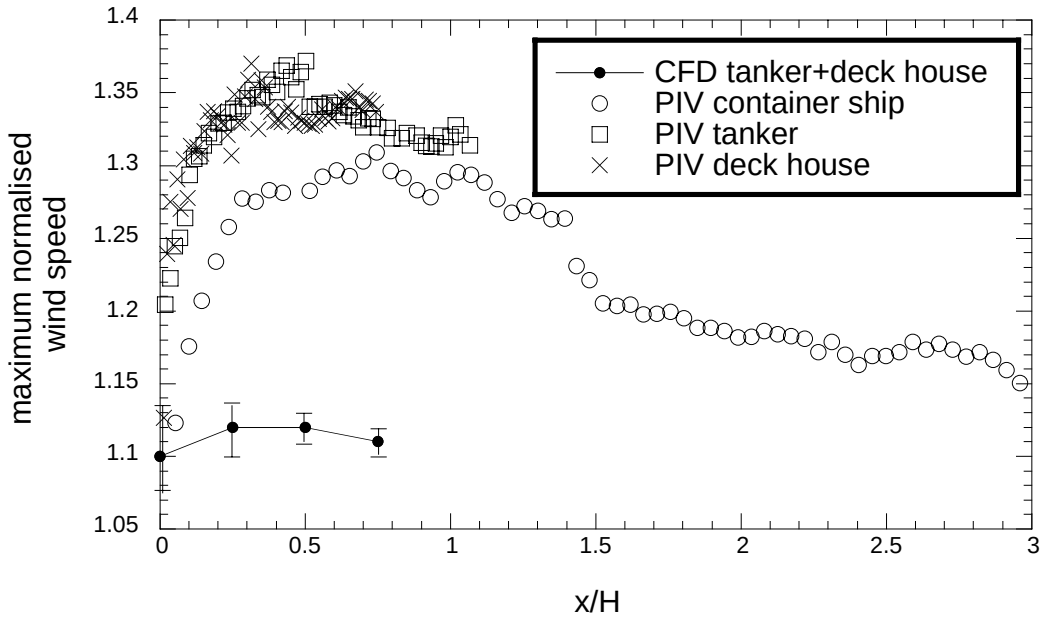

Figure 4.17 The CFD predicted wind speed maximum from each of the three scale geometries compared with the PIV measurements.

Figure 5.1 A photograph of the *RRS Charles Darwin* (reproduced with permission from NERC Research Ship Unit, Southampton, UK).

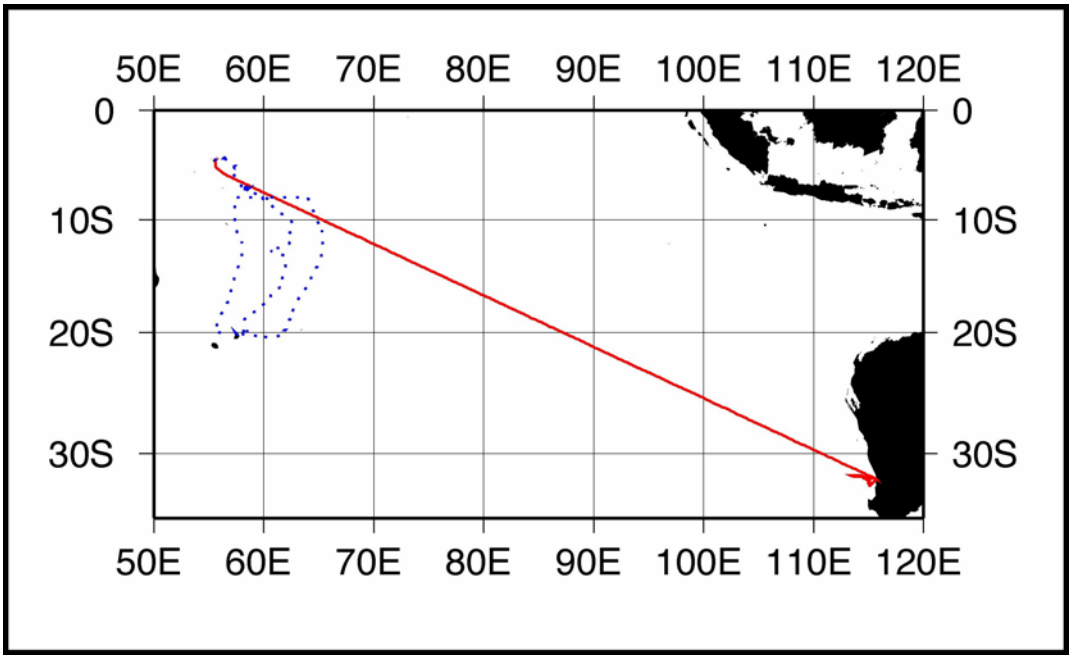

Figure 5.2 The ship track for the *RRS Charles Darwin* cruises CD140 (solid line) and CD141 (dotted line).

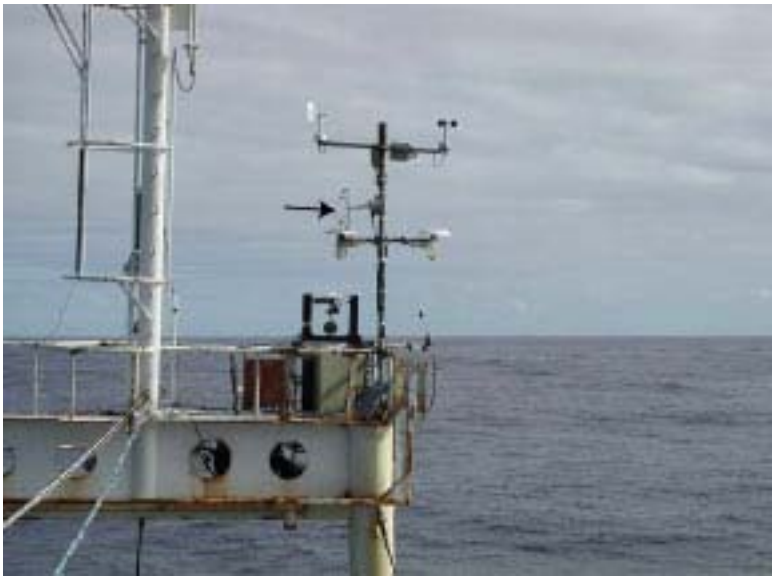

Figure 5.3 The foremast of the *RRS Charles Darwin*, showing the HS sonic anemometer (indicated by the arrow) on the starboard side of the platform.

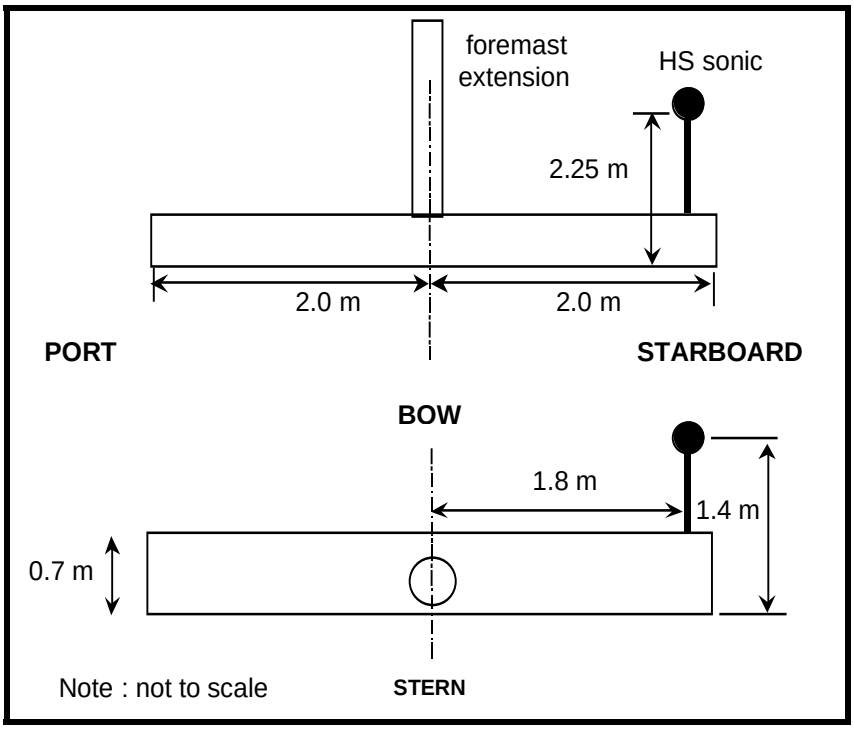

Figure 5.4 The position of the HS sonic anemometer on the foremast platform of the *RRS Charles Darwin* looking from astern (top), and above (bottom).

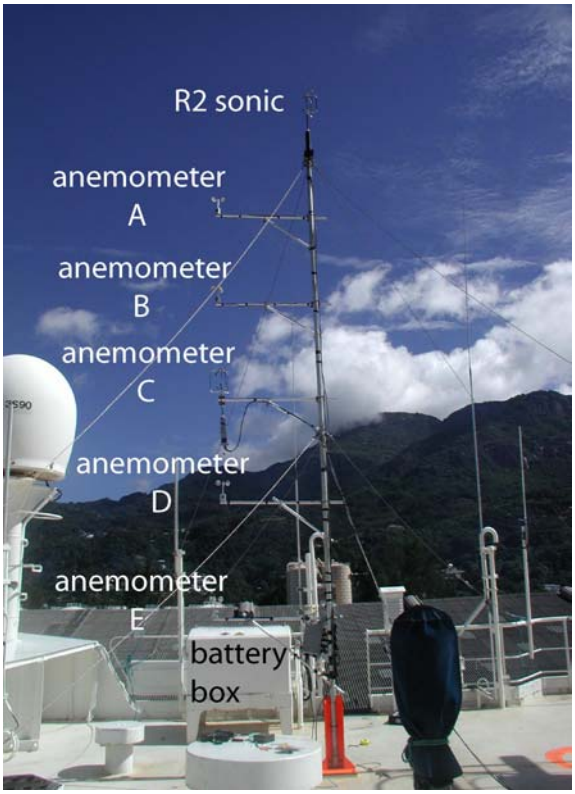

Figure 5.5 The temporary mast above the bridge of the *RRS Charles Darwin*, looking towards the starboard side.

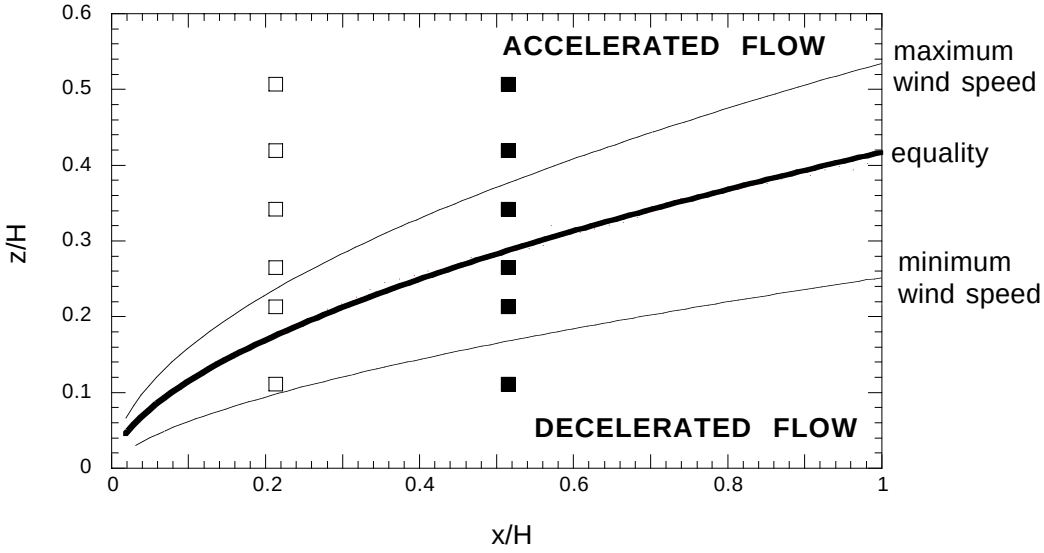

Figure 5.6 The scaled positions of the anemometer locations for flows over the port beam (filled squares) and starboard beam (open squares). The positions of the line of equality (thick line), the maximum and minimum wind speeds (thin lines) are overlaid.

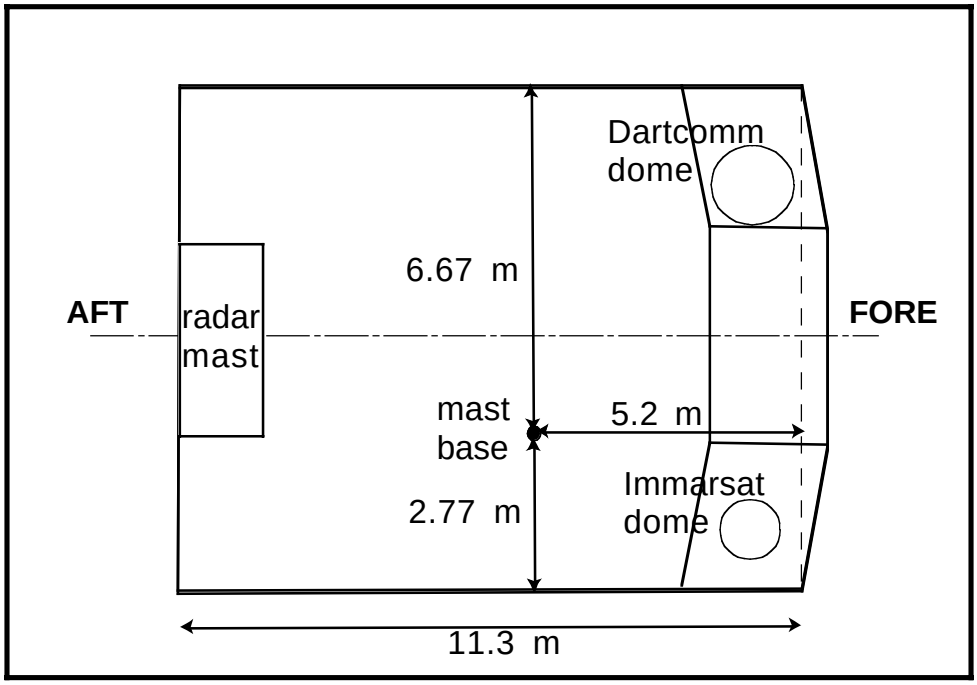

Figure 5.7 Schematic plan view of the position of the mast above the bridge of the *RRS Charles Darwin*.

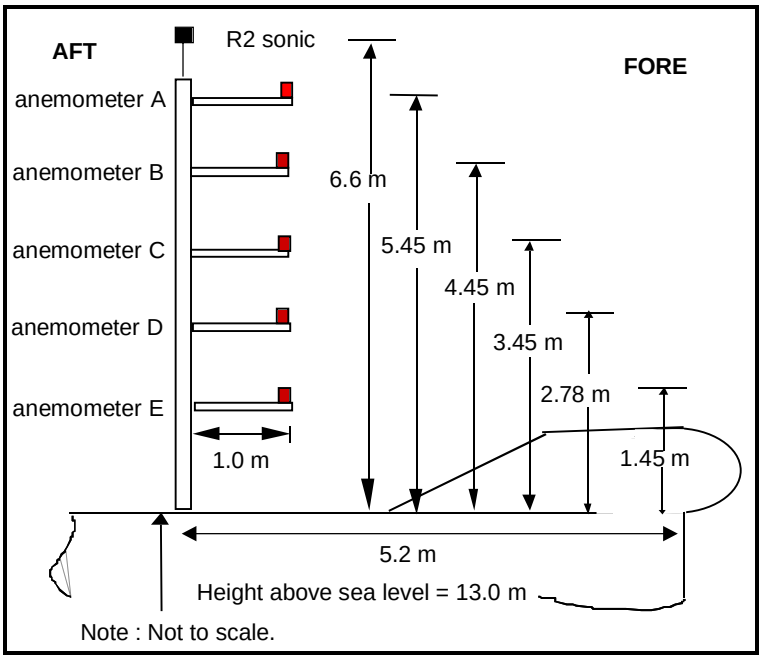

Figure 5.8 Schematic side view of the Vector anemometers on the temporary 6 m mast above the bridge of the *RRS Charles Darwin* cruise.

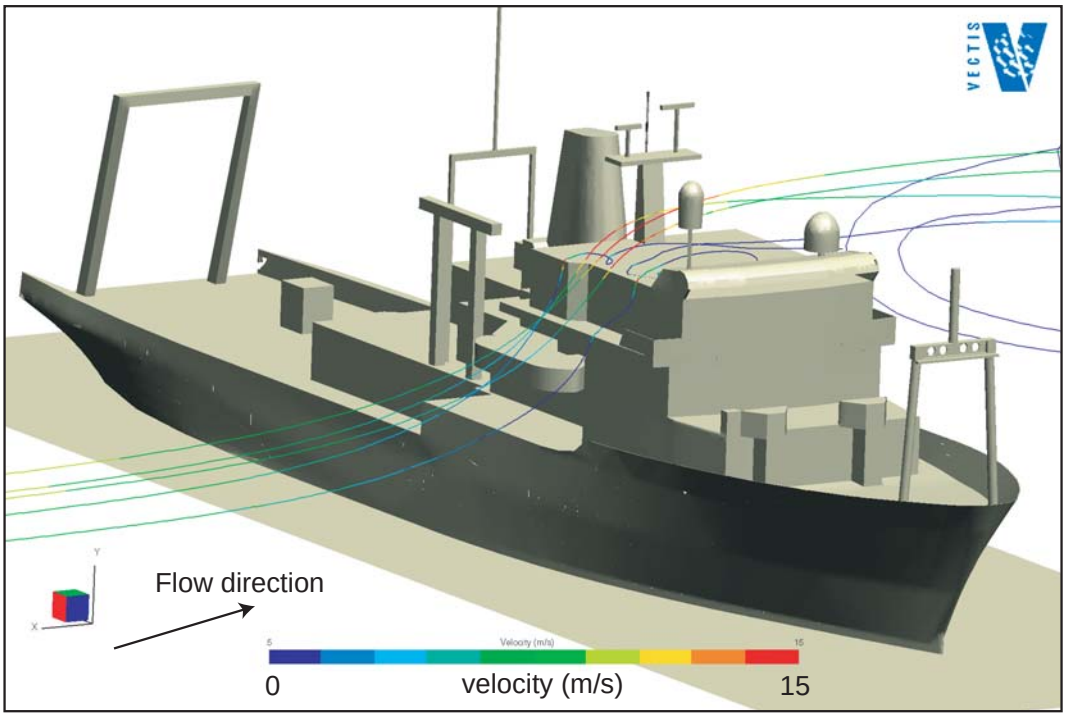

Figure 5.9 The CFD model of the air flow over the starboard beam of the *RRS Charles Darwin*. Streamlines showing the path of the flow of air over the bridge top are overlaid.

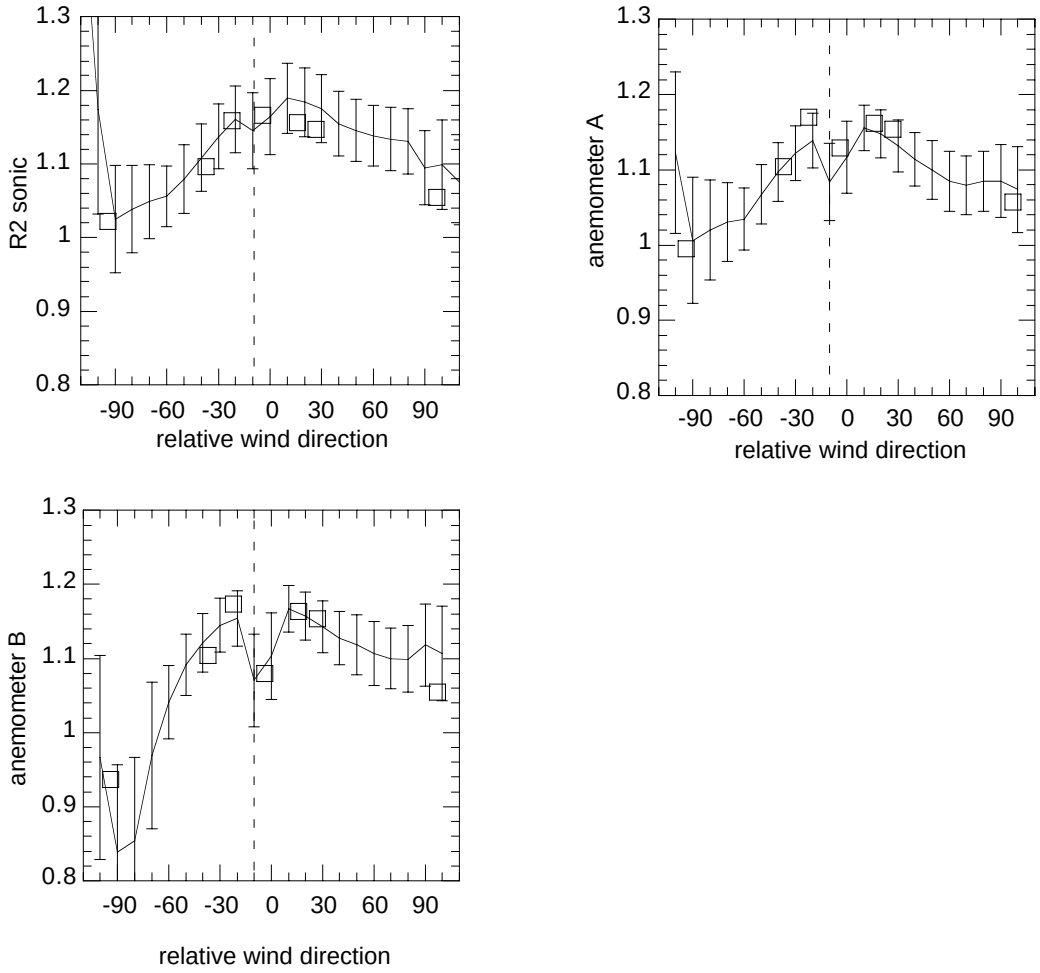

Figure 5.10 Relative wind speed ratios (expressed as a fraction of the wind speed measured by the HS sonic on the foremast) for *in situ* wind speed measurements made on the *RRS Charles Darwin* (lines) and for the CFD models (open squares).

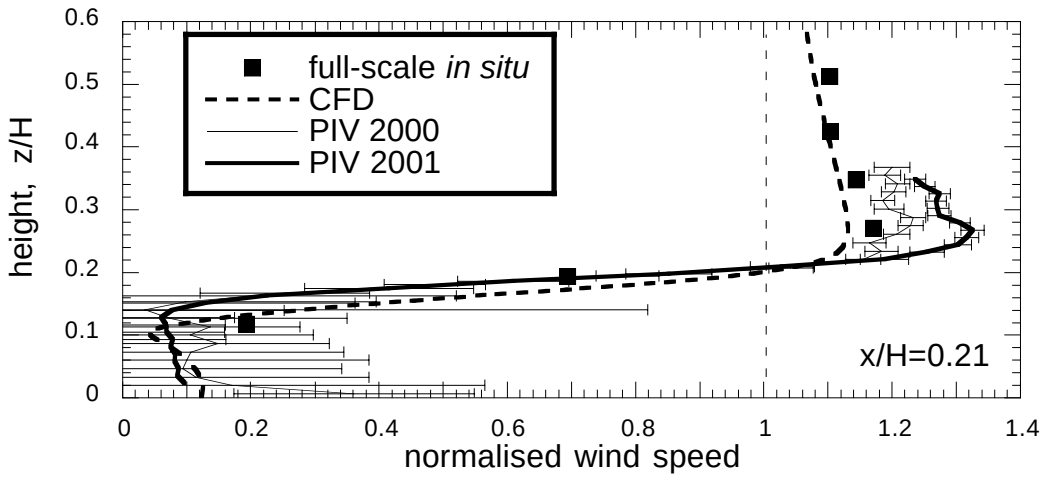

Figure 5.11 Normalised wind speed profiles compared to the *in situ* results from the anemometers for an air flow over the starboard beam.

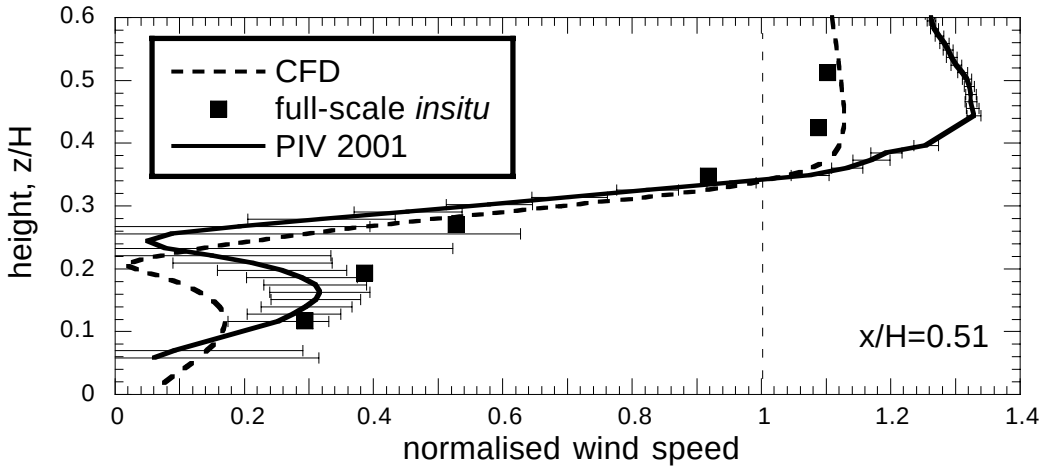

Figure 5.12 As Figure 5.11, but for an air flow over the port beam.

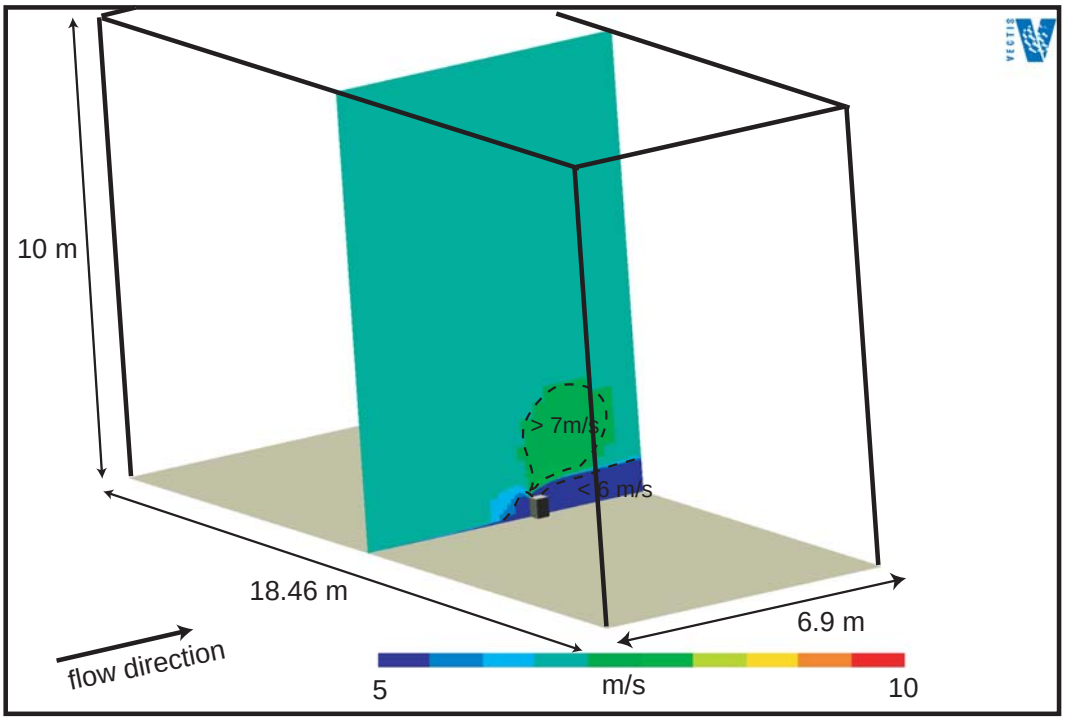

Figure 5.13 The CFD simulation of a free surface flow over the deck house block. The velocity field in the centre of the wind tunnel is displayed.

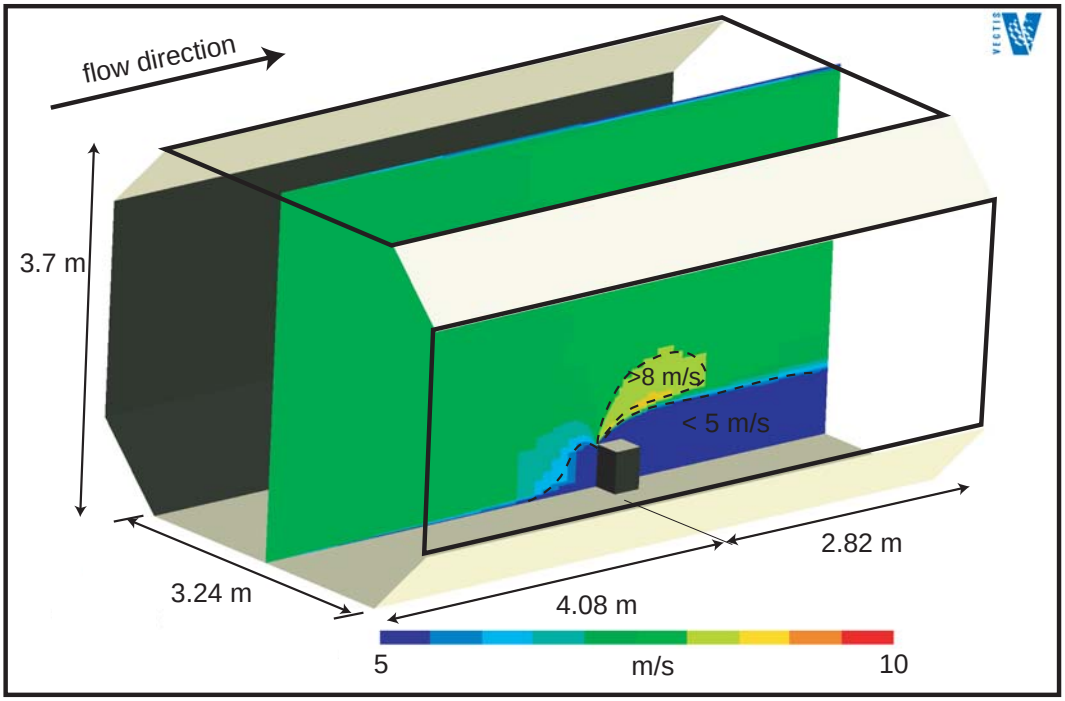

Figure 5.14 The CFD simulation of the flow over the deck house block, enclosed in the low speed section of the wind tunnel. The velocity field in the centre of the wind tunnel is displayed.

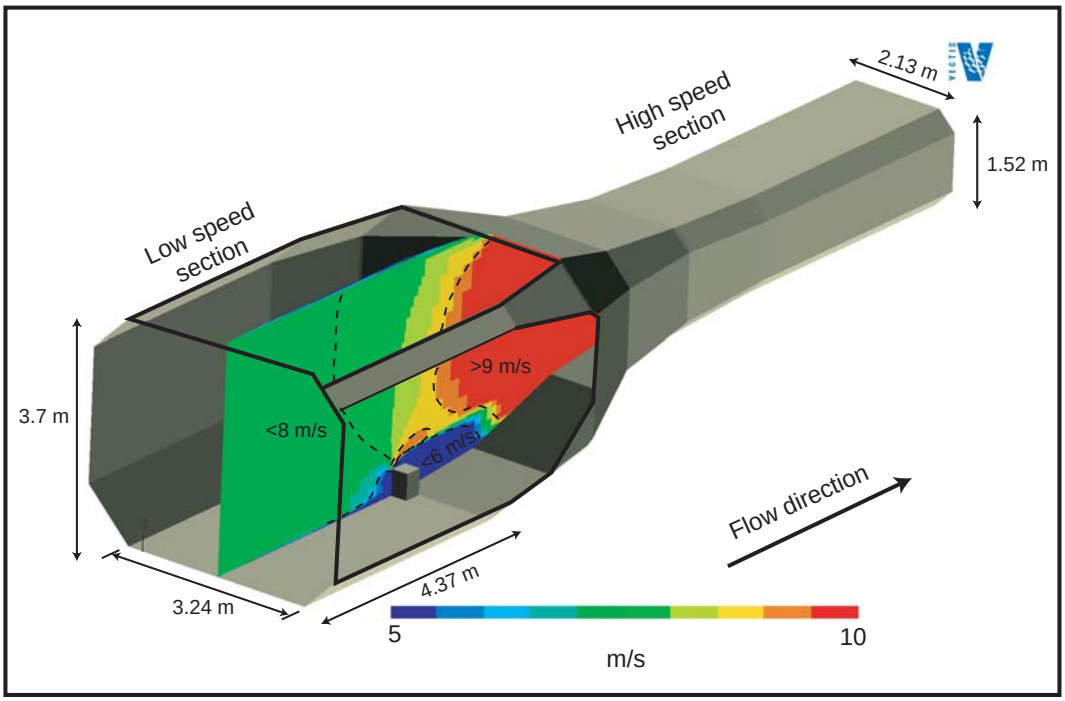

Figure 5.15 The CFD simulation of the airflow through the Southampton University wind tunnel, including the contraction. The velocity field in the centre of the wind tunnel is displayed.

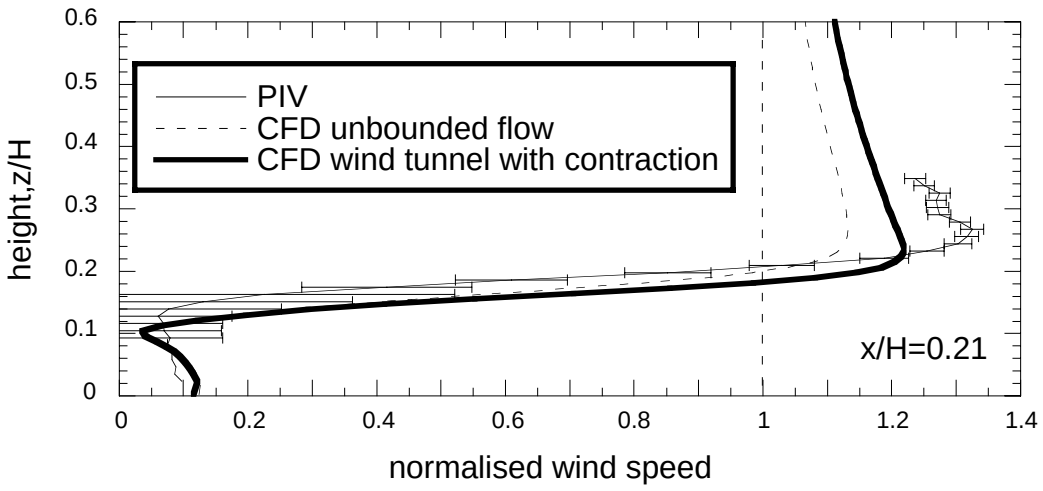

Figure 5.16 CFD simulations and PIV results of the flow above the deck house block. The error bars indicate the standard error of the data.

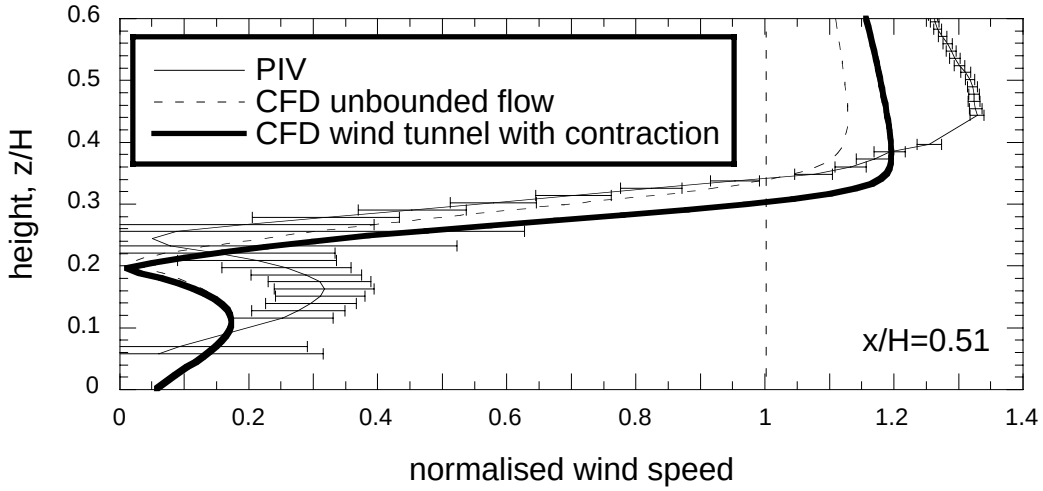

Figure 5.17 As figure 5.16, but at a distance of x/H=0.51 from the upwind leading edge.

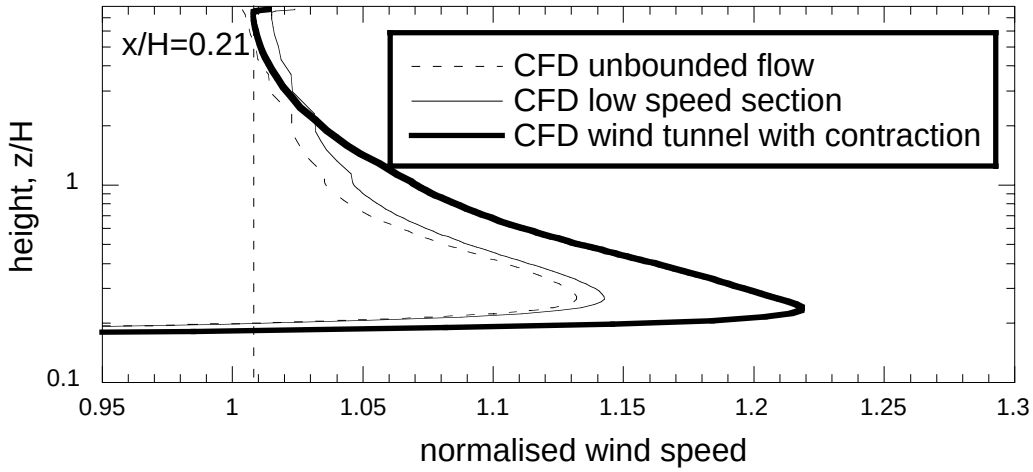

Figure 5.18 CFD simulations of the normalised wind speed profiles above the deck house block.

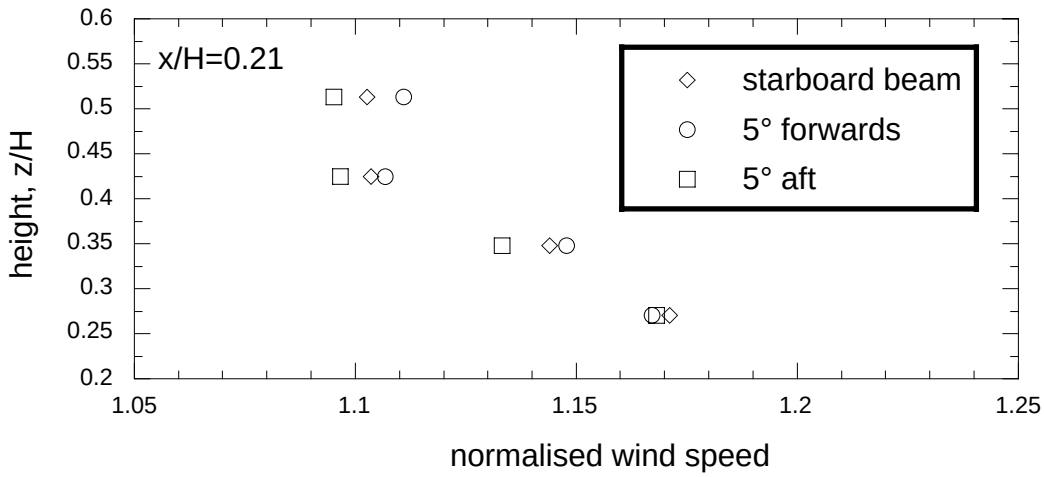

Figure 5.19 Normalised *in situ* wind speed profiles selected at for flows 5° fore and aft of the starboard beam, compared to beam on flow.

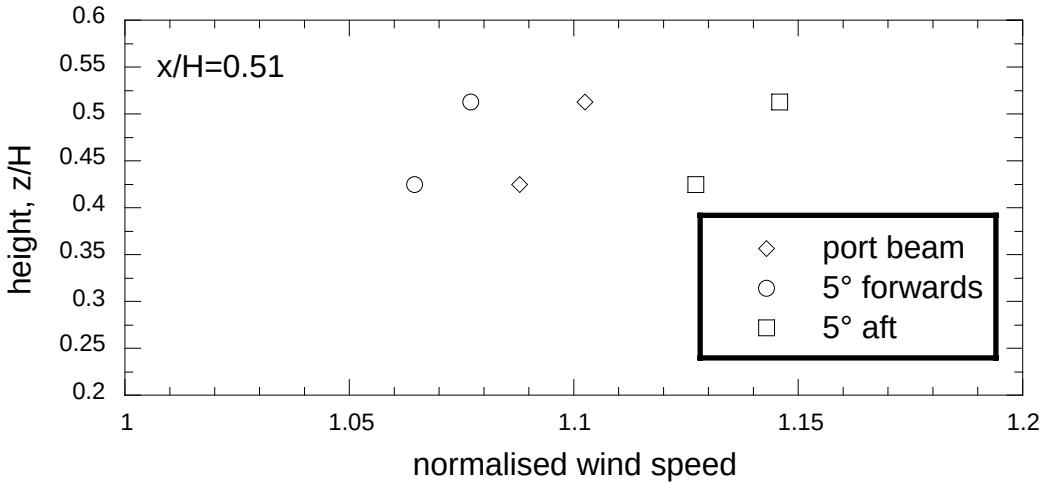

Figure 5.20 As figure 5.19, but for the flow over the port beam.

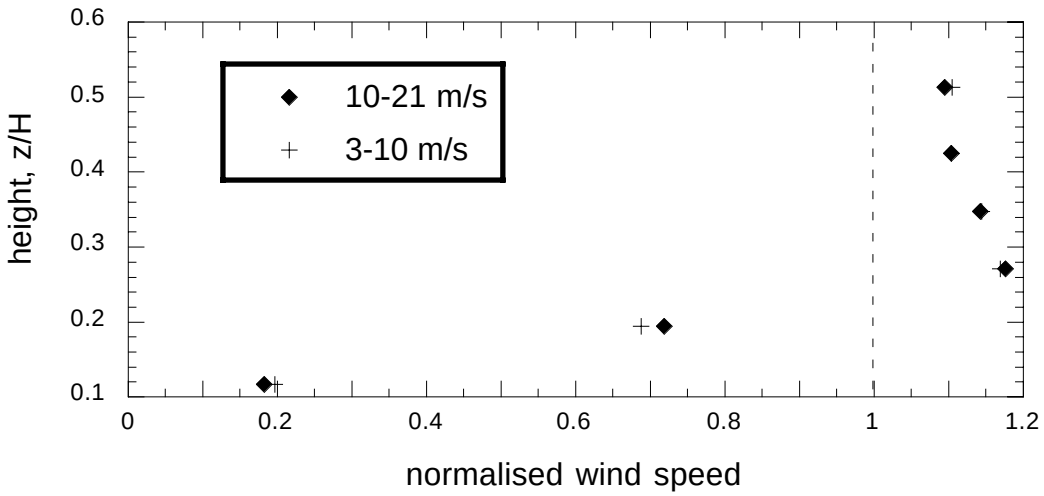

Figure 5.21 The normalised wind speed profiles at two different wind speeds for flows over the starboard beam. The vertical dashed line indicates no change in the normalised wind speed.

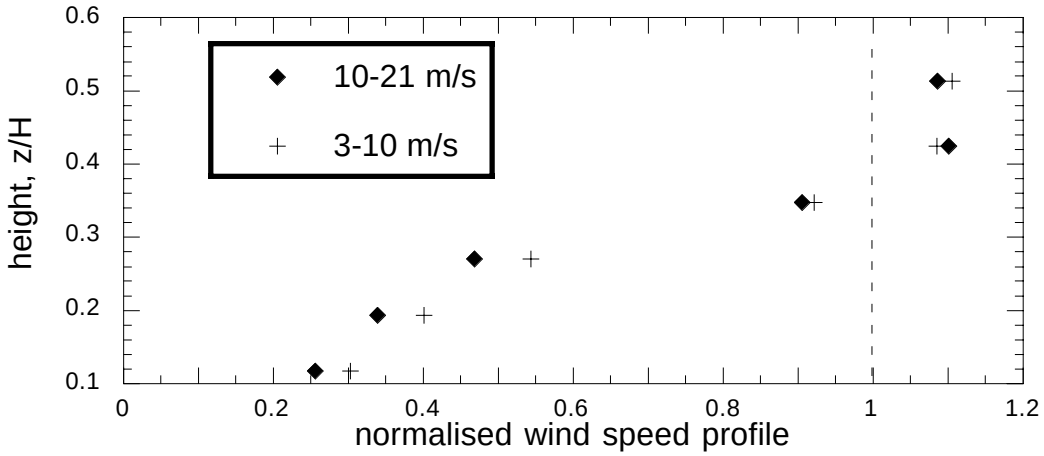

Figure 5.22 As Figure 5.21, but for the flow over the port beam.

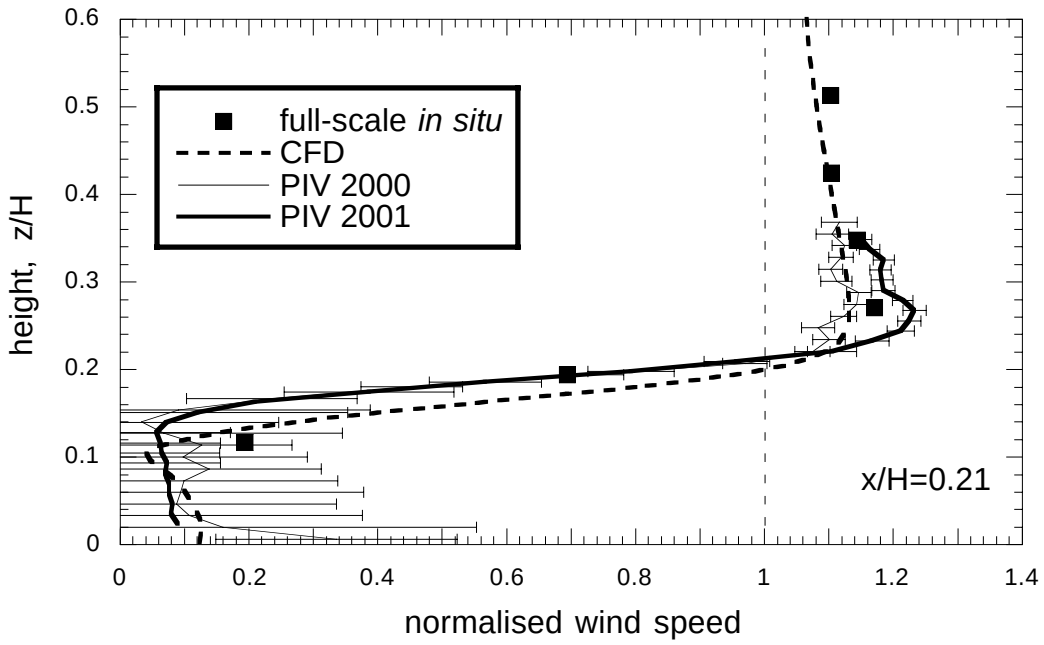

Figure 6.1 Normalised wind speed profiles over the deck house block for various methods.

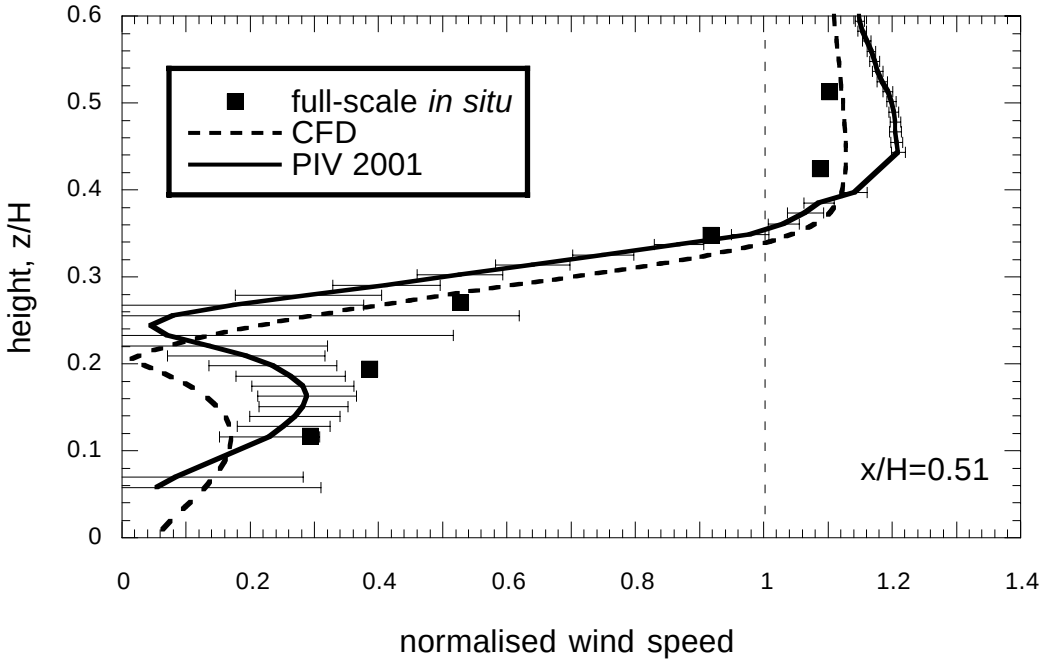

Figure 6.2 Normalised wind speed profiles over the deck house block for various methods.

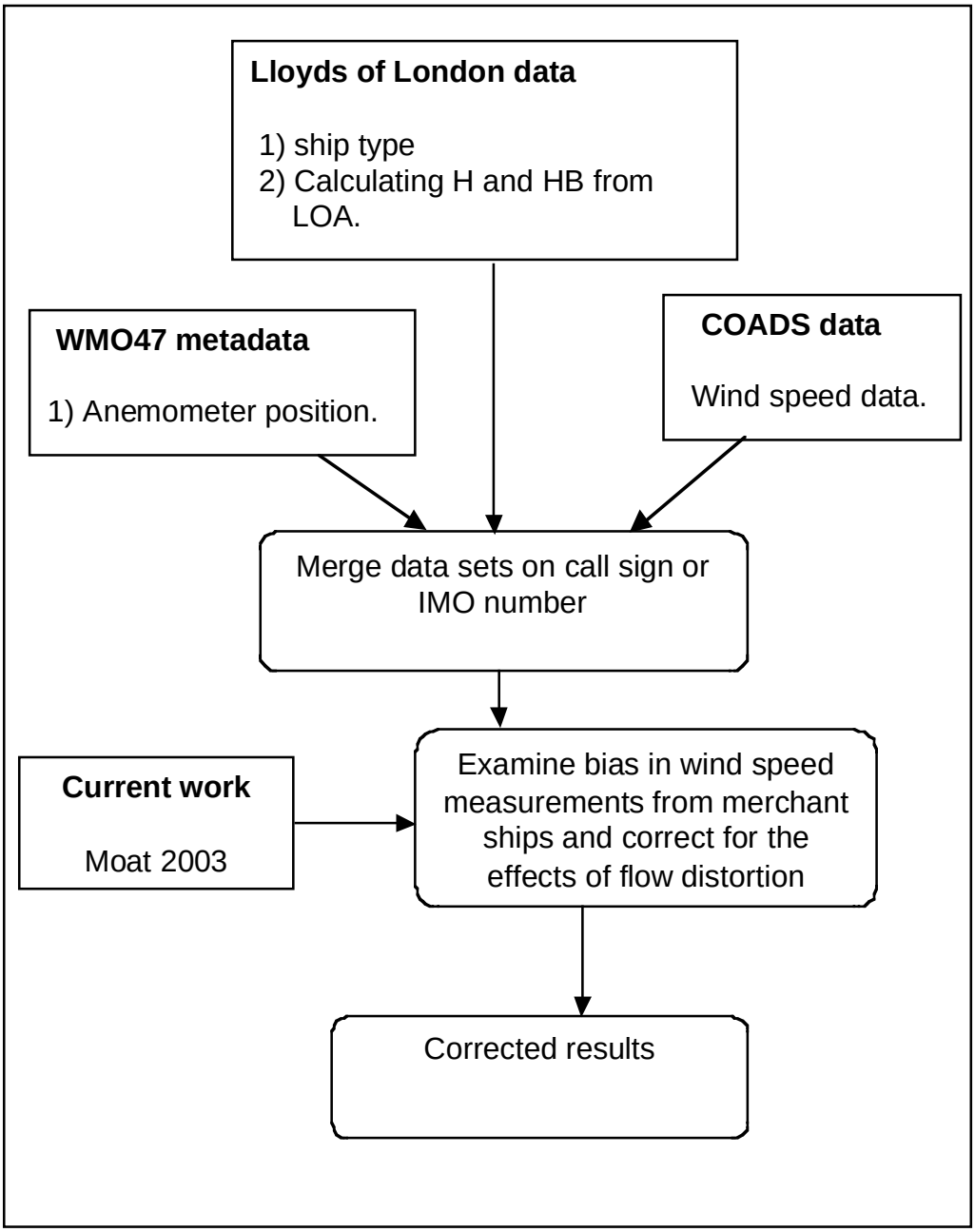

Figure 6.3 Flow chart showing the application of the results.